DETERMINATION OF OPTIMAL PROCESS FLOWRATES AND REACTOR DESIGN FOR AUTOTHERMAL HYDROGEN PRODUCTION IN A HEAT-INTEGRATED CERAMIC MICROCHANNEL NETWORK

A Thesis

by

SHALINI DAMODHARAN

Submitted to the Office of Graduate Studies of
Texas A&M University
in partial fulfillment of the requirements for the degree of

MASTER OF SCIENCE

May 2012

Major Subject: Chemical Engineering

Determination of Optimal Process Flowrates and Reactor Design for Autothermal Hydrogen Production in a Heat-Integrated Ceramic Microchannel Network

DETERMINATION OF OPTIMAL PROCESS FLOWRATES AND REACTOR DESIGN FOR AUTOTHERMAL HYDROGEN PRODUCTION IN A HEAT-INTEGRATED CERAMIC MICROCHANNEL NETWORK

A Thesis

by

SHALINI DAMODHARAN

Submitted to the Office of Graduate Studies of
Texas A&M University
in partial fulfillment of the requirements for the degree of

MASTER OF SCIENCE

Approved by:

Chair of Committee,	Benjamin Wilhite
Committee Members,	Dan Shantz
	Molly Gentleman
Head of Department,	Charles Glover

May 2012

Major Subject: Chemical Engineering

ABSTRACT

Determination of Optimal Process Flowrates and Reactor Design for Autothermal Hydrogen Production in a Heat-Integrated Ceramic Microchannel Network. (May 2012)

Shalini Damodharan, B.Tech., Anna University

Chair of Advisory Committee: Dr. Benjamin Wilhite

The present work aimed at designing a thermally efficient microreactor system coupling methanol steam reforming with methanol combustion for autothermal hydrogen production. A preliminary study was performed by analyzing three prototype reactor configurations to identify the optimal radial distribution pattern upon enhancing the reactor self-insulation.

The annular heat integration pattern of Architecture C showed superior performance in providing efficient heat retention to the system with a 50 – 150^{o}C decrease in maximum external-surface temperature. Detailed work was performed using Architecture C configuration to optimize the catalyst placement in the microreactor network, and optimize reforming and combustion flows, using no third coolant line. The optimized combustion and reforming catalyst configuration prevented the hot-spot migration from the reactor midpoint and enabled stable reactor operation at all process flowrates studied. Best results were obtained at high reforming flowrates (1800 sccm) with an increase in combustion flowrate (300 sccm) with the net H_2 yield of 53% and

thermal efficiency of >80% from methanol with minimal insulation to the heat-integrated microchannel network.

The use of the third bank of channels for recuperative heat exchange by four different reactor configurations was explored to further enhance the reactor performance; the maximum overall hydrogen yield was increased to 58% by preheating the reforming stream in the outer 16 heat retention channels.

An initial 3-D COMSOL model of the 25-channeled heat-exchanger microreactor was developed to predict the reactor hotspot shape, location, optimum process flowrates and substrate thermal conductivity. This study indicated that low thermal conductivity materials (e.g. ceramics, glass) provides enhanced efficiencies than high conductivity materials (e.g. silicon, stainless steel), by maintaining substantial thermal gradients in the system through minimization of axial heat conduction.

Final summary of the study included the determination of system energy density; a gravimetric energy density of 169.34 Wh/kg and a volumetric energy density of 506.02 Wh/l were achieved from brass architectures for 10 hrs operation, which is higher than the energy density of Li-Ion batteries (120 Wh/kg and 350 Wh/l). Overall, this research successfully established the optimal process flowrates and reactor design to enhance the potential of a thermally-efficient heat-exchanger microchannel network for autothermal hydrogen production in portable applications.

DEDICATION

To my family & friends

ACKNOWLEDGEMENTS

I would like to take this opportunity to express my sincere gratitude to my advisor, Professor Benjamin Wilhite, for his invaluable motivation, guidance and for being extremely patient throughout the course of my research. I would also like to thank Dr. Dan Shantz and Dr. Molly Gentleman for acting as members of my thesis committee and their valuable time spent reviewing my thesis.

I deeply appreciate to express my gratitude to Dr. Angela Moreno for her valuable support and guidance during the initial stage of this project and assistance throughout my research. I would like to thank Randy Marek of Technical services, William Merka of glass shop and Chemical engineering staff at Texas A&M University for their extraordinary assistance.

It's a great pleasure to thank members of Dr. Wilhite's research group – Dr. Daejin Kim, Dr. Aravind Suresh, Bhanu Kuncharam, Haomioa Zhang and Elva Moreno for providing a great work environment, and for their stimulating advice, help and suggestions. In particular, my special thanks go to Dr. Aravind Suresh for helping me to learn and understand laboratory work and for all his mind-blowing jokes and ideas. I am extremely grateful to my friends for their love and encouragement to overcome the difficult times and stay focused on my graduate study.

Most importantly, my family - Suguna Damodharan, Saranya, Praburam and Akshath, have been a constant source of love, concern, support and strength all these

years, and this thesis would certainly not have existed without them. Thanks for everything and I would like to dedicate my thesis to you guys.

NOMENCLATURE

A_i	Pre-exponential factor
E_i	Activation energy (J/mol)
C_i	Concentration of species (mol/m^3)
ρ_s	Density of solid catalyst (kg/m^3)
ρ_g	Gas density (kg/m^3)
R_D	Rate of decomposition
R_R	Rate of reforming
R_C	Rate of methanol combustion
A_R, B_R, A_D	Frequency factors of reforming and decomposition reaction
E_R, E_D	Activation energy of reforming and decomposition reaction (J/mol)
SMR	Steam to methanol molar ratio
C_R and C_D	Correction factors for BASF R3-15 catalyst ($CuO/ZnO/Al_2O_3$)
ω_i	Mass fraction
x_j	Mole fraction
D_{ij}	Multicomponent fick's diffusivity (m^2/s)
D_i^T	Thermal diffusion coefficient (kg/ms)
T_f	Subdomain temperature (K)

T_s	Surface(wall) temperature (K)
T_a	Ambient temperature (K)
R_i	Rate of appearance, species i (kg/m^3s)
r_p	Pore radius (m)
M_i	Molecular weight of the component
ε	Porosity, assumed to be 0.5
τ	Tortuosity, assumed to be 2
υ	Atomic diffusion volume
k	Permeability of the porous medium and is taken as 1e-9 m^2
P	Pressure in the subdomain (Pa)
η	Viscosity of the porous medium (Pa.s)
K	Thermal conductivity of the fluid/solid (W/mK)
Q	Heat source (W/m^3)
C_p	Heat capacity at constant pressure (J/kg/K)
h_{fs}	Fluid-solid heat transfer coefficient ($W/m^2/K$)
h_s	Heat transfer coefficient of solid to ambient ($W/m^2/K$)
ΔH	Heat of reaction (J/mol)

TABLE OF CONTENTS

Page

LIST OF FIGURES

Page

LIST OF TABLES

Page

1. INTRODUCTION

One of the major challenges in emerging portable power sources is the development of efficient, compact yet scalable microreactor systems capable of converting biomass - derived alcohols to hydrogen at high thermal and fuel efficiencies. Such systems still require breakthroughs in process intensification for hydrogen production at (i) the portable scale for standalone power production from high energy density liquid fuels and (ii) industrial scale for efficient resource conversion to clean hydrogen commercial fuel [1]. The goal of this thesis work is to address both of these challenges.

1.1 Hydrogen fuel cells

Recent technological advances demand higher energy density and longer operational time from portable power sources. The lithium- and nickel- based battery technologies (Ni-MH, NiCad and Li-Ion) have served as a significant energy supply for portable devices, but these systems are limited by energy densities and environmental concern. Hydrogen-driven fuel cells offer high energy densities, low cost and reduced environmental impact, offering a promising alternative to batteries for meeting portable power for consumer (e.g. laptop computers, PDAs, cellular phones) and military needs (e.g. communication devices, micro sensors and actuators) [2].

This thesis follows the style of *IEEE Journals*.

Proton exchange membrane fuel cells (PEMFCs) are attractive because of their ability to convert hydrogen fuel directly to electrical work at high thermal efficiencies (>40%). PEMFCs provides at least 25-30% more efficiency compared to Internal Combustion Engines (ICE) for converting chemical energies of gasoline or hydrogen to work, with the energy efficiency range for ICEs as 20-30% compared to 40-60% for PEMFCs [3].

PEMFCs are favorable for transportation, space, military and energy storage systems due to their passive design, high energy density and mild operating conditions. Figure 1.1 presents a schematic of the PEMFC single cell. These fuel cells employ a polymer electrolyte membrane operating generally at 85-105^{o}C. The electrolyte is an ion exchange membrane, which nominally allows only protons and water to pass through it. Nafion® membrane, a sulfonated PTFE developed by Dupont de Nemours and Company, remains one of the most frequently used electrolytes. This is provided by a poly – tetrafluoroethylene (PTFE) based structure, which combines chemical inertness with high acidity [4, 5].

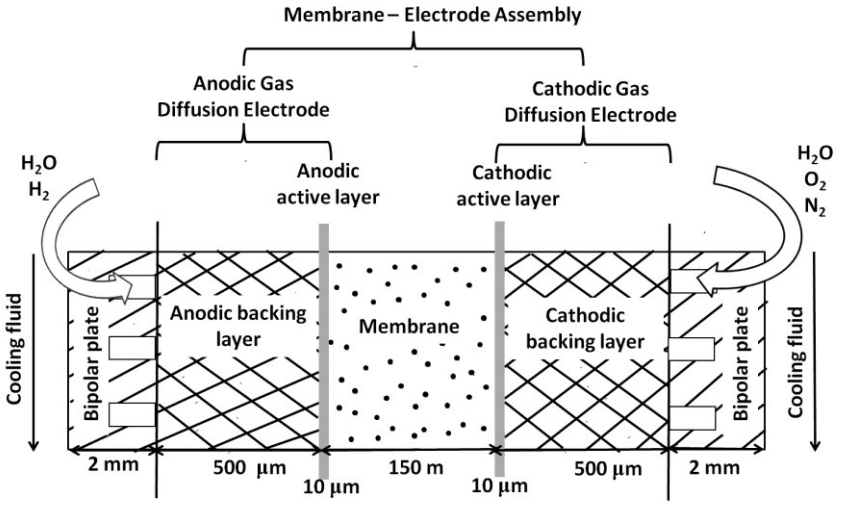

Figure 1.1. Schematic of PEMFC single cell, from Ramousse *et al*., 2005 [6]

The polymer electrolyte membrane is placed between porous anodic and cathodic backing layers to form a Membrane Electrode Assembly (MEA). The anodic and cathodic electrodes are composed of thin layers of platinum on carbon particles embedded in the polymer electrolyte membrane. The two electrodes (active layers) are located between the electrolytic membrane and the backing layers. The backing and the active layers without the membrane are together referred to as the Gas Diffusion Electrodes (GEA). The backing layers are typically made of carbon fibers coated with hydrophobic PTFE to prevent flooding and ensure uniform gas distribution to the electrode surface. Electronically conductive graphite bipolar plates are used on either face of the MEA for current collection, system cooling and gas feeding through channels [6].

At the anode, oxidation of hydrogen to protons liberates electrons. The proton migrates from anode to the cathode through the electronically insulated polymer membrane, while liberated electrons transport to the cathode via an external circuit. The cathodic reaction reduces oxygen by combining with the protons and electrons to produce water [6].

Anode: $H_2 \rightarrow 2H^+ + 2e^-$

Cathode: $\frac{1}{2}O_2 + 2H^+ + 2e^- \rightarrow H_2O$

Overall reaction: $H_2 + \frac{1}{2}O_2 \rightarrow H_2O$

Corrosion problems are minimal in PEMFCs because water is the only product formed within the cell. They offer a quick startup because of low temperature operation. Since the electrolyte is a solid membrane, it offers remarkable resistance to gas crossover and provides zero leakage of electrolyte [7].

Water and heat management are the critical factors for efficient performance of PEMFCs. The polymer membrane must remain hydrated in order to facilitate ionic conductivity, whereas excess water at the positive electrode leads to flooding which in turn prevents the oxygen access to the active layers. Operating conditions have to be chosen carefully to ensure proper water and thermal management because the water produced should neither evaporate rapidly nor support water condensation in the backing layers. Therefore, low temperature is preferred (<120^{o}C) for efficient operation of PEMFCs [7]. PEMFCs are limited by a low tolerance to CO, which manifests in the form of electrode polarization and decreases cell efficiency. The high affinity of

platinum catalyst for CO adsorption, combined with low temperatures leads to a loss in active surface area for hydrogen adsorption and decrease in electrochemical oxidation rates [8]. For example, introduction of 25 ppm of CO at a current density of 600 mA/cm^2, resulted in an increase in electrode polarization from 0.2 to 0.3 V corresponding to a 30% to 40% loss in electrical power [8].

1.2 Batteries vs hydrogen fuel cells

The performance of energy storage and delivery systems (batteries, supercapacitors and fuel cells) can be compared based upon (i) their energy content, referred as specific energy or energy density (Wh/kg or Wh/L), and (ii) their rate capability, expressed as specific power or power density (W/kg or W/L), using a Ragone plot (shown in Figure 1.2).

Batteries have intermediate energy and power densities as compared to fuel cells with higher energy densities, and supercapacitors with higher power densities [9]. Table 1.1 provides a comparison of energy densities reported for various battery systems and hydrocarbon fuels.

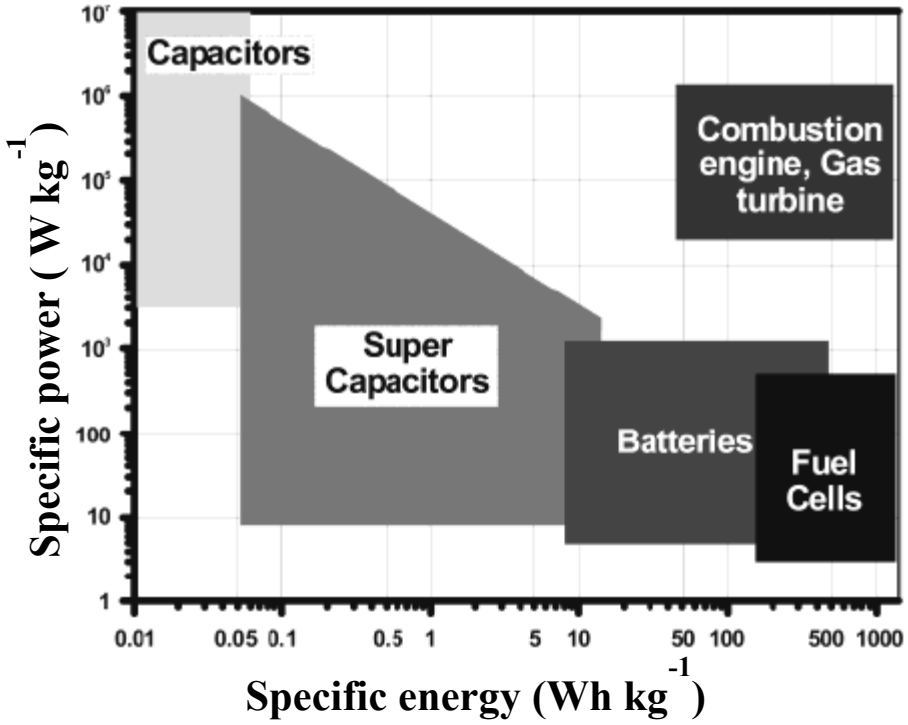

Figure 1.2. Ragone plot represents power and energy capabilities for various electrochemical energy conversion systems from Winter and Brodd, 2004 [9]

Table 1.1. Energy density of various hydrocarbon fuels and battery types [10-12]

Technology	Energy Density	
	Gravimetric[Wh/kg]	**Volumetric[Wh/l]**
Batteries		
Alkaline(primary)	35	70
Lead-Acid(rechargeable)	35	70
Ni-Cad(rechargeable)	55	170
Ni-MH(rechargeable)	70	250
Li-Ion(rechargeable)	120	350
Zn-Air(primary)	340	1050
Hydrocarbon Fuels		
Hydrogen(@ 700 bar)	39700	2100
Methanol	5600	4380
Ethanol	7500	5900
Butane	12600	7290
Iso-Octane	12340	8680
Diesel	12400	8700

Fuel cells have a significant advantage over rechargeable batteries in terms of recharging vs. refueling times, especially in portable power applications. Recharging a Li-Ion battery takes several hours (~3 hrs) and requires an external power source as well charging equipment [13], while fuel cells require minutes to refill the fuel storage system and do not require any external power other than the fuel. The refueling time of onboard hydrogen storage for hydrogen fuel cells (PEMFCs) suggested by 2009 U.S DoE targets is less than 5 mins [14]. The time span between refueling for a typical fuel cell system is also quite favorable when compared to that of batteries. For example, a cellular phone Li-battery can supply 2h of operation under continuous conversation at 0.45 A and 3.6 V, or 200h operation at 4.5 mA in stand-by mode. In the case of a direct methanol fuel cell (DMFC), 10 cells each of 5 cm^2 connected in series provides 1.6 W at 0.45 A with each cell operating at 0.355 V. The methanol consumed for each cell is 0.21 ml for every 2 h of conversation and 2.1 ml for the whole device. Therefore, 50 ml of pure methanol provides 48 h of continuous conversation or 4800 h in stand-by operation. If the recharging frequency for battery is 2 days then the refueling frequency for DMFC will be every 50 days [15]. Though the PEMFC system requires an additional fuel processor for on-board conversion of liquid hydrocarbon fuels (e.g. methanol) to hydrogen, it offers higher efficiency and power density compared to DMFCs. The critical factor which limits DMFC performance is the fuel (methanol) crossover which degrades the cathodic reduction reaction [16]. Another disadvantage with DMFCs when compared to PEMFCs is the poor electrochemical activity of anodic methanol oxidation (kinetic

losses), which requires high Pt loading (5 to 10 mg Pt/cm^2) compared to PEMFCs (0.2 to 0.5 mg Pt/cm^2) for efficient operation.

Fuel cells operating on stored hydrogen offer energy densities at 500 – 1000 Wh/kg as compared to projected energy density for batteries of 300 Wh/kg [17]. The primary challenge with hydrogen fuel cells for transportation and stationary power applications is that of onboard hydrogen storage. Gaseous hydrogen compressed at approximately 69 MPa (10,000 psi) provides sufficient volumetric energy densities, at the cost of substantial difficulties associated with storage and transportation. Additionally, though hydrogen gas has high gravimetric energy density (39700 Wh/kg), even in a compressed state it offers poor volumetric energy densities (2100 Wh/l) compared to liquid fuels (e.g. methanol). For these reasons, onboard hydrogen production via catalytic reforming of energy-dense hydrocarbon fuels remains an attractive option for portable power systems.

Several portable processing units have been investigated for this application over the past decade, with their subsequent analysis providing valuable insight into the capacities and efficiencies required to ensure a competitive portable power system. For example, Palo *et al*. presented their analysis of a fuel processor consisting of a reformer, combustor and two vaporizers integrated with a PEMFC, and compared this system to a Li-Ion battery. At fuel cell power of 13 W_e, 45% fuel processor efficiency resulted in a predicted overall system efficiency of 22% assuming fuel cell efficiency of 60% with 80% hydrogen utilization [17]. Assuming 1 kg of fuel processor/ fuel cell system, with 14 day and 3 day mission time, the system offers energy densities of 720 Wh/kg and 450

Wh/kg respectively, which is significantly higher than projected energy densities of Li-Ion batteries (300 Wh/kg). Thus, a portable power system coupling a fuel reformer with a proton-exchange membrane fuel cell can achieve higher energy densities than competing battery technology.

1.3 Centralized hydrogen production

Commercial vehicles emit significant amounts of carbon oxides, volatile organic compounds (VOC), nitrogen (NOx) and sulfur oxides (SOx) into the atmosphere which deteriorate air quality and may contribute to climate change. The largest sources of CO_2 emissions are the electric utility and transportation sectors [18]. In light of growing environmental concerns, there have been significant efforts to identify cleaner fuels for transportation, stationary and portable power applications for reduced carbon emissions. Fuel cells operating on hydrogen emit water as their sole by-product, providing clean, emission free power. While hydrogen may be produced from solar or nuclear resources using electrolysis cells, the most economical means of producing hydrogen at sufficient capacity is through catalytic steam reforming of hydrocarbon feedstocks, integrated with carbon capture and sequestration techniques to minimize emissions [19]. Hence, hydrogen can be produced on large scale from biomass feedstocks in centralized facilities and subsequently distributed at fueling stations and/or community locations as a universal clean fuel for transportation and power applications. This scenario would focus technique for controlling carbon emissions at centralized locations, where efficient reactor technologies can be implemented to minimize environmental impact of

distributed power at transportation sectors [18, 20]. Centralized large-scale hydrogen production offers low production cost, high production & energy efficiency with greater control on carbon and other emissions than localized small-scale hydrogen production [19, 21].

The major challenges to centralized hydrogen production are the need for large market demand and cost-effective infrastructure for hydrogen transmission and distribution. During the early stages of implementing a hydrogen economy, high costs and safety concerns associated with the distribution of hydrogen to refueling stations may inflate the cost of hydrogen to roughly three times the current production cost [19]. This requires breakthroughs in improving plant efficiency, reducing capital cost while enhancing the reliability and operating flexibilities. If these challenges are met, to satisfy a volatile fuels market, cost-effective hydrogen production in the long term may be achieved by centralized plants and efficient distribution pipelines [19, 21].

1.4 Process intensification

Process Intensification (PI) is the process of reducing the physical size of a chemical plant with improved chemical productivity by optimum integration of heat, mass and/or momentum transfer in a single reactor chamber. The advantages of process intensification may include reduced cost and/or size, improved safety of operation and greater operational flexibilities. PI offers higher production capacity with smaller reactors leading to reduced investment costs, higher reaction yields and/or thermal efficiencies, leading to reduced raw materials and utilities consumption for reduced

operating costs and waste minimization. Operation with smaller equipment improves safety of chemical processes and offers controlled process parameters. With decrease in size and increase in efficiency, PI offers ease of scale up by replication to increase the production volume [22].

Process intensification in reactor design is achieved using multifunctional reactors, in which two or more chemical and/or transport processes occur simultaneously in a single volume [23]. Mass integration in a multifunctional reactor coupling reactors and separators can be achieved using reactive distillation [22, 24], reactive extraction [25, 26] or membrane reactor configurations [27]. Thermal integration in multifunctional reactor via coupling exothermic and endothermic reactions can be achieved using one of the three reactor configurations [28] shown in Figure 1.3.

- Direct coupling (directly coupled adiabatic reactor) – exothermic and endothermic reactions simultaneously occur in the same catalytic bed [29-32]. This configuration offers advantages of simple design and rapid heat transfer between endothermic and exothermic reactions. Disadvantages include the need for product separation, the need for bifunctional catalysts, and lack of direct control over reactor temperature or individual reaction rates.
- Regenerative coupling (Reverse Flow reactor) – exothermic and endothermic reactions take place in the same catalytic bed at alternate time spans [33-35]. This configuration is most effective for weakly exothermic reactions where the combustion heat allows for storage with the reactor. The primary disadvantage of

this configuration is the need for complex valving, necessary for periodic flow reversal which are susceptible to damage and limit operation at microscale [36].

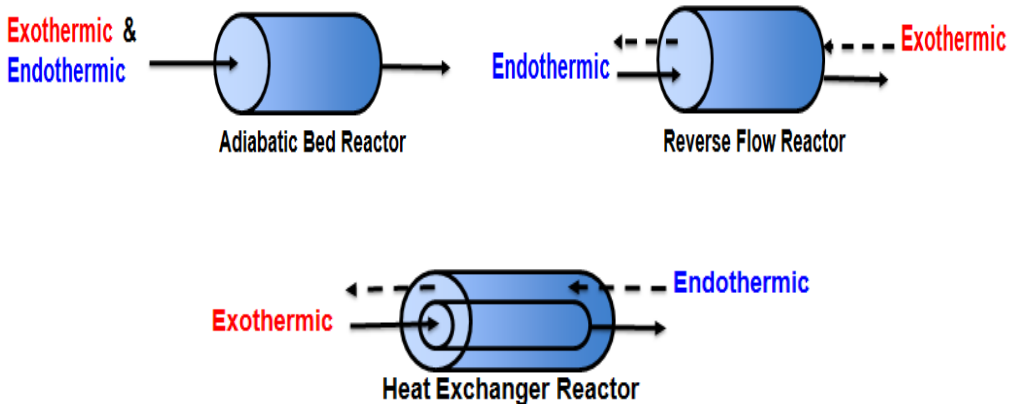

Figure 1.3. Schematic of three reactor configurations coupling exothermic and endothermic reactions

- Recuperative coupling (heat exchanger reactor) – exothermic and endothermic reactions are carried out in separate catalytic volumes either with co-current or counter-current configuration [36-40]. Advantages of heat-exchanger reactor configuration include (i) exothermic and endothermic reaction products are always separated and their process chemistries are controlled externally, (ii) enables the usage of air instead of oxygen for combustion processes by elimination of nitrogen separation from the product mixture, (iii) provides independent selection of catalyst, fuel and other operating parameters. The primary disadvantage of the heat exchanger configuration lies in the management

of axial temperature profiles to maximize heat transfer rates and minimize heat losses due to axial conduction at reactor inlet/outlet.

For portable power applications, the heat exchanger multifunctional reactor configuration is preferred over the adiabatic and reverse flow reactor configurations owing to the maintenance of separate process flows and the lack of moving parts or complex valving [28, 41]. Microchemical systems, with their micron-scale design results in order-of-magnitude increase in interphase heat-mass transport rates as compared to conventional-scale systems, offer a highly efficient platform for thermal coupling of endothermic and exothermic processes using heat exchanger reactor configurations.

1.4.1 Microreactors

Microreactors have emerged as a promising technology for multiple industrial and scientific applications. Enhanced heat transfer characteristic of microreactors enables safer operation with improved process conditions, making important intermediates and products without the danger of runaway reactions in conventional reactors [42, 43].

Advantages of using microreactors include [1, 44-46]:

1) Rapid interphase heat and mass transport resulting from a high surface-to-volume ratio, relative to conventional reactors.

2) Ability to exploit high thermal conductivity materials (e.g. steel, silicon) in tandem with rapid heat transport rates to ensure isothermality, even with highly exothermic reactions.
3) Reduction in reagent and catalyst capacity which facilitates rapid, economical and environmentally feasible screening of new reactor pathways.
4) Ability to scale up processes ("numbering up") by increasing the number of identical parallel microreactor units which eliminates costly redesign and deployment time.
5) The inherent redundancy characteristic of microreactors which provides safer operation by enabling online monitoring through integration of sensors and control components.

Challenges associated with microreactors include: high sensitivity to fouling, difficulty in sealing the system or providing suitable fluidic connections to conventional plumbing and managing heat losses to ambient due to high heat transfer rates. These issues can be minimized by proper material selection and reactor design [1, 47].

Thermal management is the crucial factor in microreactor operation for portable fuel processors. Material and packaging selection play an important role for microreactor construction in order to maximize thermal efficiency through (i) tailoring hot spot formation and (ii) minimizing conductive losses to packaging or ambient. High thermal conductivity substrates such as silicon [38, 48] and stainless steel [49] limit heat exchanger efficiencies to below 50% and result in rapid thermal equilibration of the solid phase which leads to a near-isothermal slab.

Shah and Besser [48] studied the heat loss mechanism of a silicon microchemical system for methanol fuel processor (shown in Figure 1.4) by analyzing various packaging methods to minimize heat losses. The fuel processor consisted of a steam reformer (SR), combustor and PrOx reactor, fabricated in silicon using lithography and chemical etching techniques. Each process has unique heat duty and optimal operating temperature range. The methanol steam reforming reaction should be operated at a temperature range of 220-260^{o}C for obtaining higher yields [50]. In order to maintain optimum operating temperature in each component, the thermal gradient of the silicon micro-reformer was increased by insertion of microfabrication insulators between fuel processor (FP) components. Microfabricated vacuum insulation was achieved by sealing the cavity etched in silicon to trap the required vacuum to create low thermal conductivity around the silicon microSR.

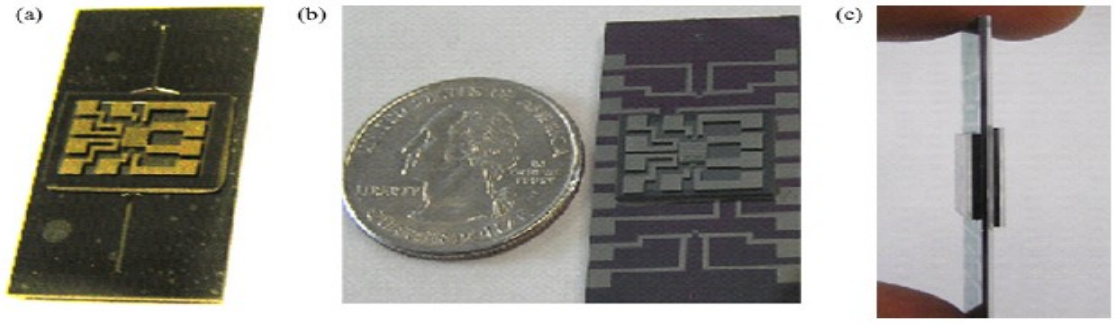

Figure 1.4. Silicon SR microreactor bonded with insulation chips on both sides (a) Front-side of microreactor (b) Backside of microreactor (c) Assembled micro-reformer, from Shah and Besser, 2007 [48]

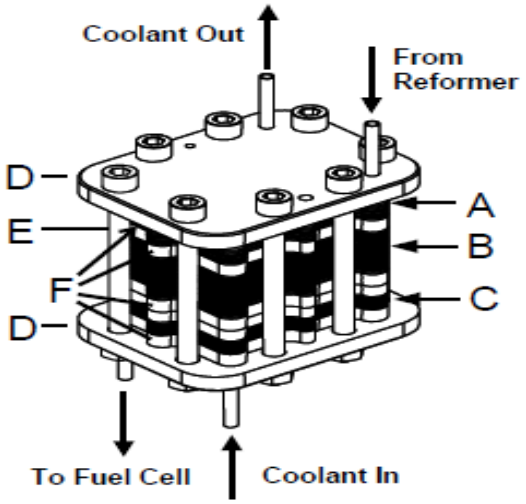

Figure 1.5. Schematic of assembled microreactor with A- high temperature heat exchanger, B-Preferential oxidation reactor, C- low temperature heat exchanger, F- four insulation plates, from Delsman *et al*., 2004[49]

Delsman [49] designed and analyzed the heat transfer efficiency of a stainless steel microdevice (shown in Figure 1.5), integrating two heat exchangers with one preferential oxidation reactor. The thermal efficiency of the system was analyzed by three different sets of insulation plates inserted between the reactor and heat exchangers to provide thermal isolation between components. The thermal resistance (layer thickness divided by thermal conductivity) was varied for each type of insulation. Heat transfer efficiency of the microdevice was observed to increase with the temperature differences (thermal resistance) created by the insulation plates between components.

Peterson [51] demonstrated that low thermal conductivity material gives the best performance for the construction of micro-scale counter flow heat exchangers because

the usage of high thermal conductivity material leads to excessive axial conduction heat losses in the device. Increase in heat conductivity of the wall offset the temperature gradient within the substrate which degrades the heat transfer efficiency, whereas reduction of heat conductivity towards zero provides negligible heat transfer efficiency. The optimal substrate heat conductivity needed to maximize thermal efficiency of counter-current micro-heat exchangers is within the range of glass and ceramics[52]. Modeling analysis performed by Frauhammer [39] reported that the internal heat exchange with the ceramic reactor seems to be efficient to maintain an ignited steady-state and provides optimized process. The major challenge associated with ceramic reactors is the thermo-mechanical stability caused due to thermal stress by local heat trapping and recirculation, which leads to cracks in the hot spot region at higher temperatures [36].

High thermal conductivity materials (silicon, stainless steel) require insulators to increase the thermal gradient in the system to enhance the thermal efficiency of the microdevice. Usage of insulators increases weight and volume of the system thereby decreasing the energy density of the fuel processor. With low thermal conductivity substrates such as ceramics [37, 39, 53], large thermal gradients are maintained in the reactor without insulators and act as a driving force for effective radial heat transfer by limiting axial conduction heat losses via packaging [54]. Therefore, ceramic substrates offer enhanced reactor performance by increasing thermal efficiency of the system.

Ceramic monolithic reactors consisting of parallel channels with small diameters, offer a higher surface to volume ratio and a lower pressure drop, are effective for

catalytic processes. A better temperature profile is achieved in the catalytic bed by coupling exothermic and endothermic reactions in these reactors, which offers good catalytic activity by reducing thermal degradation of products and feedstocks [23].

1.4.2 Honeycomb monoliths

A monolith is a large uniform block of a single building material, and its structure is referred to as "honeycomb structure". In heterogeneous catalysis, monolith is considered as a support to catalytically active component or it itself acts as a catalyst if the monolith structure contains catalytic component. Monoliths are made up of either ceramic (cordierite) or metallic (stainless steel, metal alloys, etc) materials in various shapes (rectangular, square, circular, etc) with their channel walls of different thickness. The number of channels, their diameters and wall thickness determines the cell density or cells per square inch (cpsi). This is the key component for mass transfer controlled reactions and pressure drop, which aids in calculating geometric surface area [55].

Ceramic monolith structures are prepared by extrusion in specially designed devices (extruders) and by corrugation. The most common material used for monolith extrusion is cordierite ($2MgO.2Al_2O_3.5SiO_2$) with alumina. Other materials used for monolith extrusion include SiC, TiO_2, ZrO_2, $ZrSiO_4$, Mullite ($3Al_2O_3.2\ SiO_2$), Al titanate ($Al_2O_3.TiO_2$) and Li-Al silicate ($LiO_2.\ Al_2O_3.4SiO_2$). Metallic monoliths are obtained exclusively by corrugation (flexing) of flat and corrugated metal plates and/or bends. Metallic monolith structures are most commonly made of stainless steel and Fecralloy (73% Fe, 15-20% Cr, 5% Al, rare metals in traces) [55].

A monolithic catalyst is obtained by applying the layer of catalytically active component or a suitable support material (γ-Al_2O_3, SiO_2, ZrO_2, carbon, zeolites, etc) containing one or more catalytically active components (Pt, Pd, Rh, zeolites, etc) on the inner walls of the inert monolith structure, and this process is termed as coating or washcoating. If the required support material is an integral part of the monolith structure, then the catalytically active component can be deposited directly on the monolith. Else, catalytically active component should be applied after coating the monolith with appropriate support material. Coating of support material and catalytically active component provides required porosity, good mechanical properties and improved dispersion of catalytically active phase [55].

Advantages of monolithic catalyst include: (1) high geometric surface area, (2) reduced pressure drop, (3) improved interphase mass transfer, (4) good thermal and mechanical properties, (5) simple scale up, etc., which make them superior to conventional particle catalysts [56]. Honeycomb ceramic monoliths are used widely in various hydrogen production technologies such as for autothermal reforming of diesel and jet fuel [57], autothermal reforming of methane [35], ethanol steam reforming [58], autothermal reforming of gasoline [59], partial oxidation of ethanol [60], etc.

1.5 Hydrogen production technologies

Several fuel processing technologies are available for producing hydrogen from hydrogen rich materials including hydrocarbon reforming, ammonia reforming, plasma reforming, pyrolysis and aqueous phase reforming.

Ammonia reforming offers a simple gas clean-up process and the strong odor of ammonia provides easy leak detection. Ammonia, an inexpensive and sustainable fuel for storage and transportation, is considered suitable for portable power applications with its high energy density of 8900 Wh/kg. The disadvantages that make ammonia reforming inefficient for onboard fuel processors are: (1) toxicity of ammonia which demands advanced infrastructure for processing concentrated solution and (2) ammonia poisoning causes severe and irreversible losses to PEMFC performance, unlike reversible losses from CO exposure. **Plasma reforming** overcomes certain limitations of conventional reforming such as cost, size and weight requirements, deterioration of the catalyst, and limitations on hydrogen production from heavy hydrocarbons. The overall reaction of plasma reforming was same as the conventional reforming where the energy and free radicals for the reforming reaction are provided by plasma generated with the help of electricity or heat. The disadvantages include the electrical requirement and significant electrode erosion at high pressures; the latter limits plasma reforming for fuel production, especially at a portable scale. **Pyrolysis** offers CO and CO_2 emission-free process through decomposition of hydrocarbon into hydrogen and carbon in water-free and air-free environments. The other advantages of this process include fuel flexibility, relative simplicity and compactness, a clean carbon by-product and reduction in CO and CO_2 emissions. The most significant challenge with this process arises with carbon fouling which affects the system performance. **Aqueous phase reforming** (APR) reactions are quite complex which produce hydrogen from oxygenated hydrocarbons or carbohydrates. The advantages of APR include elimination of vaporization of water and

feedstock, which eliminates a system component so that fuels like glucose can also be processed. Therefore, this technology is efficient for converting biomass feedstocks to hydrogen. The main disadvantage lies with catalyst instability during long reaction runs. Comparing other techniques, the most advantageous and widely used method of hydrogen production is the reformation of energy-dense hydrocarbon fuels.

1.5.1 Hydrocarbon reforming

Hydrogen can be produced from liquid hydrocarbon fuels by three primary techniques: Steam Reforming (SR), Partial Oxidation (POX) or Autothermal Reforming (ATR).

1.5.1.1 Steam reforming

Steam reforming process (Eqn 1.1) is a combination of hydrocarbon fuel decomposition and subsequent reactions of methane and CO with steam, and Boudouard reactions. The resulting product mixture is comprised primarily of hydrogen, carbon monoxide and carbon dioxide. The overall steam reforming reaction is strongly endothermic, requiring efficient external heat addition to drive the reaction. To avoid carbon deposition, the H_2O/HC molar ratio should be slightly higher than the stoichiometric value [20, 61].

$$C_nH_m + (n+2p)H_2O \Rightarrow (n-p)CO + pCO_2 + (n+2p+m/2)H_2 \quad \Delta H_{rxn} > 0\,(\text{endothermic}) \qquad (1.1)$$

The presence of steam and carbon monoxide provides for further reaction leading to water gas shift reaction (Eqn 1.2) producing carbon-dioxide and hydrogen. High and

low temperature WGS reactors are used to convert carbon monoxide to carbon dioxide. In high temperature WGS reactors (>350^{o}C), the reaction is limited by thermodynamics because of fast kinetics at higher temperatures. So, low temperature reactors (210-330^{o}C) that use copper catalysts are preferred to produce high purity hydrogen for on-board power generation [20, 61].

$$CO + H_2O \Leftrightarrow CO_2 + H_2 \qquad \Delta H_{rxn} = -41.1 \text{ kJ/mol} \qquad (1.2)$$

1.5.1.2 Partial oxidation

In partial oxidation, the hydrocarbon fuel is partially oxidized with oxygen to give hydrogen and carbon monoxide (Eqn 1.3). This is an exothermic reaction, which may be carried out with or without a catalyst [20, 62]. The oxygen -to-fuel ratio (n) controls the overall heat of reaction and hydrogen yield [61]. Table 1.2 shows the enthalpies of steam reforming and partial oxidation reaction for various hydrocarbon fuels.

$$C_nH_m + \frac{n}{2}O_2 \Rightarrow nCO + \frac{m}{2}H_2 \qquad \Delta H_{rxn} < 0 \text{ (exothermic)} \qquad (1.3)$$

Table 1.2. Enthalpies of steam reforming and POX for various hydrocarbon fuels

Hydrocarbon fuel	Enthalpy of Steam reforming (ΔH_{rxn})[kJ/mol]	Enthalpy of POX (ΔH_{rxn})[kJ/mol]
Methanol	49.5	-193.2
Methane	164.646	-36
Ethanol	173.534	-14
Propane	375.058	-227
n-Octane	929.758	-660

1.5.1.3 Autothermal reforming

Combining the heat effects of partial oxidation and steam reforming, the autothermal reforming reaction (Eqn 1.4) occurs by reacting hydrocarbon fuel with steam and oxygen together in the same reactor without any external heat supply. The steam reforming reaction occurs by absorbing some of the heat generated by partial oxidation, limiting the maximum temperature in the reactor. Choosing an appropriate catalyst helps to achieve desired conversion and product selectivity [63]. The oxygen to fuel (O/C) ratio and steam to carbon (S/C) ratio are selected in order to control the reaction temperature and product gas composition for preventing coke formation [20].

$$C_nH_m + \frac{n}{2}H_2O + \frac{n}{4}O_2 \Rightarrow nCO + (\frac{n}{2} + \frac{m}{2})H_2 \quad \Delta H_{rxn} < 0 \text{ (slightly exothermic)} \qquad (1.4)$$

By using appropriate operating conditions and catalyst, fuel processing reactors are designed to maximize hydrogen production and minimize carbon formation.

1.6 Methanol as a fuel for hydrogen production

Methanol, being a liquid fuel, is an efficient hydrogen carrier for fuel cell applications because of its unique advantages specifically:

1) High H/C ratio (4:1), equal to that of methane.
2) Being a liquid, it is stable at all environmental conditions.
3) Ease of storage and transportation.
4) Cheap and readily available.
5) Hydrogen can be produced from methanol via catalytic reactions at lower temperatures (150-300^{o}C) compared with other fuels (>500^{o}C), owing to the absence of carbon-carbon bonds, which require significant energy to cleave.
6) Low temperature conversion of methanol leads to minimal CO formation, even with no special mechanism provided by the catalyst for high CO_2 selectivity over CO.
7) High boiling point (65^{o}C), which allows for easy vaporization in approximately the same as water temperature range.
8) It is miscible with water and easily metabolized by organisms in the environment. Hence, methanol spills have minimal environmental damage.
9) Depressed freezing point from -44^{o}C to -74^{o}C of methanol/water mixtures in their normal operating range (45-60 wt% methanol), facilitates use of methanol-fueled systems in cold environments.

10) Being a synthetic fuel, sulfur contamination is minimal as compared to petroleum distillate fuels.

The U.S military recognized methanol as a promising fuel for portable power applications because of its higher energy density compared with primary batteries [62]. Unlike methanol, other hydrocarbon fuels such as gasoline, propane, natural gas, diesel, JP-8 etc. contain certain levels of sulfur that must be removed by advanced desulfurization techniques; and reformation of these hydrocarbon fuels requires high temperature operation (>500^{o}C). Moreover, methanol processing is less complex compared to other fuels like diesel, gasoline etc, providing an excellent test chemistry for developing new reactor or system design [62].

1.6.1 Methanol steam reforming (MSR)

Methanol Steam reforming (Eqn 1.7) involves endothermic methanol decomposition (Eqn 1.5) followed by exothermic water gas shift reaction (Eqn 1.6). The overall methanol steam reforming reaction is endothermic and it requires an external heat source to proceed with the reaction. Methanol steam reforming reaction produces carbon dioxide and hydrogen by reacting methanol with water vapor. The water gas shift reaction does CO clean-up by converting CO to CO_2 by increasing hydrogen productivity.

$$CH_3OH \Rightarrow CO + 2H_{2,} \qquad \Delta H_{rxn} = 90.54 \text{ kJ/mol} \qquad (1.5)$$

$$CO + H_2O \Leftrightarrow CO_2 + H_{2,} \qquad \Delta H_{rxn} = -41.09 \text{ kJ/mol} \qquad (1.6)$$

$$CH_3OH + H_2O \Rightarrow CO_2 + 3H_2, \qquad \Delta H_{rxn} = 49.45 \text{ kJ/mol} \qquad (1.7)$$

Cu- or Pd-based catalysts can be used for methanol steam reforming process operating at relatively low temperatures. Copper based catalysts such as $CuO/ZnO/Al_2O_3$ are considered as the highly preferred low temperature shift catalyst for traditionally performed methanol-steam reforming reaction [64]. Disadvantages with a copper catalyst include deactivation, pyrophoricity and thermal sintering at higher temperatures (>300^oC). Therefore, control of maximum operating temperature is important to prevent loss of catalyst activity due to thermal sintering of copper crystallites [50]. During methanol steam reforming reaction, the oxidation state of Cu in oxidized copper based catalyst decreases gradually with time. The oxidation state of copper (Cu^+) which is more active for MSR than metallic copper (Cu^0), has to be stabilized or dispersion of copper species has to be increased in Cu-based catalysts to increase the activity of MSR reaction [64]. Addition of additives such as Cr_2O_3, ZnO, ZrO_2 etc. to copper based catalyst minimizes thermal sintering and increases the activity and selectivity of MSR and WGS reactions by promoting the structure of skeletal copper [65, 66].

Addition of the required amount of Pt and Rh to $CuO/ZnO/Al_2O_3$ catalyst enhances reaction performance at temperatures above 320^oC [66]. The $Pd\text{-}ZnO/Al_2O_3$ catalyst exhibited greater catalyst activity and low CO selectivity at a wider temperature range, which gives similar performance as Cu based catalyst [67-69]. However, copper based catalysts are highly active than precious metal based catalysts for methanol steam reforming and oxidative steam reforming reactions [70]. Proper selection of appropriate catalyst, promoter, support type, loading, and reaction temperature has significant effects on methanol steam reforming rates and selectivities.

1.6.2 Methanol combustion/Partial oxidation

Methanol steam reforming is an endothermic reaction; therefore it requires continuous energy supply to drive the reaction. Electrical heating methods do not serve as an economical way to produce hydrogen, and imparts a dependence of the reforming system upon pre-existing infrastructure. Alternately, thermal energy for the endothermic reaction may be provided by simultaneous partial (Eqn 1.8) or complete (Eqn 1.9) oxidation of methanol, via process intensification to achieve autothermal operation. For the envisioned counter-current heat exchanger system, heat generated from combustion/partial oxidation is used to preheat the reforming CH_3OH/H_2O mixture and drive the endothermic reaction. Commercial platinum catalyst (Pt/Al_2O_3) is highly preferred for methanol combustion reaction, owing to its high stability and activity for combustion.

$$CH_3OH + \frac{1}{2}O_2 \Rightarrow CO_2 + 2H_2 \qquad \Delta H_{rxn} = -193.2 \text{ kJ/mol} \qquad (1.8)$$

$$CH_3OH + \frac{3}{2}O_2 \Rightarrow CO_2 + 2H_2O \qquad \Delta H_{rxn} = -673.2 \text{ kJ/mol} \qquad (1.9)$$

1.7 Ceramic microchannel network developed by wilhite research group

A new class of cartridge-based microchannel network was constructed by fusion of two unique approaches to material processing: (1) precision machining of metals and (2) ceramic extrusion, to achieve 2-D complex radial distribution pattern to couple two or more heat duties in one compact system. Brass distributor assembly employed in this network provides two-dimensional flow patterns, in order to distribute reactant streams

to their respective channels. Material selection for microreactor construction plays a vital role in enhancing the thermal efficiency of the system. High thermal conductivity materials such as silicon and stainless steel lead to rapid thermal equilibration of solid phase which limits thermal efficiencies by increasing axial heat losses. In contrast, ceramic substrates, with its low thermal conductivity, enables efficient heat transfer by maintaining required thermal gradient for stabilizing hot-spot and minimizes axial heat conduction losses. Therefore, this novel design of ceramic heat-exchanger microchannel network provides a cost-effective, scalable and energy-efficient process of hydrogen production for portable power.

An initial study performed by Dr.Angela Moreno [71] with a 3x3 checkerboard patterned microreactor of five methanol steam reforming channels and four methanol combustion/partial oxidation channels (shown in Figure 1.6), demonstrated that this novel design is capable of providing axially self-insulating pattern to integrate combustion/partial oxidation and steam reforming of methanol for portable hydrogen production. The system performance was evaluated at 900 sccm of combustion and 300 sccm of reforming by varying ER from 1 to 0.6.

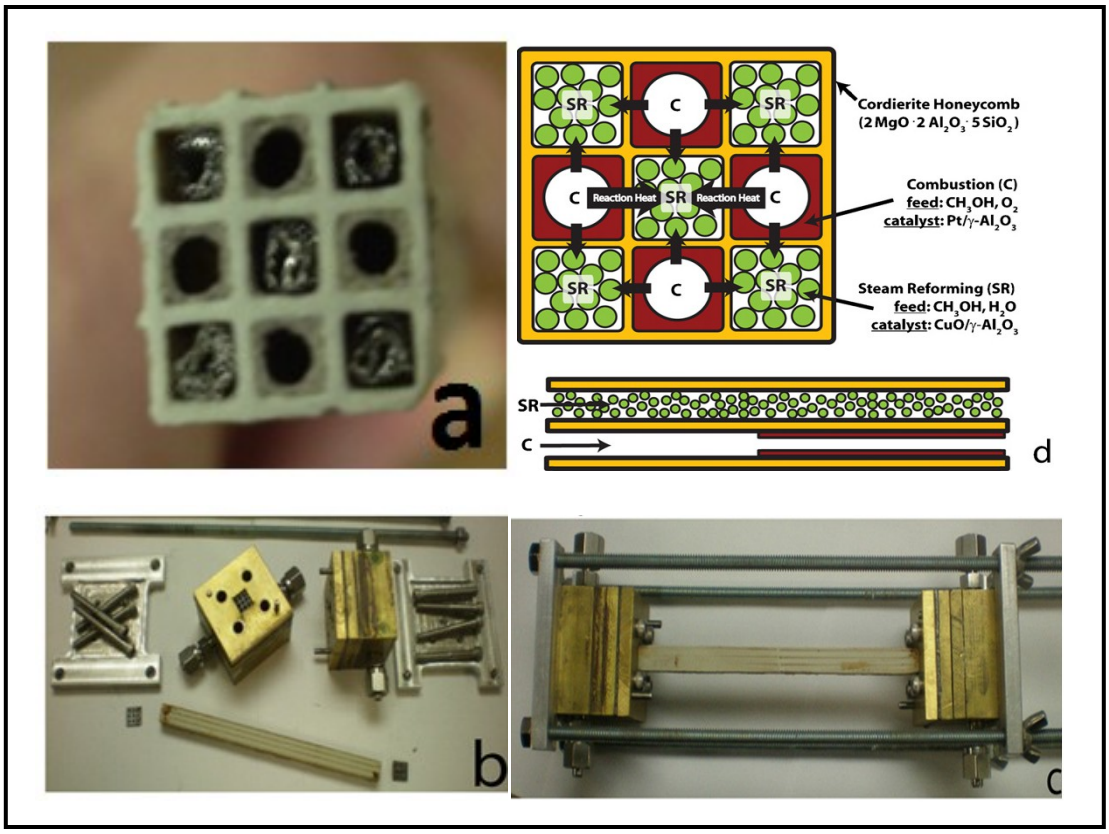

Figure 1.6. Schematic of (a) 3x3 microreactor packed with combustion and reforming catalyst (b) unassembled microchannel network (c) assembled view (d) cross-sectional schematic of checkerboard configuration with 3x3 reactor, from Moreno *et al*., 2010 [71]

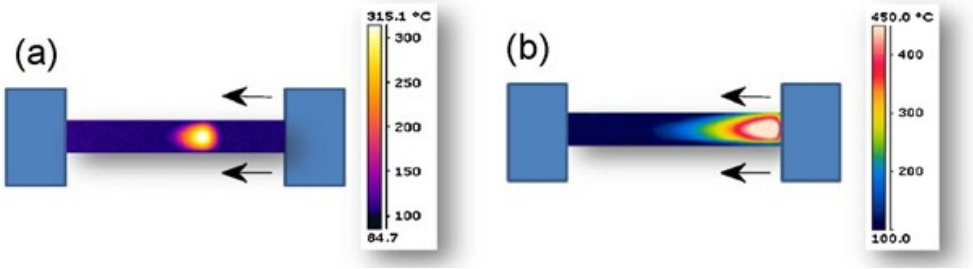

Figure 1.7. Thermal images of a 3x3 microchannel network with (a) the hotspot located at the midpoint and (b) hotspot located at the reactor inlet, from Moreno *et al*., 2010 [71]

A stable, symmetrical hot-spot of 350 – 500^{o}C was maintained at the axial mid-point of the reactor (shown in Figure 1.7) with a packaging temperature of <50^{o}C in the absence of any external insulation. The hot-spot temperature decreased from 450^{o}C to 300^{o}C with a decrease in ER from 1 to 0.6, due to the reduction of methanol conversion in the combustion volume from 84% to 55%. Further reduction in ER led to flame extinction because of insufficient oxidant supply. The best performance was obtained at ER = 0.6 with 90% methanol conversion and 70% hydrogen yield in the steam reforming channels, corresponding to an overall hydrogen yield of ~11%.

1.8 Thesis objective

The goal of this research is to extend the above design to a 5x5 heat integrated ceramic microchannel network, such that thermal efficiencies and hydrogen yields in excess of 50% are achieved by minimizing fuel consumption for combustion reaction. This is accomplished through a series of experimental and modeling studies to identify configuration, and minimize heat-loss pathways. Introducing an additional outer ring of 16 channels along with 3x3 core reforming/combustion volume is expected to further enhance the self-insulating nature of the microchannel network and provides opportunity for further impact in thermal efficiency (>50%) by flow-folding strategies. Optimizing process flowrates and equivalence ratio by analyzing various reforming and combustion flowrates is expected to enhance overall hydrogen yield and thermal efficiency through perfecting the balance between endothermic and exothermic rates. Finally, 3-D

simulations of the experimental systems are used to confirm the hypotheses and provide additional insight into the internal behavior of the microreactor assembly.

2. PRELIMINARY STUDY: MICROREACTOR ARCHITECTURE SELECTION

This chapter describes a preliminary study performed with Dr.Angela Moreno (PhD, UCONN 2010) to select appropriate microreactor architecture for subsequent optimization of hydrogen yield and thermal efficiency. As described in Chapter 1, Moreno demonstrated an initial 3x3 prototype with five steam reforming and four partial oxidation channels distributed such that axial temperature variations were minimal; overall hydrogen yields of 10-15% were reported, with stable hot-spots of >300^{o}C observed at the mid-point of the reactor axial length while either distributor remained <50^{o}C, demonstrating the ability to achieve axially self-insulating designs [71]. Based upon these results, three separate radial distribution patterns (shown in Figure 2.1) were studied to ascertain the ability to incorporate additional radial self-insulation for enhanced efficiencies using a larger 5x5 system. Figure 2.1 shows the cross-sectional configuration for each reactor design, as before all three couple the same two reactions (methanol combustion/partial oxidation and methanol steam reforming) to investigate radial distribution patterns for enhancing overall hydrogen yield. The three reactor configurations are:

- **Architecture A**: checkerboard pattern coupling methanol steam reforming and methanol combustion/partial oxidation in alternating channels to achieve maximum radial temperature uniformity; volume ratio of partial

oxidation/combustion (ΔH = -193.2 kJ/mol/ ΔH = -673.2 kJ/mol) to reforming (ΔH = 49.5 kJ/mol) is 12/13.

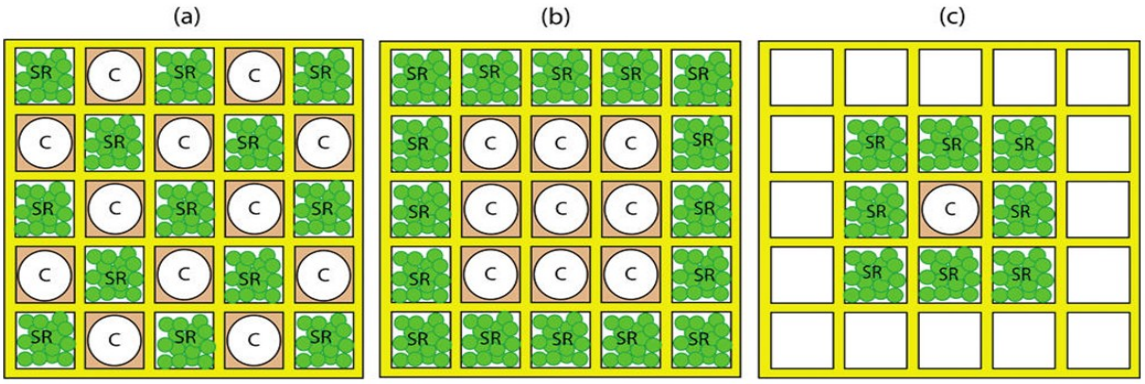

Figure 2.1. Cross-sectional schematic of (a) Architecture A: checkerboard pattern coupling two separate volumes (b) Architecture B: annular pattern coupling two separate volumes (c) Architecture C: annular pattern coupling three separate volumes, from Moreno *et al*., 2010 [72]

- **Architecture B**: annular pattern coupling methanol steam reforming and methanol combustion/partial oxidation such that reforming volume acts as a self-insulation layer; partial oxidation/combustion (ΔH = -193.2 kJ/mol/ ΔH = -673.2 kJ/mol) to reforming (ΔH = 49.5 kJ/mol) volume ratio of 9/16.
- **Architecture C**: annular/core distribution pattern coupling methanol steam reforming (ΔH = 49.5 kJ/mol) with methanol partial oxidation/combustion (ΔH = -193.2 kJ/mol/ ΔH = -673.2 kJ/mol) with an outer shell of insulating channels; combustion /partial oxidation to reforming volume ratio of 1/8.

2.1 Experimental work

2.1.1 Distributor construction

Brass plates were used for the distributor construction because of their flexibility of machining using in-house facilities. Four 1/8" x 2" x 2" brass plates were machined with two-dimensional patterns (shown in Figure 2.2) of size 1/16" in. on either side of the plate with an intermediate pattern to achieve fluidic connections across each plate. Among the four brass plates used for distributor construction, the three topmost plates were of 1/8 in. thickness to reduce the weight and size of the microchannel network; whereas the bottommost plate was of 1 in. thickness to accommodate standard 1/8" nominal pipe thread (NPT) fittings to provide fluidic connections to the ceramic microreactor. The top-most plate was fabricated with a 1/16" deep recess to accommodate a silicon or graphite gasket for reversible compression-sealing of the distributor to the ceramic microchannel network. Final assembly of the distributor was achieved by laminating the four plate stack using compression sealing with 0.065 in. thick silicon gaskets (McMaster-Carr) between each plate. Fluidic connections in the distributors were designed to compartmentalize reaction streams to their respective channels according to the intended architecture (shown in Figure 2.1).

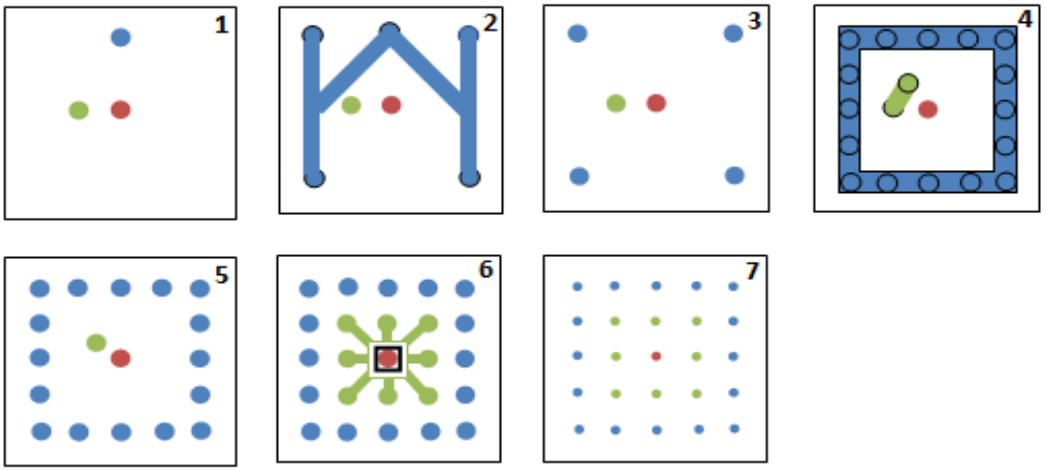

Figure 2.2. Schematic of four brass plates used for distributor C construction to attain process intensification by coupling three reaction volumes in an annular pattern. External plumbing connection made to Plate 1; Plate 7 addresses the microreactor network.

2.1.2 Ceramic microchannel network construction

Ceramic microchannels network were constructed in accordance with the three reactor architectures shown in Figure 2.1. Dense, fired non-porous cordierite honeycomb monoliths from Rauschert Technical Ceramics with a cell density of 72 cells per square inch (CPSI) were used for the construction of all 5x5 microchannel networks. Ceramic substrates were initially dip-coated with nano-alumina solution to obtain smooth uniform surface for subsequent catalyst introduction and to minimize crossover between channels due to pinholes present in the untreated substrates.

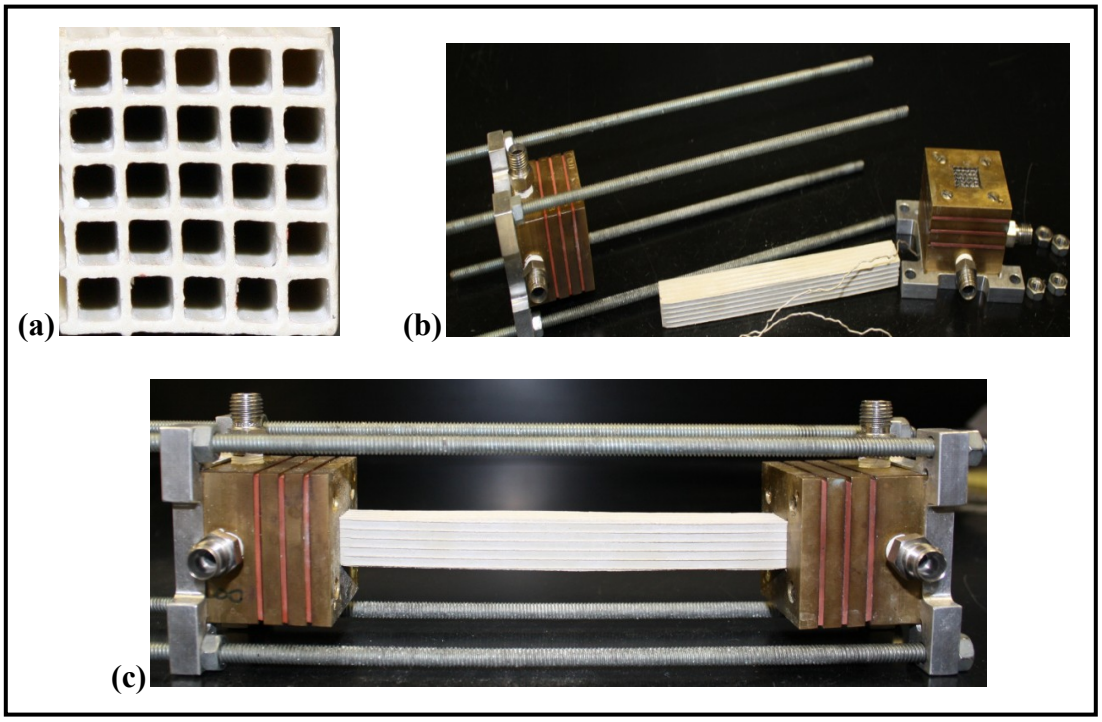

Figure 2.3. Schematic of (a) 5x5 ceramic microreactor (b) unassembled microchannel network and (c) assembled microchannel network

Combustion channels were dip-coated with Pt/Al_2O_3 solution prepared from 1wt% Pt/Al_2O_3 powder (from Sigma-Aldrich), colloidal alumina dispersion (20 wt%, Sigma Aldrich) and methanol at a ratio of 11:23:66 by mass. 20-30 drops of concentrated nitric acid were added to the Pt/Al_2O_3 solution to initiate gel formation immediately prior to dip-coating. Blocking gaskets ensured that only combustion channels were coated with the catalyst slurry, in accordance to the desired reactor configuration. The microchannel network with blocking gaskets was immersed in the dip-coated solution till the reactor mid-length, in order to locate the catalytic ignition

point at the axial center of the microchannel network. Excess solution was removed by pressurized gas and the procedure was repeated eight times with drying between each coat for 45 minutes at room temperature. The substrate was then calcined at 450^{o}C for 4h with heating and cooling rates of 3^{o}C/min. After coating of combustion catalyst, corresponding reforming channels were packed with $CuO/ZnO/Al_2O_3$ catalyst (Puristar R312, BASF). $CuO/ZnO/Al_2O_3$ pellets of size 5 mm were ground and sieved to between 500 and 700 mm (25-35 mesh) particle size. Approximately 600 mg of reforming catalyst was packed in each channel with Nickel mesh (100 μm; Alfa Aesar) inserted at either end of the reforming channel to retain the packed catalyst during operation. Figure 2.3 shows the unassembled and assembled view of 5x5 ceramic microchannel network packaged with brass distributors.

2.2 Microreactor operation

Combustion/Partial oxidation feed was comprised of a dry gas blend of 20% O_2/5% He/75% Ar and ultra high purity argon to achieve desired O_2 dry basis mole fraction, with approximately 13% methanol supplied by a gas bubbler maintained at 20^{o}C using heating tapes connected to the temperature controller. The reforming feed was comprised of 5% N_2/95% Ar with 2.5% methanol/2.5% water addition from a separate gas bubbler thermostated at 20^{o}C to maintain a steam to methanol ratio (SMR) of unity. Both product streams were dehumidified using a series of moisture traps at 0^{o}C and -80^{o}C and analyzed on a dry basis using a dual-column (Molecular Sieve and Plot Q columns) Agilent MS3000 gas chromatograph employing Ar as the carrier gas. N_2 and

He were used as internal standard gas to compute the outlet flowrate for reforming and combustion/partial oxidation volumes, respectively.

For each combination of reforming and combustion/partial oxidation flowrates studied, the combustion reaction was initially ignited at equivalence ratio of unity; once a stable hotspot was observed, reactant supply to the reforming volume was initiated, and the ER was reduced at intervals of 0.1 from 1 to 0.5. The surface temperature of the microreactor was measured at seven nodal points along the length of the reactor by placing thermocouple probe on the outer surface of the microchannel network. Thermal images were taken using FLIR Thermocam^{TM} infrared camera to capture the hotspot location and magnitude under steady-state operation. Coating of combustion catalyst till the mid-length placed the fuel ignition at the reactor axial mid-point. However, with steady-state data collected at each condition, co-current operation moved hotspot towards combustion/reforming outlet, while counter-current operation resulted in a stable hotspot location at the axial mid-point of the reactor. Therefore, all experiments with all three prototypes were performed in counter-current configuration.

2.3 Results with three prototype reactor designs

2.3.1 Architecture A [checkerboard configuration]

Architecture A was composed of 13 steam reforming channels, alternating with 12 combustion/partial oxidation channels in a 25-channel network. System performance was analyzed at a fixed reforming flow rate of 1600 sccm corresponding to $Re_{ref} = 250$. Three different combustion flow rates (900, 1200 and 1500 sccm) were studied,

corresponding to Re_{comb} = 150, 200 and 250. Combustion equivalence ratio (ER) was varied from 0.5 to 1.

Lowering ER values from 1 to 0.5 led to decrease in methanol conversion in the combustion volume due to decrease in the oxidant supply. This resulted in the reduction of hotspot magnitude from a maximum temperature of 560^{o}C to 260^{o}C. The hotspot had a symmetrical shape and was located at the axial midpoint of the reactor with both distributors maintained at ~50^{o}C. Further reduction in ER resulted in extinction of combustion due to insufficient oxidant supply. Methanol conversion in the reforming channels decreased significantly at ER<0.7 due to a decrease in reactor temperature. The reduction in temperature resulted in increased H_2 yields and reduced CO yields by favoring WGS in the reforming volume. In the combustion volume, reduction in ER led to partial oxidation, which resulted in increased H_2 yields at high combustion flowrates. Overall hydrogen yield reflects the hydrogen produced from steam reforming and partial oxidation. With increase in combustion flow rate, the maximum overall hydrogen yield was observed at lower ER. Maximum overall hydrogen yield of i) 28% was obtained at ER=0.9 and Re_{comb} = 150; ii) ~28% at ER=0.7 and Re_{comb} = 200; iii) 30.3% was obtained at ER=0.6 and Re_{comb} = 250. Overall CO yields of about 32% were observed at high combustion flow rates and at intermediate ER values (ER=0.8). Methane yields were observed only in the combustion volume of <3%. The best performance with Architecture A was achieved at high combustion flowrates with low ERs. (Additional details are provided in Dr.Angela Moreno's Thesis Dissertation [73]).

2.3.2 Architecture B [Annular integration of two volumes]

Architecture B was comprised of 9 combustion/partial oxidation and 16 steam reforming channels, providing an annular integration of two catalytic volumes with a radial distribution pattern representing a conventional shell and tube heat exchanger. Combustion equivalence ratio was varied from 0.5 to 1 for three different reforming flowrates of 1000, 1600 and 2000 sccm corresponding to Re_{ref} = 125, 200 and 250 respectively, at a fixed combustion flow rate of 1125 sccm corresponding to Re_{comb} =250.

Methanol conversion in the combustion channels decreased gradually at ER<0.8 owing to insufficient oxidant supply. Hence the hotspot magnitude decreased from 430^{o}C to 300^{o}C as the ER value lowered from 1 to 0.5 and at high Re_{ref} because of effective heat removal/utilization by the reforming stream. The hot spot was located at the axial mid-point of the reactor with both distributors at temperatures of 40^{o}C-50^{o}C at all conditions. Reforming hydrogen yields were not affected by the change in ER values at low reforming flow rates. But at high reforming flow rates, due to the combined effect of reduced residence times and reduction in reactor temperature, decrease in ER value led to lower methanol conversion and lower hydrogen yields. These results signify the similar observations from Architecture A where the hotspot magnitude decreased at low combustion flow rates and with a decrease in ER. In the combustion volume, decrease in ER value increased H_2 yields by favoring partial oxidation. Maximum overall hydrogen yield of 26% was observed at Re_{ref} = 200 and ER= 0.8. Higher ER values reduced combustion CO yields by favoring complete combustion, whereas increased hotspot

magnitude at higher ERs increased reforming CO yields. Therefore, both combustion and reforming carbon monoxide yields increased with decreasing Re_{ref} at ER=0.8. Similar to Architecture A, reforming volume did not produce detectable methane, whereas in the combustion volume, low methane yields of <1% was detected. Desirable performance was obtained with an increase in reforming flowrates at intermediate ERs. (Additional details are provided in Dr.Angela Moreno's Thesis Dissertation [73]).

2.3.3 Architecture C [Annular integration of three volumes]

Architecture C is comprised of a central combustion channel surrounded by 8 steam reforming channels and an outer ring of 16 heat retention/insulation channels, providing an annular integration of three separate process volumes. The system performance was studied at ER=1 by varying combustion and reforming flow rates in order to effectively compare results obtained from Architecture A and B. Reducing ER<1 led to a significant decrease in hotspot temperature, so insufficient heat to the reforming volume failed to obtain the desired performance from Architecture C.

2.3.3.1 Influence of varying reforming flowrates at fixed combustion flowrate of 500 sccm with ER=1

The overall system performance was studied at a constant combustion flow rate of 500 sccm corresponding to Re_{comb}= 1000 at ER=1 for reforming flow rates of 400, 600, 800, 1000 and 1200 sccm corresponding to Re_{ref}= 100, 150, 200, 250 and 300 respectively. Increase in the reforming flowrate contributed to dispersion of combustion

heat, resulting in decreased hot spot magnitude from 300 to 270^{o}C and a shift in hot spot location towards the combustion inlet/ reforming outlet.

The combustion flowrate of 500 sccm at ER=1 resulted in complete combustion of methanol, as evidenced by negligible traces of hydrogen and CO obtained in the combustion effluent. Hydrogen yield in the reforming volume decreased slightly with an increase in reforming flowrate due to a likewise reduction in methanol conversion owing to decreasing residence time. Overall hydrogen yield increased from 10% to ~30% with increase in reforming flowrate. Overall carbon monoxide yield increased from 3% to 8% with increase in reforming flowrate whereas methane was only observed in the combustion volume at mole fractions of <0.3%.

2.3.3.2 Influence of varying combustion flowrate with ER=1 at fixed reforming flowrate of 1000 sccm

By maintaining the reforming flowrate constant at 1000 sccm corresponding to Re_{ref} = 250, combustion flow rates were varied from 500, 450, 400, 350 and 300 sccm, corresponding to Re_{comb} = 1000, 900, 800, 700 and 600 respectively. Decrease in Re_{comb} from 1000 to 600 resulted in decrease in hotspot magnitude from 250^{o}C to 170^{o}C due to lower methanol conversion in the combustion channel. Further decrease in combustion flowrate (i.e. below 300 sccm) resulted in significant decrease in hotspot magnitude due to inadequate fuel combustion to stabilize the symmetrical hotspot; this eventually led to extinction of combustion. Hydrogen yields in the reforming volume were found to be strongly affected by combustion flow rates. With decrease in the combustion flowrate,

the reaction temperature decreased due to reduced reaction rates, resulting in lower hydrogen yields from the reforming volume. Reformer hydrogen yields plateaued at Re_{comb}>700 to >80%, such that the overall hydrogen yield decreased slightly with further increase in combustion flowrates. The optimal performance for Architecture C was therefore obtained at Re_{comb}=700 with the overall hydrogen yield of 32% and carbon monoxide yield of 4%. No trace of methane was observed in the reforming and combustion volume except at Re_{comb}=1000 with the hotspot temperature of 250^{o}C. The best performance with Architecture C was achieved at low combustion and high reforming flowrates. (Additional details are provided in Dr.Angela Moreno's Thesis Dissertation [73]).

2.4 Conclusion and motivation for primary study

Comparing the best performance of Architecture C with the similar conversions and yields obtained with other two architectures under identical single channel reforming flow rates, showed that the external hot spot magnitude was 360^{o}C, 300^{o}C and 200^{o}C for Architecture A, B and C respectively. Architecture B of an annular pattern integrating two reaction volumes resulted in reduction of external surface temperature of ~50^{o}C compared to Architecture A, whereas the Architecture C with the addition of outer 16 heat retention channels contributed to further reduction of reactor surface temperature of ~100^{o}C. Therefore, variation in configuration showed 50-150^{o}C difference in three-dimensional hotspot magnitude and suggested that the distribution pattern obtained from Architecture C was most effective for radial insulation. Low CO

yields of about 3 - 8% were obtained from Architecture C compared to Architecture's A & B (~30%), which provides less need for H_2 purification. Thus, proper selection of two-dimensional radial distribution pattern aids in attaining substantial thermal gradient for enhancing self-insulation as well as overall hydrogen yields. In Architecture C, high combustion flow rates resulted in reduction of net hydrogen yield. Above results also indicated that with the combustion flowrate of 500 sccm, increase in reforming flowrate showed an increasing trend in overall hydrogen yield. Therefore, the increase in reforming flowrate along with minimization of combustion fuel is expected to provide improved system performance. However, for the initial catalyst configuration, the hotspot location was highly sensitive to both reforming and combustion flows. Variation in catalyst configuration is proposed as a viable means of preventing hotspot mobility from the axial center of the reactor, allowing a much broader range of process flows to be investigated. With the decrease in combustion flowrate (<300sccm), extinction of combustion occurred due to insufficient fuel & oxidant. Whereas at high reforming flowrates, the hotspot was moved towards the combustion inlet/reforming outlet. The primary research goal of this thesis is to fully explore and understand the impact of process flowrates upon overall thermal efficiency and hydrogen yield in the thermally integrated microchannel reactor network. This is accomplished experimentally using the 5x5 Architecture C selected through this preliminary study.

3. INFLUENCE OF PROCESS FLOWRATES UPON OVERALL HYDROGEN YIELD IN A CERAMIC HEAT-EXCHANGER MICROREACTOR

Preliminary studies (summarized in Chapter 2) confirm that a radial distribution pattern coupling a central combustion channel with eight surrounding steam reforming channels and an outer 16 heat retention channels (Architecture C), provides sufficient radial insulation to maintain 50^{o}C-150^{o}C difference between expected inner maximum temperature/external surface temperatures [72]. Using catalyst washcoating for the combustion reaction, this architecture was capable of stable operation at combustion flowrates varying from 300 to 500 sccm and reforming flowrates varying from 400 to 1200 sccm, corresponding to an overall hydrogen yield of 20-32% without any external insulation to the microchannel network. This chapter details the successful redesign of combustion and reforming catalyst configuration to greatly expand the available parameter space for stable reactor operation by preventing hot-spot migration from the reactor midpoint. Results obtained from a through exploration of this expanded parameter space were presented herein. Findings indicate that appropriate selection of feed and sweep flowrates using the moderated architecture C is capable of achieving H_2 yields in excess of 50% and thermal efficiencies in excess of 80%.

3.1 Microchannel network construction

3.1.1 Initial preparation, dimension

The defect-less 5x5 ceramic microchannel reactor was cut from dense fired cordierite honeycomb monolith purchased from Rauschert Technical Ceramics, Denmark, with a cell density of 72 cells per square inch (CPSI). Each channel is of width 2.5 mm and length 150 mm, such that the overall dimension of the ceramic microchannel reactor is 15 mm X 15 mm X 150 mm. Architecture C, which provided effective radial insulation among the three reactor configurations (discussed in Chapter 2), was chosen for subsequent study enhancing the reactor performance to increase overall hydrogen yield above 50%. Therefore, the heat-integrated ceramic microchannel reactor was designed for an annular distribution pattern of a central methanol combustion channel, 8 adjacent methanol steam reforming channels, with the remaining outer 16 channels providing thermal insulation via flow folding or sealing with stagnant gas. Each face of the reactor was polished using 8” dia. 60/P60 grit abrasive paper to extrude the ceramic reactor to brass distributor. Construction of distributor C was already discussed in Chapter 2 (refer to Section 2.1.1).

3.1.2 Nano-alumina coating

Cordierite channels were coated with nano-alumina slurry in order to close the fine pores of the monolith so that there would not be any crossover between channels. Nano-alumina layers on the cordierite monolith give the reactor a uniform, crack free

surface to reduce pressure drop during operation. Nano-alumina solution was prepared by following the recipe below:

1) Mix Aluminum Oxide nanopowder (<50nm TEM, from Sigma Aldrich) (3 grams) + 20% colloidal aluminum oxide in water (0.05 micron particles, from Alfa-Aesar) (1.5 grams) + distilled H_2O (31.5 grams) + methanol (31.5 grams) in a container.
2) Dip the cordierite microchannel reactor into the nanopowder alumina slurry for 5 minutes and sonicate it for 1 hr at room temperature.
3) After sonication, dry the sample for 1 hr at room temperature.
4) Repeat the above procedure (2) & (3) for three times.
5) Blow out the excess solution inside the ceramic channel by passing air at low velocity to get smooth nano-alumina layer inside the reactor.
6) Calcine the cordierite reactor at 650^{o}C for 4 hr with a heating and cooling rate of 3^{o}C/min in the furnace.

Once the nano-alumina coating was completed, a leak test was performed to check crossover between channels by passing 20% O_2/5% He/Ar to the combustion channel and 5% N_2/Ar to the reforming channels. If any crossover was observed, the monolith was again coated with nano-alumina slurry once or twice and calcined at 650^{o}C with the heating and cooling rate of 3^{o}C/min.

3.1.3 Optimized combustion catalyst configuration

As discussed in Chapter 2, the performance of the microchannel network can be enhanced by increasing the reforming flowrate with minimum amount of fuel addition in

the combustion volume. The main challenge associated with reducing the combustion flowrate was the stabilization of the hotspot at the axial mid-point of the reactor; this is necessary to maintain reactor temperature with minimum heat losses in order to achieve desired thermal efficiencies at high reforming flowrates. The selective washcoating of 1 wt% Pt/Al_2O_3 catalyst up to the mid-point of the reactor prevented the hotspot migration at the expense of allowing extinction of combustion process at low combustion flowrates due to lower methanol conversion. A packed bed of 1 wt% Pt/Al_2O_3 pellets were used to stabilize the hotspot at low combustion flowrates (<400 sccm) by providing sufficient catalyst surface area and additional thermal capacities to anchor the hotspot. The 1 wt% Pt/Al_2O_3 pellets (Sigma Aldrich #232114) were hand crushed either by a pepper mill or mortar and pestle and sieved to achieve a particle size of approx. 500-710 μm. Approximately 0.16-0.18 grams of Pt/Al_2O_3 catalyst was packed inside the combustion channel to a bed length of 3.3 cm along the center of the channel axial length. Nickel mesh (100 μm, Alfa Aesar) of 0.4 cm length was placed on either side of the packed zone in order to retain the combustion catalyst. The remaining open, non-catalyst entrance and exit regions of 5.85 cm length are expected to provide a thermally buffer region to prevent excess heat transport to the packaging/distributors.

3.1.4 Optimized reforming catalyst configuration

The eight reforming channels were packed with BASF Puristar R315 $CuO/ZnO/Al_2O_3$ catalyst, crushed by mortar & Pestle and sieved (25-35 mesh) to a particle size of approx. 500-710 μm. Approximately 0.3 grams of $CuO/ZnO/Al_2O_3$

catalyst was packed inside each reforming channel with a loading length of 6 cm at the axial midpoint of the channel. Nickel mesh (100 µm, Alfa Aesar) of 0.4 cm length was used as a catalyst retainer on either side of the packing. A packing length of 6 cm was selected to allow maximum utilization of combustion heat while maintaining a 4.5 cm open, non-catalytic entrance and exit regions to maximize dispersive heat losses to the outer packaging layers. Figure 3.1 shows the cross-sectional schematic of the ceramic microreactor packed with combustion and reforming catalyst as per Architecture C configuration. Figure 3.2 shows the optimal axial schematic of flow and catalyst configuration in a 25-channeled heat-integrated ceramic microchannel network.

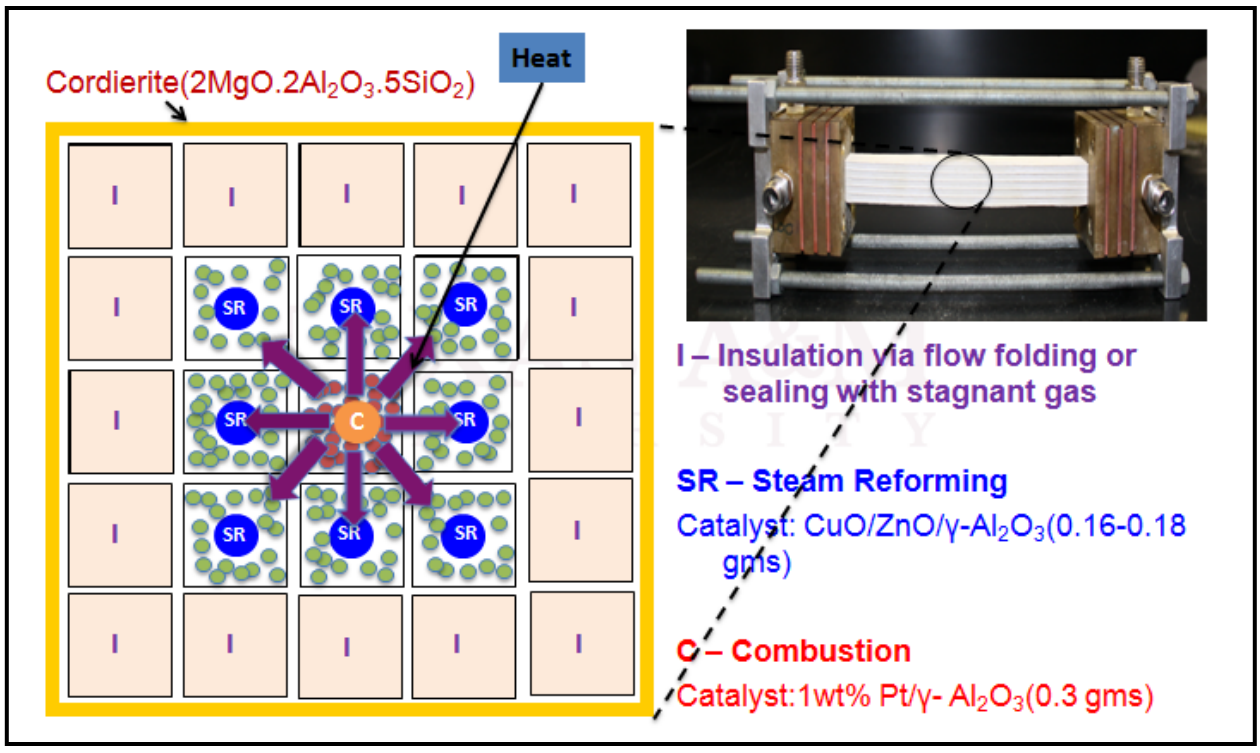

Figure 3.1. Cross-sectional schematic of the microchannel reactor coupling three chemical processes in an annular pattern (Architecture C)

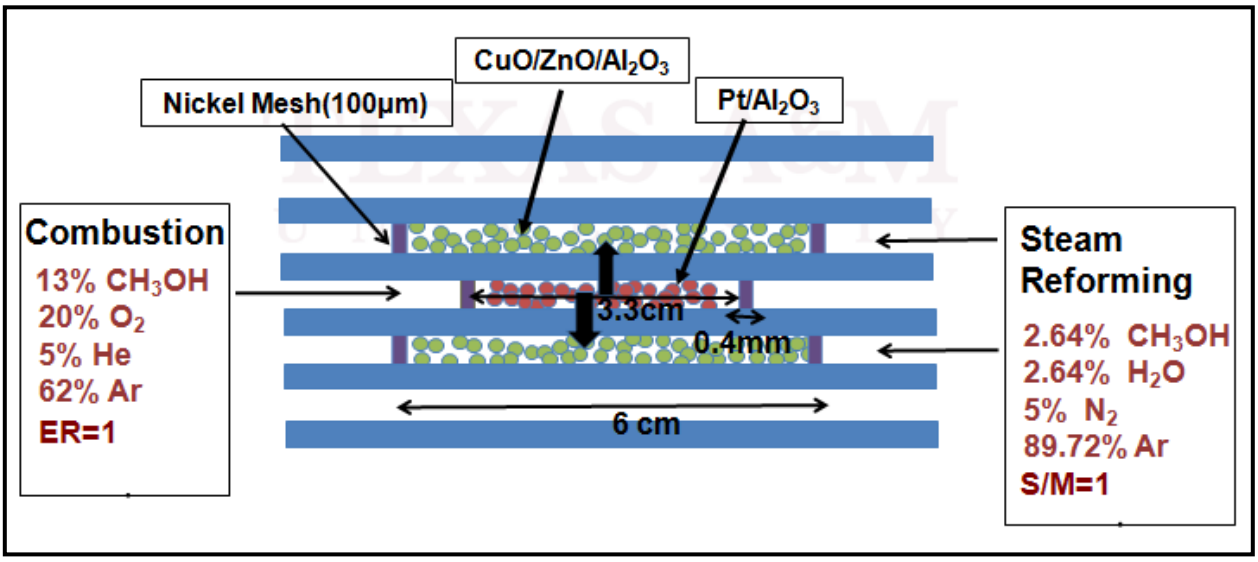

Figure 3.2. Axial schematic of catalyst packing and flow configuration in a 5x5 channeled heat integrated ceramic microchannel network

3.2 Microchannel network assembly

The microchannel network was assembled with the brass distributor on either side of the extruded ceramic reactor with metal chucks on four corners of the distributor. With one distributor fixed at one end of the microchannel reactor; the other distributor was compressed and sealed using four metal adjustable screws. Silicon and graphite gaskets (1/16" McMaster-Carr) were placed on both ends between the recessed face of each distributor block and the extruded ceramic reactor for proper sealing. Figure 3.3 shows the assembled and unassembled view of a 5x5 heat-integrated ceramic microchannel network.

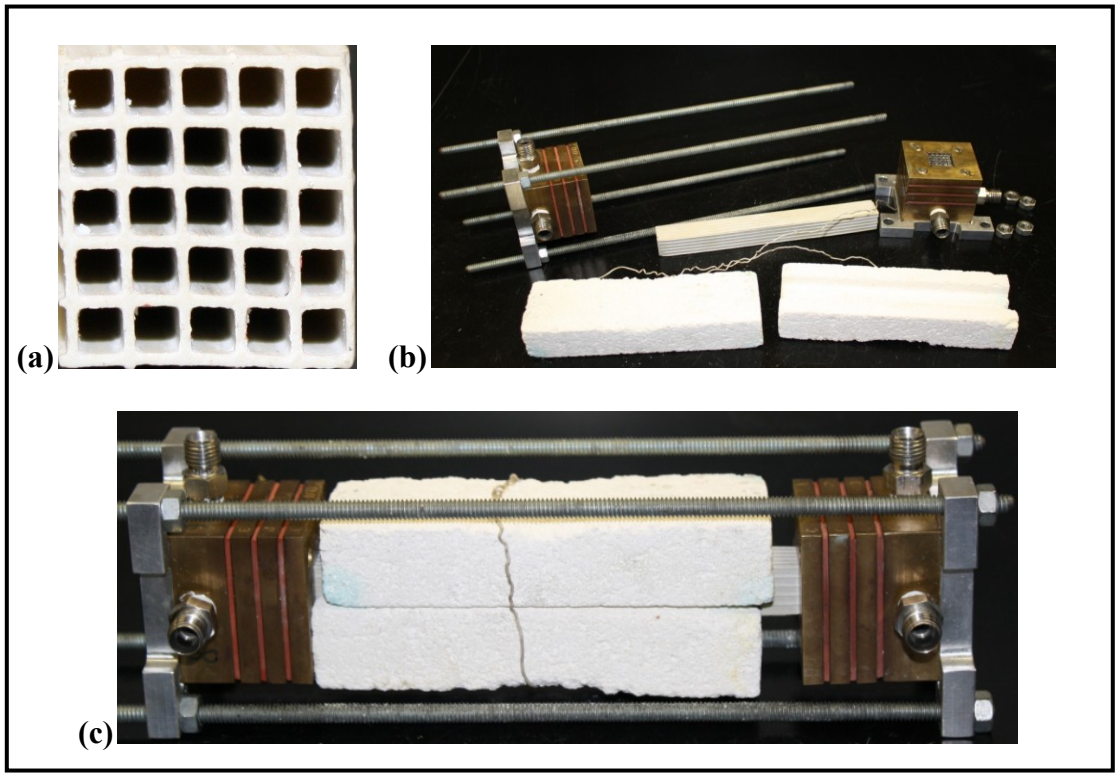

Figure 3.3. Schematic of (a) 5x5 ceramic microreactor (b) unassembled microchannel network showing brass distributors, ceramic microreactor and fire-brick insulation block and (c) unassembled view

3.3 Experimental procedure

Once the microchannel network was assembled, the ceramic microreactor was covered with a fire-brick insulation block of 2.5 cm thickness x 13.2 cm length x 4.2 cm width with metal strips tied tightly on both edges of the reactor for providing external insulation to the system. The bubbler was filled with 400 ml of methanol-water solution (118 mL of methanol and 282 mL of water) with a steam to methanol molar ratio of unity. Heating tape was wrapped around the bubbler and controlled manually using a

variable autotransformer and PID controller (Omega CNi16D44-C24) to maintain a bubbler temperature of 25°C. The methanol vaporizer was filled with 99.9% pure methanol (J.T.Baker) and was maintained at 20°C by heating tape powered by a second PID controller (Omega CNi16D44-C24).

The combustion gas was comprised of a dry gas blend of 20% O_2/5% He/75% Ar with ultra high purity argon and 13% methanol from the vaporizer. The reforming gas was consisted of a dry gas blend of 5% N_2/95% Ar with 2.64% methanol and 2.64% water from the bubbler maintained at 25°C. Combustion (20% O_2/5% He/13% CH_3OH/Ar) and reforming (5% N_2/2.64% CH_3OH/ 2.64% H_2O/Ar) gas streams were passed to their respective channels at atmospheric pressure and temperature through Alicat mass flow controllers. Figure 3.4 shows the schematic of the experimental system.

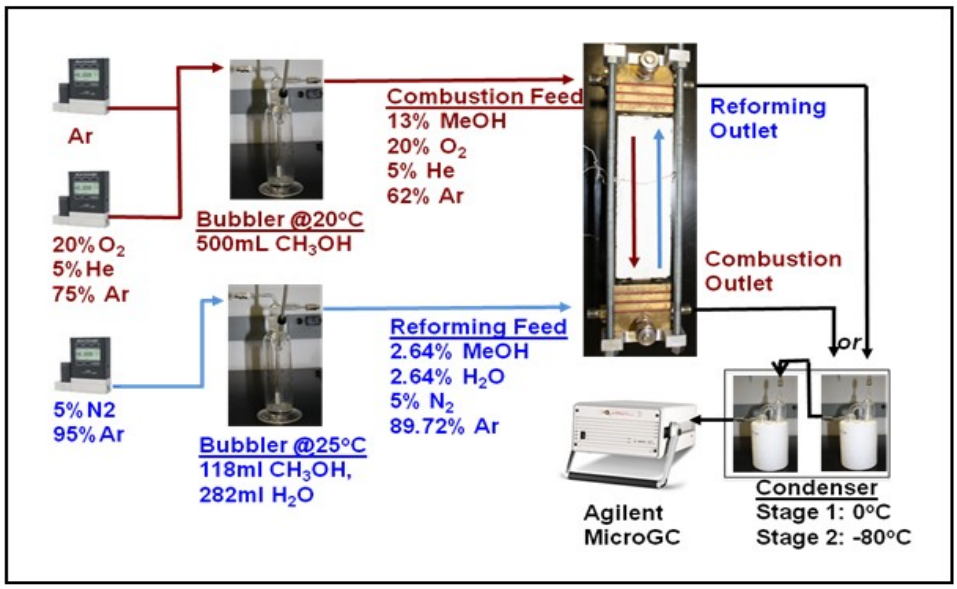

Figure 3.4. Schematic of the experimental system

A thermocouple probe was placed on the outer surface of the microchannel reactor, between the upper insulation block and the ceramic reactor to measure the surface temperature at seven nodal points along the length of the reactor. A 12" long thermocouple probe consisted of 7 K type thermocouples, in which each sensing point was located 1" distance between each point except the last sensing point placed at 0.5" distance. The probe was constructed with a stainless steel (grade 304) protection sheath of 1/16" diameter in which 7 thermocouples were inserted. Thermal images of the microchannel network were obtained using FLIR Thermocam^{TM} infrared camera to capture the hotspot location and magnitude during steady-state operation. Helium and Nitrogen gas were used as an internal standard gas for combustion and reforming volume respectively. Both combustion and reforming product streams were analyzed on dry basis through Agilent MS3000 gas chromatograph using Ar as a carrier gas. Ice (0^oC) and dry ice (-80^oC) condensers were used in series to trap the moisture content in the product streams before passing them to the GC column for analysis. The dual-column Agilent MS3000 MicroGC was consisted of two columns: Molecular sieve and Plot Q columns equipped with a thermal conductivity detector. Both columns were operated at a temperature of 60^oC and column head pressure of 30 and 18 psia respectively. Cerity software was used to export the GC samples to Excel file.

As discussed in Chapter 2, all experiments were performed in counter-current heat exchanger configuration, which offered the best thermal insulation pattern to locate the stable hotspot near to the axial mid-point of the reactor. Both methanol combustion

and methanol steam reforming reaction were initiated at room temperature without addition of external heat to the system. The combustion process was initially ignited at a combustion flowrate of 500 sccm. Once the flame was stabilized, the methanol combustion was run at a desired combustion flow rate and the reforming gas streams were passed to their respective channels by increasing the reforming flowrate from 200 to 2000 sccm at intervals of 200 sccm. Occasionally, issues with self-ignition of combustion process prevailed even at high combustion flowrates, and this was evicted by preheating the microreactor packed with combustion and reforming catalysts to 100^{o}C before starting the combustion process. At high reactor temperatures (>300^{o}C), degradation in activity of the reforming catalyst ($CuO/ZnO/Al_2O_3$) occurred over a time span of 15 hrs due to the reduction of CuO to Cu under reducing environment. For this reason, a new monolith packed with fresh combustion and reforming catalyst was used for each set of experiments. Bubbler solution of 118 mL of CH_3OH and 282 mL of H_2O was replaced for every change in reforming flowrate of 200 sccm or per 3 hrs of time on-stream, in order to ensure consistent reforming gas composition of 2.64% methanol and 2.64% water. For all experiments varying reforming flowrate at a fixed combustion flowrate, 10 samples of both combustion and reforming product streams were analyzed using Agilent MicroGC during steady-state operation. Gas chromatographs were calibrated using an external standard calibration gas provided by Praxair, Inc with known concentrations of each species (H_2, CO, CO_2, CH_4, N_2, O_2, He). The product stream elements were identified with their retention times and individual species' peak areas were analyzed from GC samples to obtain product gas composition.

The O_2/CH_3OH molar ratio for the combustion process was varied for each combustion flow rate by maintaining an equivalence ratio (Eqn 3.1) of unity. Methanol conversion (Eqn 3.2) in both combustion and reforming volume was calculated based on carbon balance i.e. from the outlet molar concentration of methane, CO and CO_2. Combustion and reforming product yields (Eqn 3.3) and selectivities (Eqn 3.5) were calculated from their outlet concentrations on stoichiometric basis. Thermal efficiency (Eqn 3.6) was calculated based on the fraction of combustion heat utilized as sensible heat and to drive the endothermic reaction.

$$ER = \frac{F_{O_2}}{1.5F_{CH_3OH}} \tag{3.1}$$

$$X_{CH_3OH} = \frac{(F_{CO} + F_{CO_2} + F_{CH_4})_{out}}{F_{CH_3OH,in}} \tag{3.2}$$

$$Y_{H_2} = \frac{F_{H_2,out}}{3F_{CH_3OH,in}} \qquad Y_{CO} = \frac{F_{CO,out}}{F_{CH_3OH,in}} \qquad Y_{CO_2} = \frac{F_{CO_2,out}}{F_{CH_3OH,in}} \tag{3.3}$$

$$Overall\_Y_{H_2} = \frac{F_{H_{2out},C} + F_{H_{2out},R}}{3(F_{CH_3OH_{in},C} + F_{CH_3OH_{in},R})} \tag{3.4}$$

$$S_{CO} = \frac{F_{CO,out}}{F_{CO} + F_{CO_2} + F_{CH_4}} \tag{3.5}$$

$$\eta_{thermal} = \frac{Q_{used,\mathrm{Ref}}}{Q_{added,Comb}} \tag{3.6}$$

3.4 Results & discussion

3.4.1 Refinement of catalyst distribution

Results of Architecture C (discussed in Chapter 2) using a reforming catalyst packed bed length of 14 cm and a fluid washcoating of Pt/Al_2O_3 catalyst in the combustion channel showed that the location of hotspot was shifted towards the combustion inlet/reforming outlet at high reforming flowrates owing to higher combustion heat dispersion by the reforming stream and an insufficient ability of the combustion channel to store reactor heat at the desired hot-spot location. To address this issue, a packed bed of combustion catalyst was introduced to allow retention of combustion heat within the microchannel at low flowrates. After stabilizing the hotspot at low combustion and high reforming flowrates by packing the combustion channel with Pt/Al_2O_3 pellets, the next challenge raised was the hotspot location. Various catalyst configurations (shown in Figure 3.4) were analyzed both in combustion and reforming volume to locate the stable hotspot at the axial mid-point of the microreactor; thereby, enhancing the thermal efficiency of the microchannel network by minimizing axial heat losses via packaging.

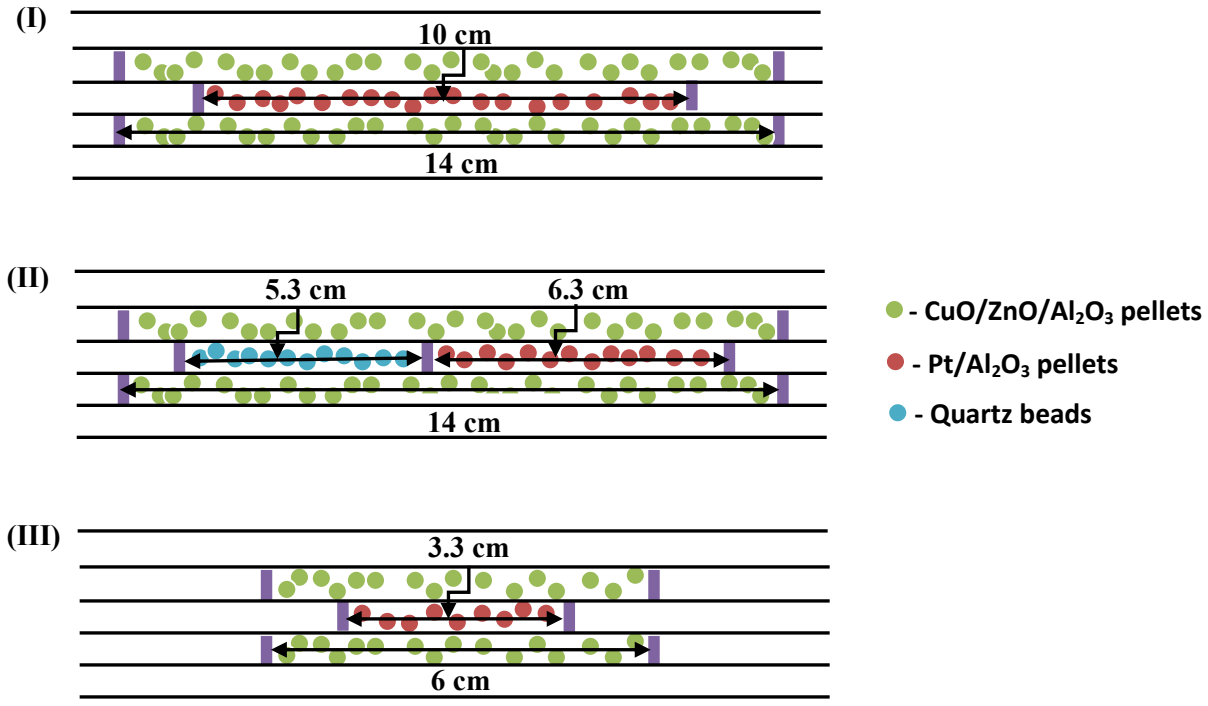

Figure 3.5. Schematic of three different catalyst configurations studied to place the hotspot at the axial mid-point of the reactor

3.4.1.1 Configuration I

The first catalyst configuration of the microchannel network was consisted of 0.38 g of Pt/Al_2O_3 pellets in the combustion channel with a loading length of 10 cm and 14 cm of $CuO/ZnO/Al_2O_3$ pellets (0.6 g) as reforming catalyst. With this configuration, though the hotspot was stabilized at low combustion flowrates even with an increase in reforming flowrates (Re_{ref} = 300 and varying Re_{comb} = 1000 to 500), the hotspot was positioned at the inlet region of the combustion catalyst, which corresponded to

approximately 1” away from the combustion inlet/reforming outlet or 6.5” away from the mid-point of the reactor network.

3.4.1.2 Configuration II

To shift the ignition point closer to the axial mid-point of the reactor, the above configuration was modified by packing the combustion channel with a 5.3 cm inlet zone of non-catalytic quartz beads (0.33 g) followed by 6.3 cm of Pt/Al_2O_3 pellets (0.28 g), while retaining a reforming catalyst packing zone of 14 cm length. Replacing the initial 5.3 cm of combustion catalyst with quartz beads successfully placed the ignition point and hot-spot center at the axial mid-point of combustion channel, without any reduction in the overall thermal capacity of the combustion channel. However, excess heat dispersion along the entire 11.6 cm of quartz and catalyst packing resulted in poor ignition behavior at low combustion flowrates (below 500 sccm).

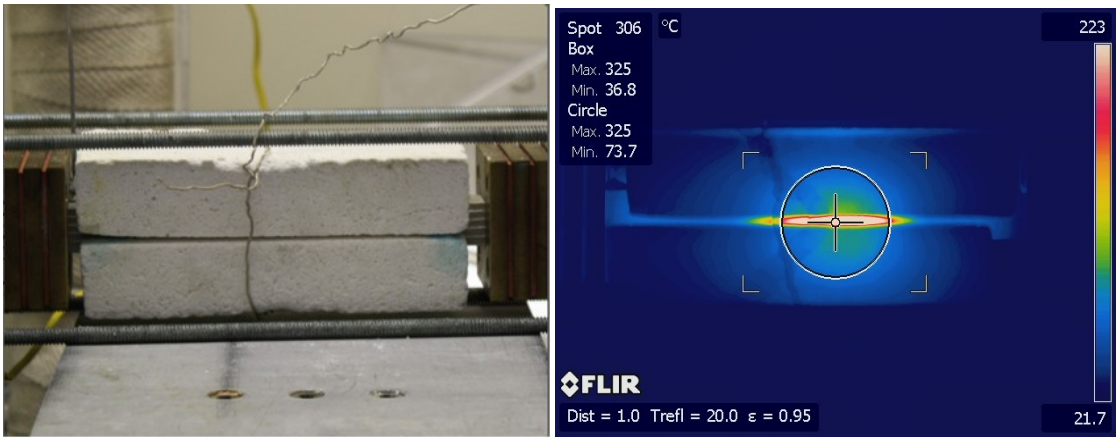

Figure 3.6. Hotspot was placed at the axial mid-point of the microreactor maintaining the distributor ends <50^{o}C

3.4.1.3 Configuration III

The final configuration of 3.3 cm of Pt/Al_2O_3 pellets (0.16-0.18 g) as combustion catalyst with 6 cm of reforming catalyst ($CuO/ZnO/Al_2O_3$) along the center of the reactor resulted in efficient performance (Overall H_2 yield of 40% at Re_{comb} = 600 and Re_{ref} = 375) of the microchannel network by providing sufficient catalyst packing mass to allow heat storage/hotspot stabilization, while minimizing the extent of heat dissipation by conduction along the packing length. This resulted in a stable hotspot (shown in Figure 3.5) located at the axial midpoint over the range of process flowrates studied. Loading length of reforming catalyst ($CuO/ZnO/Al_2O_3$) was decreased from 14 cm (0.6-0.7 g) to 6 cm (0.3 g) compared to other two configurations to place the catalytic active site for both processes at the axial mid-point and to maximize the heat utilization by the reforming stream by minimizing axial heat loss due to conduction/dispersion through the packed catalyst.

3.4.2 Influence of combustion and reforming flowrates

The main aim of this study was to find the influence of process flowrates both on combustion and reforming volume in order to increase the overall hydrogen yield above 50% by enhancing the thermal efficiency of the system through positioning the hotspot at the axial mid-point of the reactor. The system performance was analyzed by varying the reforming flowrate from 200 to 2000 sccm corresponding to Re_{ref} = 50, 100, 150 to 500 respectively, for each combustion flowrate of 200, 250, 275, 300 and 400 sccm corresponding to Re_{comb} = 400, 500, 550, 600 and 800 respectively.

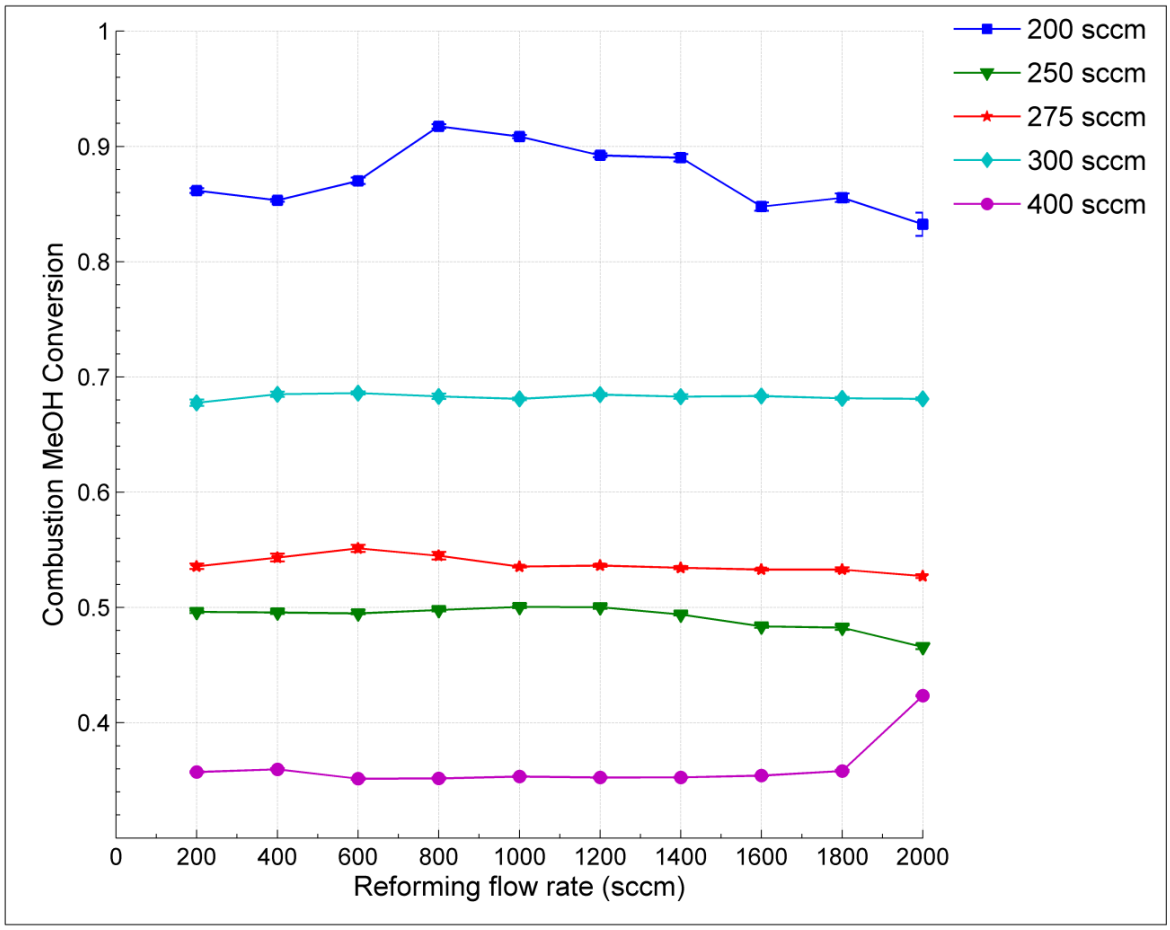

Figure 3.7. Effect of combustion and reforming flowrates on methanol conversion in the combustion volume

Figure 3.7 shows that the performance of combustion volume was not affected with the variation in reforming flowrates. The methanol conversion in the combustion volume (shown in Figure 3.7) was almost constant and conversion was high at low combustion flowrate due to high residence time in the reactor.

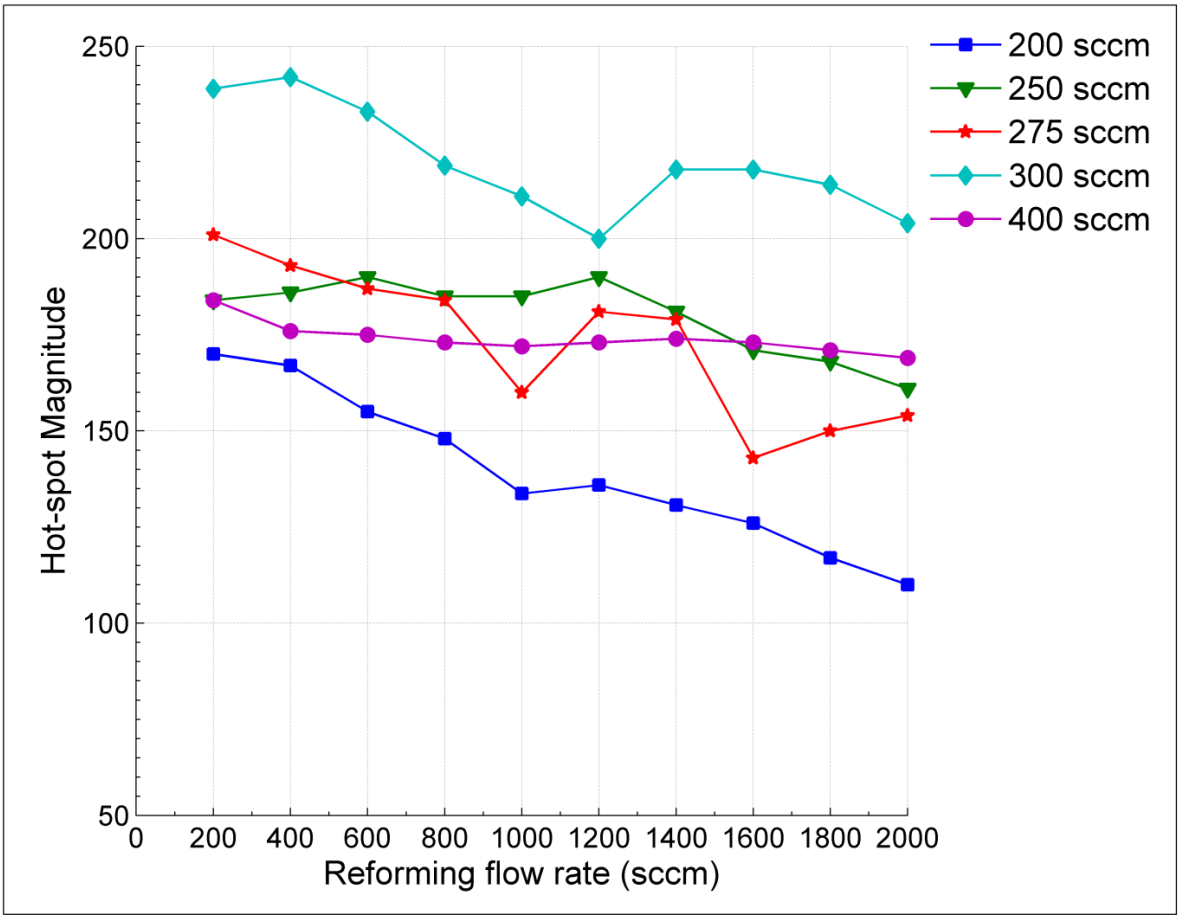

Figure 3.8. Effect of combustion and reforming flowrates on the hotspot magnitude

The hotspot magnitude increased with an increase in combustion flowrate and resulted in a decreasing temperature profile with an increase in reforming flowrate due to increased heat dispersion by the reforming stream (shown in Figure 3.8). With an increase in combustion flowrate, higher hotspot temperatures were maintained even at high reforming flowrates, providing efficient reactor performance at high reforming

flowrates. A maximum hotspot temperature of ~240^{o}C was achieved with the process flowrates employed in this study, which favors high H_2 productivity from methanol steam reforming.

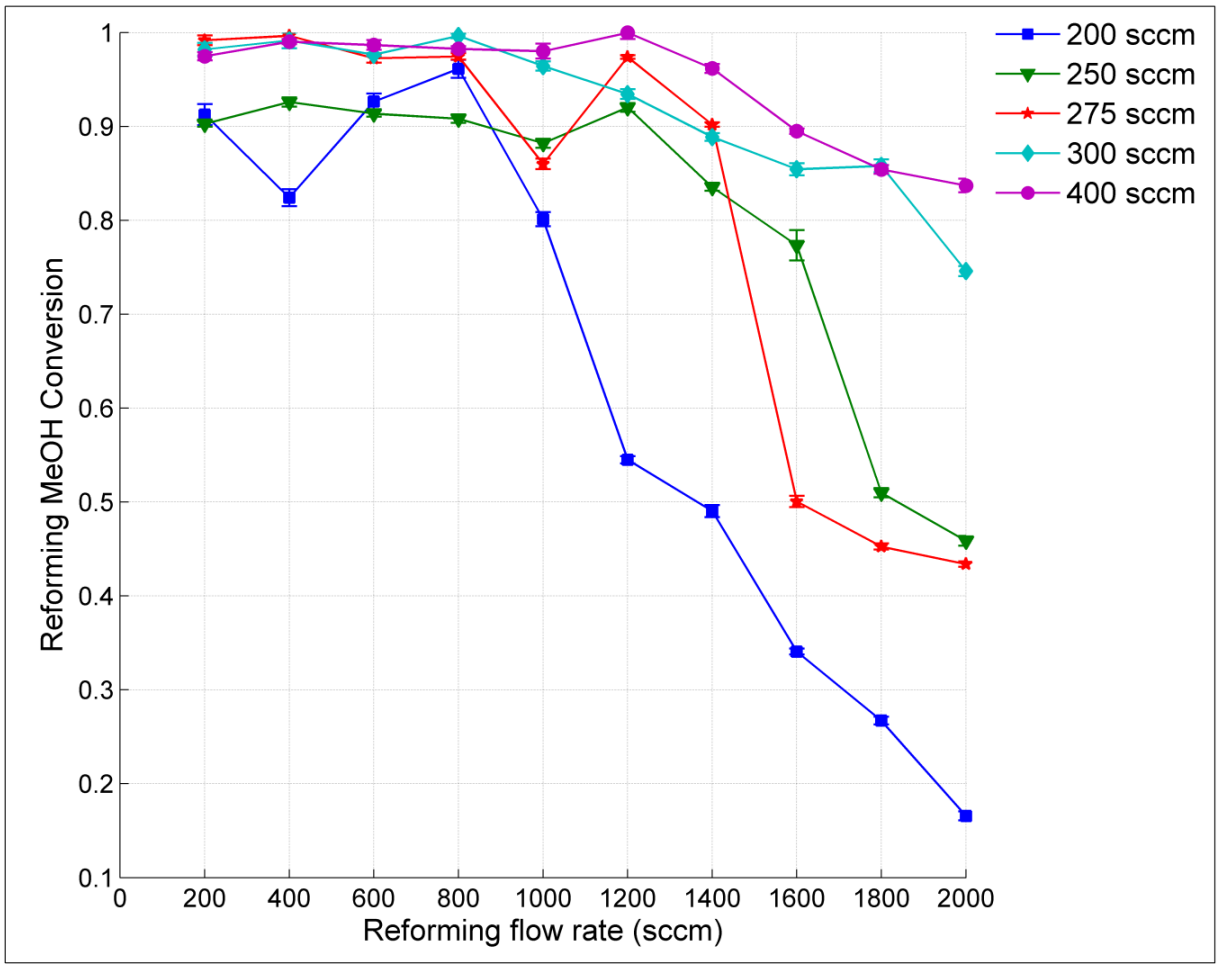

Figure 3.9. Effect of combustion and reforming flowrates on methanol conversion in the reforming volume

With the catalyst configuration discussed in Section 3.4.1.3, the hotspot was placed near to the axial mid-point of the reactor by maintaining the distributor ends at

<50^{o}C at all experimental conditions. In steam reforming channels, more than 95% methanol conversion (shown in Figure 3.9) was observed at low reforming flow rates and was reduced gradually with an increase in reforming flowrate due to the decrease in residence times in the reactor. At low combustion flowrates, methanol conversion in the reforming volume decreased significantly with an increase in reforming flowrate, because of insufficient heat supply to the reforming reaction to occur at higher flowrates. With an increase in combustion flow rate, the reaction rate was increased, which in turn increased the hotspot magnitude as well as the width, so that the methanol conversion at higher reforming flow rates was increased.

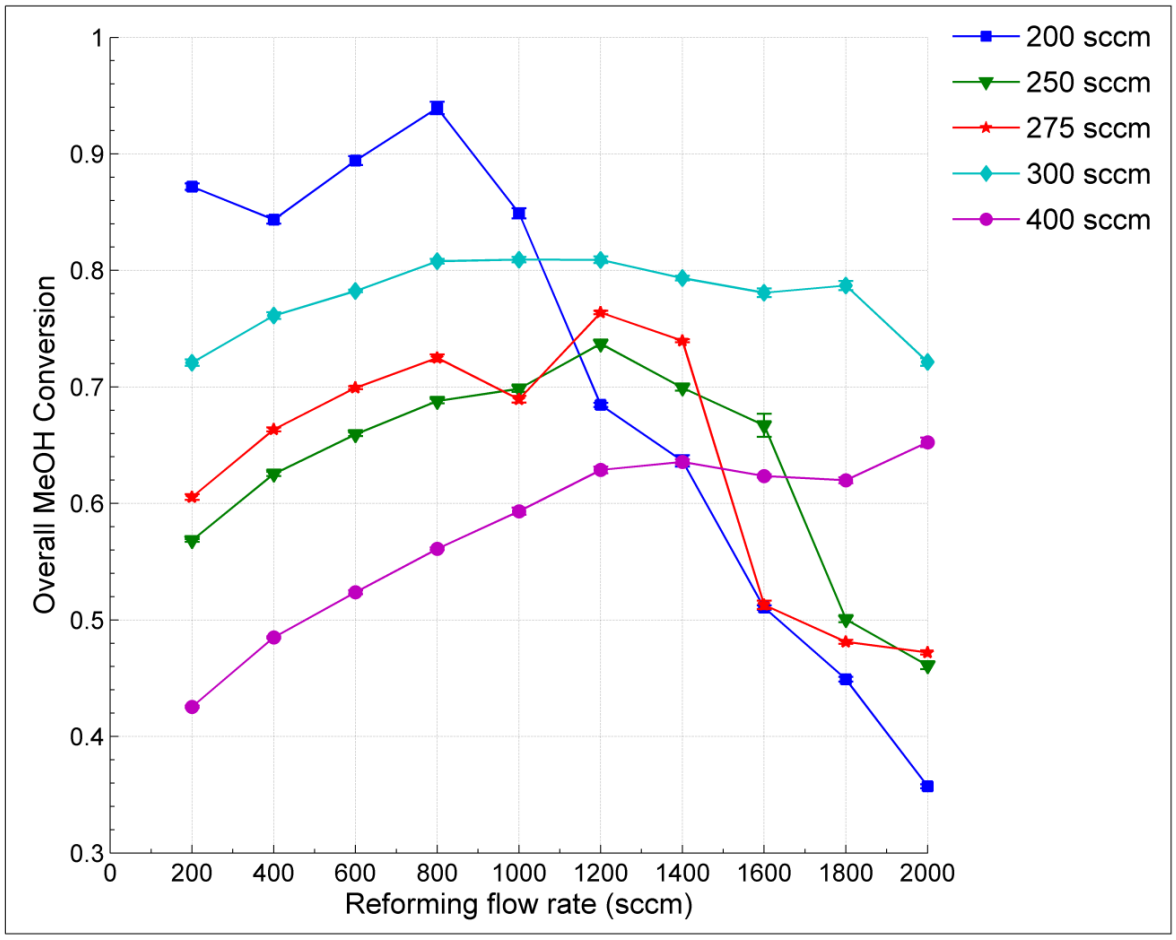

Figure 3.10. Effect of combustion and reforming flowrates on overall methanol conversion

At low combustion flowrates, though the conversion was high, the heat produced was not sufficient for higher reforming flows. Therefore, by increasing the combustion flowrate, the reactor temperature and the hotspot width had increased, which provided sufficient heat and an increased active catalytic site for methanol decomposition to occur at high reforming flowrates. Thus, the overall methanol conversion (shown in Figure

3.10) was increased at high reforming flowrates with an increase in combustion flowrate, in order to increase the overall hydrogen yield by enhancing the thermal efficiency of the system.

Increase in combustion flowrate resulted in complete oxidation of methanol, which was evidenced by negligible hydrogen yields from the combustion volume. Detectable hydrogen yields were observed only at a low combustion flowrate of 200 sccm, where partial oxidation of methanol occurred along with complete combustion which gave traceable amount of hydrogen in the combustion volume.

Higher hydrogen yields of >90% were observed in steam reforming channels (shown in Figure 3.11) at low reforming flowrates, and they started decreasing with an increase in reforming flowrate due to a decrease in methanol conversion with reduced residence times. An increase in combustion flowrate resulted in increased hotspot magnitude due to greater reaction rates. Thus, hydrogen yields at high reforming flow rates were improved due to increased heat dispersion by the reforming stream. Therefore, by increasing the reforming flowrate with an increase in combustion flowrate, sufficient reactor temperature was maintained, which favored both methanol decomposition and water gas shift reaction to increase hydrogen yields and lower CO yields in the reforming volume.

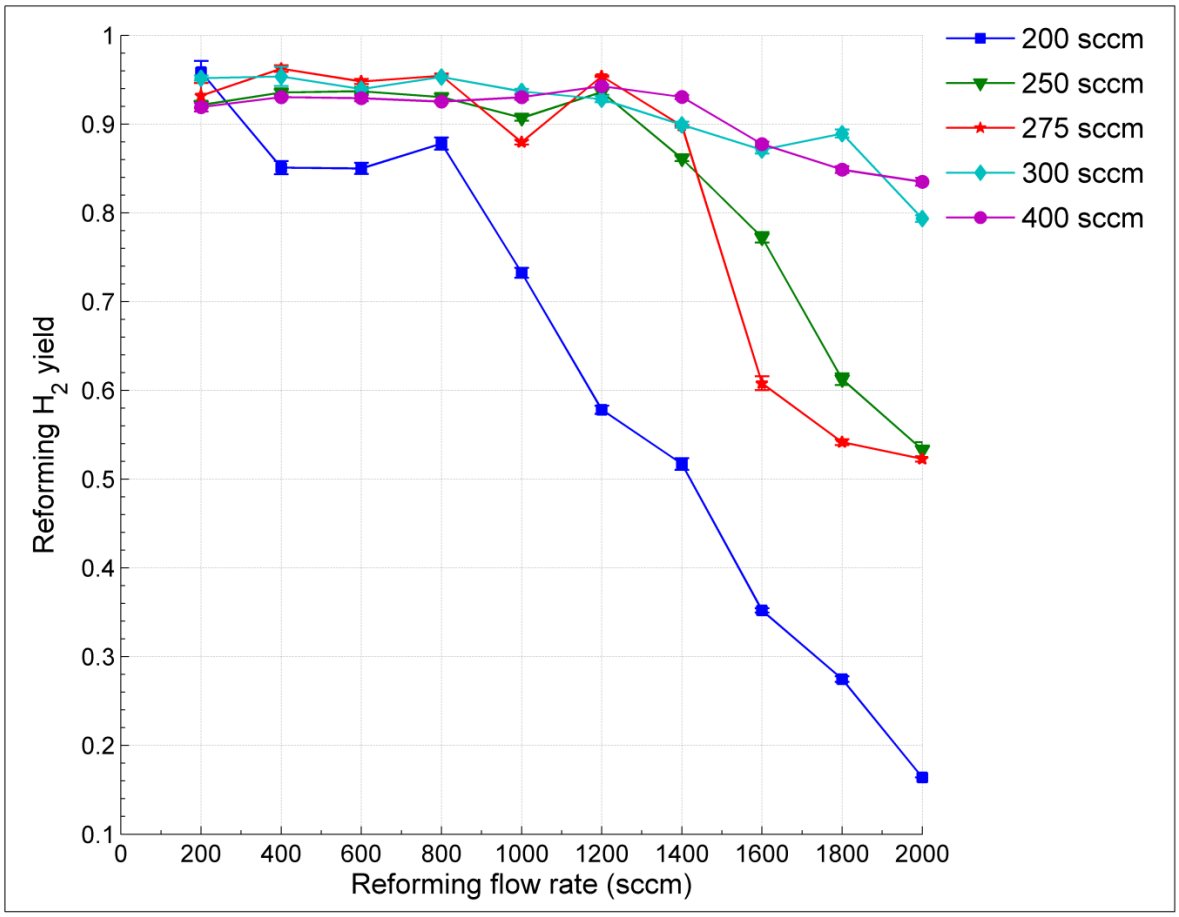

Figure 3.11. Effect of combustion and reforming flowrates on hydrogen yield in the reforming volume

Figure 3.12 provides the overall hydrogen yield of the system combining the hydrogen generated from steam reforming and combustion volume, which was increased with an increase in reforming flowrate. The maximum overall hydrogen yield was achieved at higher reforming flow rates with an increase in combustion flowrate.

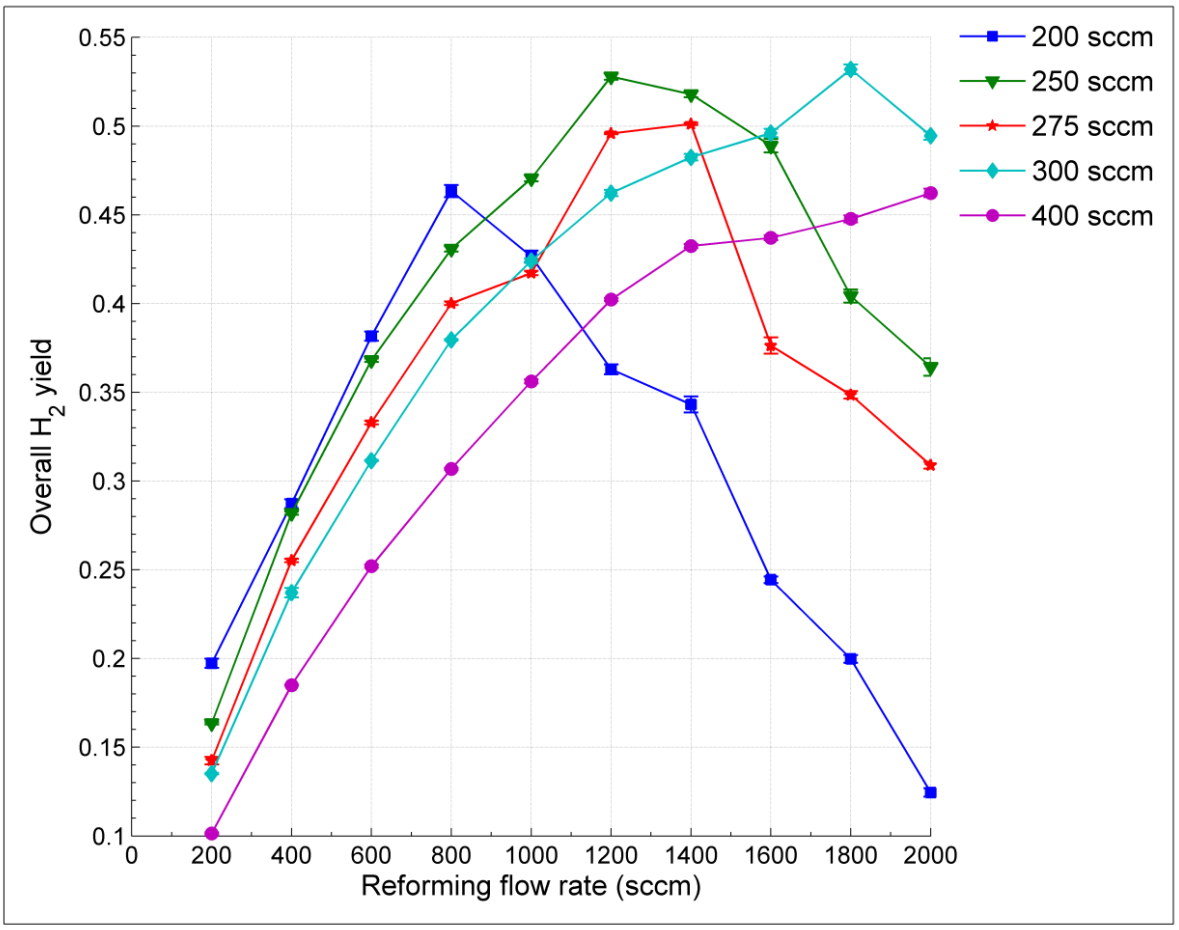

Figure 3.12. Effect of combustion and reforming flowrates on overall hydrogen yield

The maximum overall hydrogen yield of 53.2% was achieved at a combustion flowrate of 300 sccm and reforming flowrate of 1800 sccm. Table 3.1 provides the

maximum overall hydrogen yields and thermal efficiencies obtained with combustion flowrate of 200, 250, 275, 300 and 400 sccm.

Table 3.1. Maximum overall H_2 yield and thermal efficiencies at different combustion flowrates

Combustion flowrate (sccm)	Reforming flowrate (sccm)	Overall H_2 yield	Thermal Efficiency
200	800	46.3%	25.96%
250	1200	52.8%	57.1%
275	1400	50.1%	55.6%
300	1800	53.2%	50.76%
400	2600	52%	88.5%

No trace of carbon monoxide was detected from the combustion channel at high combustion flowrates due to complete oxidation of methanol. At a low combustion flowrate of 200 sccm, partial oxidation of methanol provided 7-14% carbon monoxide yields in the combustion channel. With an increase in combustion flowrate, the hotspot temperature had increased which favored methanol decomposition as well as reverse WGS reaction; hence, the CO selectivity (shown in Figure 3.13) in the reforming volume was increased with an increase in combustion flow rate. A decreasing temperature profile was observed in the reforming volume with an increase in reforming flow rate. Therefore, CO selectivity was reduced with the increase in reforming flow rate by

favoring forward water gas shift (WGS) reaction. The overall carbon monoxide yields were observed to vary from 3-18% with the combustion and reforming flowrates studied in these experiments.

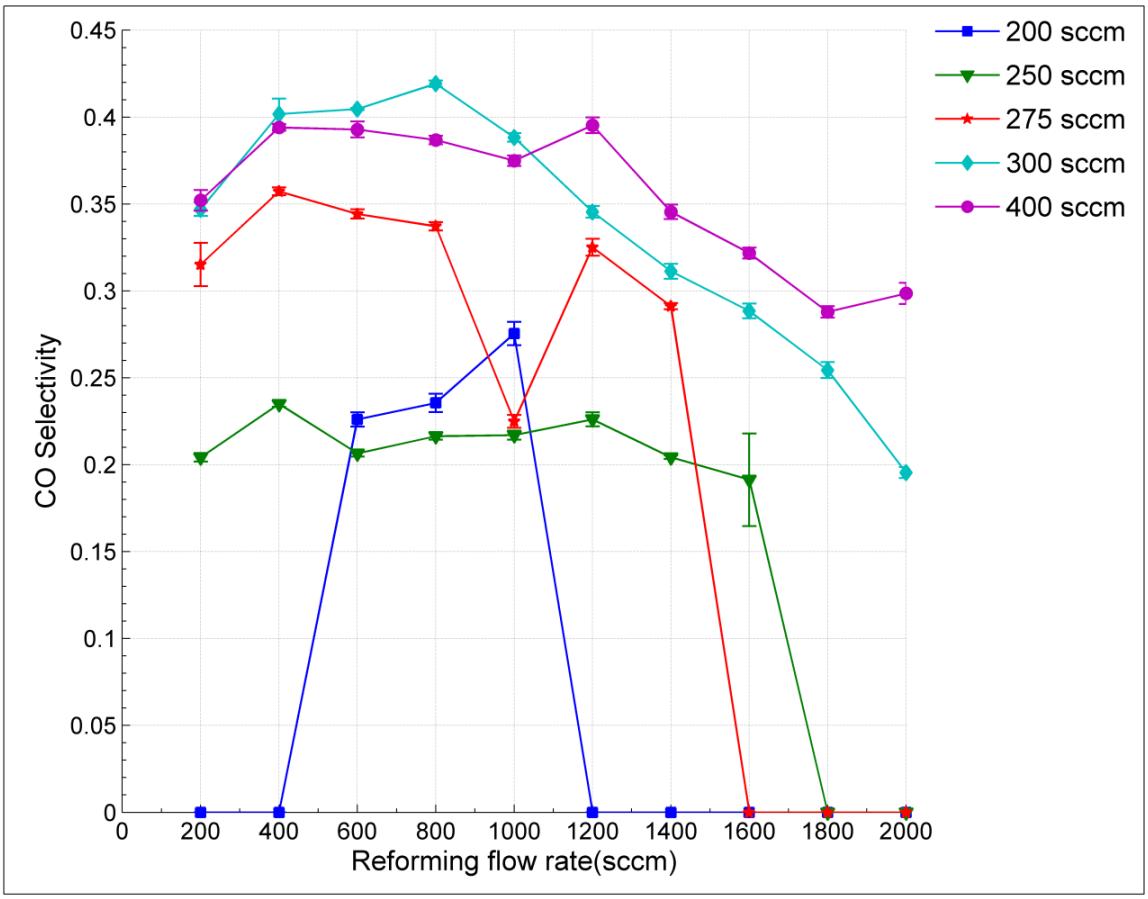

Figure 3.13. Effect of combustion and reforming flowrates on the carbon monoxide selectivity

Methane yields were negligible at all combinations of combustion and reforming flowrates studied. CO_2 was the main component produced in the combustion channel for all the flowrates examined in these experiments.

With the combustion to reforming reaction enthalpies of 13:1, the single combustion channel produced enormous heat than that required for eight reforming channels. Efficient thermal insulation to the microchannel network was expected to enhance the thermal efficiency of the system by minimizing radial and axial heat losses. At a high combustion flowrate, though the methanol conversion was less, more heat had been retained and utilized by the reforming volume at high reforming flowrates by minimizing convective heat losses to the ambient. Thus, the thermal efficiency of the system was increased with an increase in reforming flowrate (shown in Figure 3.14), which resulted in increasing overall hydrogen yield. With minimal external insulation to reduce radial heat losses of the microchannel network, the thermal efficiency of above 80% was attained in these experiments.

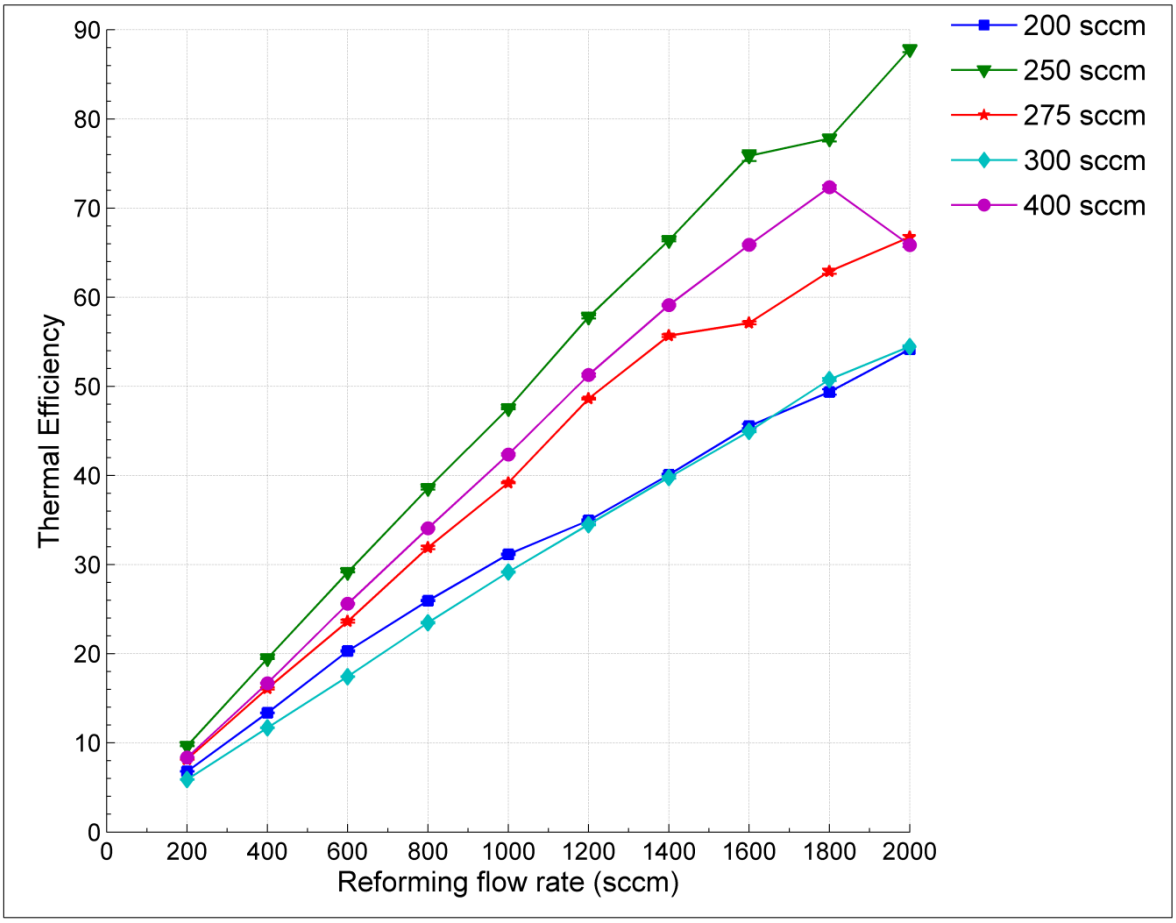

Figure 3.14. Effect of combustion and reforming flowrates on thermal efficiency of the system

3.5 Conclusions

This study established the influence of combustion and reforming process flowrates upon increasing the overall hydrogen yield and thermal efficiency of a 5x5 heat-integrated ceramic microchannel network. The thermal efficiency of the microchannel network was improved with an increase in reforming flowrate due to

enhanced heat retention in the reactor volume with (i) outer 16 insulation channels along with fire-brick external insulation and (ii) by maintaining the hotspot near to the axial mid-point of the reactor, which resulted in increased axial and radial insulation to the system. The catalyst configuration of 3.3 cm of Pt/Al_2O_3 pellets (0.16-0.18 g) in the combustion channel with 6 cm of $CuO/ZnO/Al_2O_3$ pellets (0.3 g) in the reforming channels, helped in maintaining the stable hot-spot near to the axial mid-point of the reactor at all combinations of flowrates studied using Architecture C configuration. Combustion process at an equivalence ratio of unity led to complete oxidation of methanol at higher combustion flowrates (>200 sccm), so no measurable hydrogen yields were obtained from the combustion volume, whereas higher hydrogen yields of >90% was achieved in the reforming volume. An increase in combustion flowrate provided sufficient reactor temperature to increase hydrogen yields at high reforming flowrate by favoring methanol decomposition and water gas shift reaction. Overall hydrogen yield increased with increasing reforming flowrate and the maximum overall H_2 yield was obtained at higher reforming flowrates with an increase in combustion flowrate. CO yields decreased significantly with an increase in reforming flowrate by reducing the hotspot temperature, and negligible CO yields were observed at low combustion flowrates. Net H_2 yield of >50% and thermal efficiency of >80% was achieved from methanol with minimal insulation to the heat-integrated ceramic microchannel network. Increasing the combustion and reforming flowrates led to additional heat loss via reducing the heat recovery from these streams. Therefore, preheating reforming/combustion inlet gases and utilizing the heat from

reforming/combustion outlet gases using outer 16 heat retention channels was expected to further increase the overall hydrogen yield by enhancing the thermal efficiency of a 25 channeled heat-integrated ceramic microchannel network.

4. AN EXPERIMENTAL STUDY ON FOUR DIFFERENT REACTOR CONFIGURATIONS TO FURTHER INCREASE OVERALL HYDROGEN YIELD IN A CERAMIC MICROCHANNEL NETWORK

The previous experimental study (discussed in Chapter 3) on analyzing the influence of combustion and reforming process flowrates by appropriate catalyst loading showed promising results for increasing overall hydrogen yield above 50% by enhancing the thermal efficiency of a heat-integrated microchannel network. Architecture C with a central combustion channel, eight steam reforming channels and the outer 16 heat retention channels for insulation via flow folding or sealing with stagnant gas offered excellent radial distribution pattern to the thermally-coupled microchannel network. The thermal efficiency of the system was enhanced by minimizing the radial and axial heat losses by (i) employing a light-weight fire-brick insulation block as external insulation to the heat-integrated ceramic microreactor and (ii) placing the hot-spot at the axial mid-point of the reactor. With this design, a maximum overall hydrogen yield of 53% was achieved at a combustion flowrate of 300 sccm and reforming flowrate of 1800 sccm, whereas Moreno's study with Architecture C provided 32% overall hydrogen yield at combustion flowrate of 350 sccm and reforming flowrate of 1000 sccm. Increase in combustion and reforming process flowrates led to additional heat loss through their outlet gases. Thus, the subsequent study was focused on further enhancing the self-insulating nature of the microchannel network by utilizing the heat from the reforming/combustion outlet gases or preheating reforming/combustion inlet gases. Four

different reactor configurations were investigated to analyze the reactor performance for enhanced efficiencies using the outer 16 channels in Architecture C.

4.1 Configurations of study

The reactor performance was enhanced by utilizing the heat in the combustion/reforming product streams or preheating the combustion/reforming inlet streams. The thermal efficiency of the microchannel network was improved by minimizing the convective heat losses and increasing the heat retention in the reactor through sealing the outer 16 channels with combustion/reforming inlet/outlet gas streams. Figure 4.1 shows the schematic of four different flow configurations studied to analyze the system performance in order to improve the overall hydrogen yield.

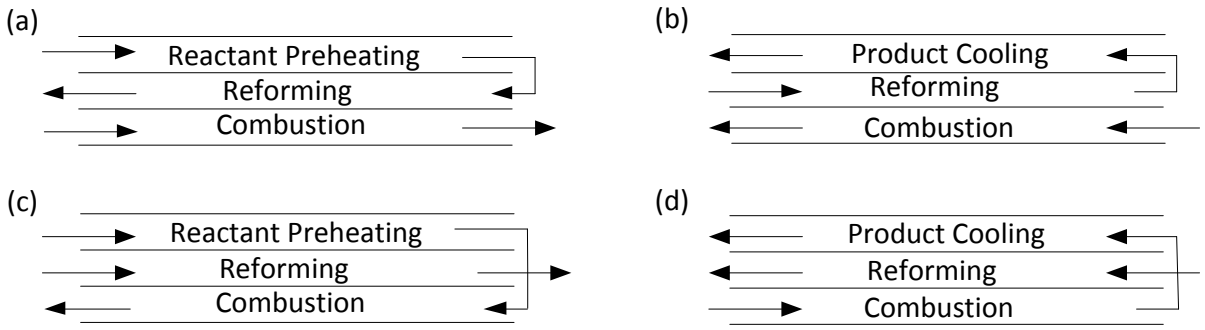

Figure 4.1. Schematic of four reactor configurations using the outer 16 channels of Architecture C for (I) preheating the reforming inlet stream (II) sealing with reforming product stream (III) preheating combustion inlet (IV) Insulation via sealing with combustion product stream

4.1.1 Configuration I

The first configuration (shown in Figure 4.1a) was experimented to preheat the reforming stream before passing them to the respective eight steam reforming channels. The convective heat from the combustion/reforming catalytic volumes was utilized to preheat the reforming stream in the outer 16 channels, which enhances the yields and selectivities of the reforming volume.

4.1.2 Configuration II

The second configuration (shown in Figure 4.1b) was performed by sealing the outer 16 channels with the reforming outlet stream. The heat from the reforming outlet stream was utilized to increase the performance of the reforming volume by improving the heat retention in the network.

4.1.3 Configuration III

The third configuration (shown in Figure 4.1c) was carried out by preheating the combustion stream in the outer 16 channels before passing them to the central combustion channel. Preheating the combustion inlet enhances the methanol conversion in the combustion volume, thereby helps in minimizing the amount of combustion fuel used to drive the endothermic steam reforming reaction.

4.1.4 Configuration IV

The fourth configuration (shown in Figure 4.1d) was accomplished through sealing the outer 16 channels with the combustion outlet stream, by passing the combustion outlet from the central combustion channel to the outer 16 channels. The methanol combustion process being an exothermic reaction produces enormous heat, in which certain heat was taken away with the combustion outlet gas stream. Utilizing the heat from the combustion outlet stream in the outer 16 channels increases the hotspot temperature of the reactor, which provides sufficient heat to be utilized by the reforming stream at higher flowrates.

4.2 Experimental procedure

The microreactor construction, assembly and operation were the same as discussed in Chapter 3. In this study, the fluid flow through the outer 16 channels was achieved by making inter-fluidic connections between the third-volume of outer 16 channels to the combustion/ reforming volume as per the flow configurations shown in Figure 4.1. Gas leaks were observed on both ends of the distributor, which prevented continuous flow of gases in all three reactor volumes. The initial problem in achieving proper flow in all three reactor volumes was the huge pressure drop created during looping the fluid between the combustion/reforming volume to the outer 16 channels. This was solved and proper sealing of the system was achieved by replacing the silicon gasket in the reforming inlet/combustion outlet with the graphite gasket, which helped to minimize the pressure drop and avoid leaks in the reactor enabling proper flow in all the

channels. Therefore, experiments with all the four configurations were performed with graphite gaskets on both ends of the distributor.

The combustion process yields liquid water as one of its by-products, which led to accumulation of water in the combustion channel due to difficulty in looping the condensed water from the combustion product stream to the outer 16 channels. This eventually resulted in extinction of combustion over time. So, the reactor was tilted in such a direction that facilitates easy flow of liquid product from the combustion channel to the outer 16 channels ensuring continuous operation.

4.3 Results & discussion

The previous experimental study of Architecture C showed promising results by achieving a maximum overall hydrogen yield of about 53% at a combustion flow rate of 300 sccm and a reforming flow rate of 1800 sccm with the hot-spot magnitude of 218^{o}C. Hence, experiments with these four different configurations were performed at a fixed combustion flow rate of 300 sccm corresponding to Re_{comb} = 600, with the reforming flowrates varying from 200 to 2000 sccm, corresponding to Re_{ref} = 50,100,150 to 500 respectively.

The hotspot temperature was increased with these reactor configurations by enhancing the self-insulating nature of the microchannel network with the maximum temperatures >270^{o}C for all four configurations, which is 50^{o}C - 60^{o}C higher than the maximum temperature (240^{o}C) achieved with earlier experiments of Architecture C (discussed in Chapter 3). Figure 4.2 shows that the configurations (II) and (IV) had

increased reactor temperature significantly than configurations (I) and (III) due to increased heat retention in the reactor.

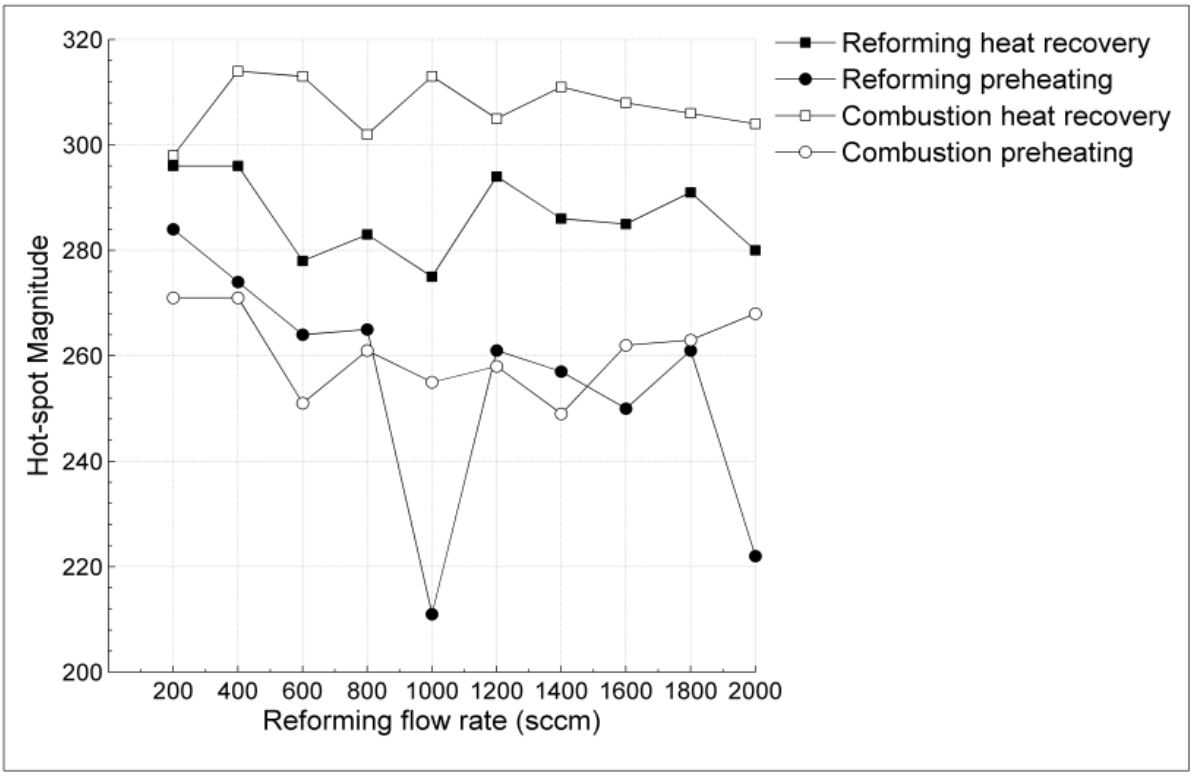

Figure 4.2. Hotspot magnitude in the microchannel network for the four configurations studied using the outer 16 heat retention channels

The methanol conversion in the combustion volume was constant and was unaffected with the variation in reforming flowrate. In the reforming volume, methanol conversion of ~100% was obtained at low reforming flowrates, which decreased gradually due to the decrease in residence times with an increase in reforming flowrate. Figure 4.3 shows the overall methanol conversion obtained with all four configurations.

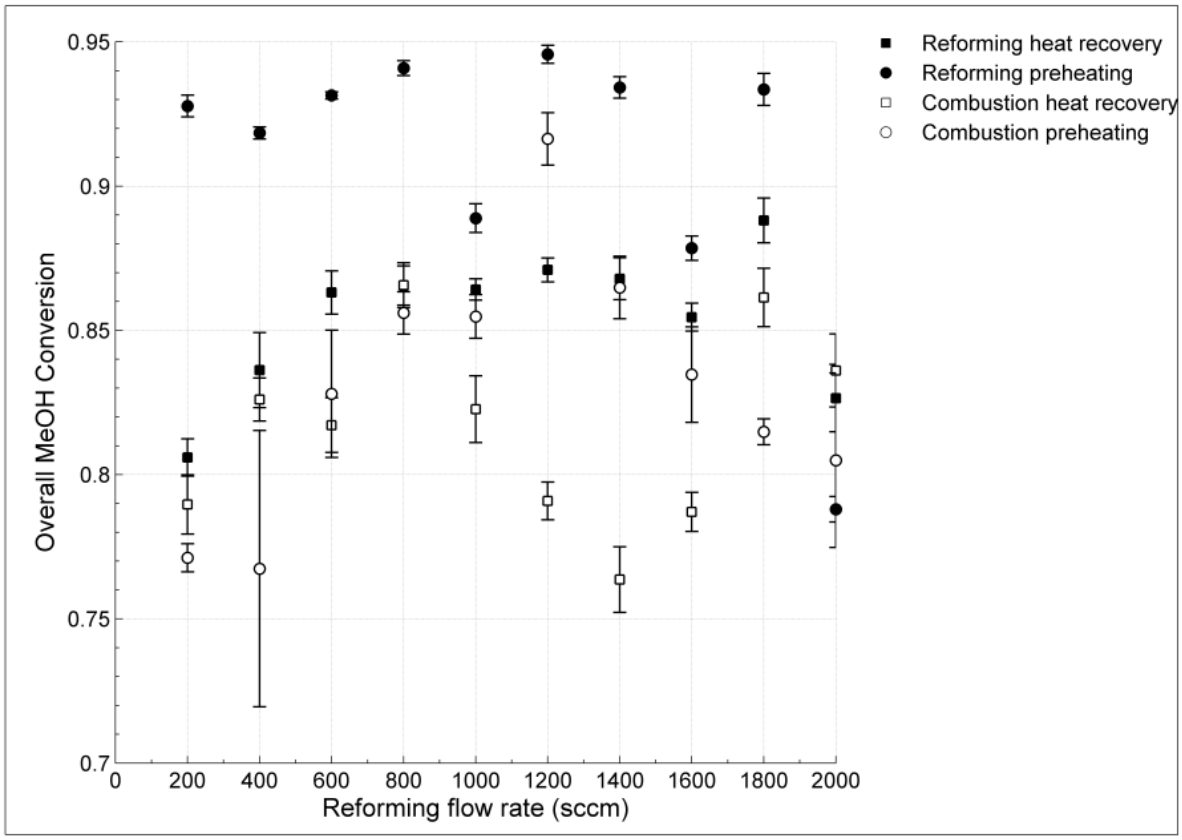

Figure 4.3. Overall methanol conversion in the microchannel network for the four configurations studied using the outer 16 heat retention channels

Measurable amounts of hydrogen yields of <6% were observed in the combustion volume for all four configurations. More than 95% hydrogen yields were obtained from the reforming volume at low reforming flowrates, which decreased with an increase in reforming flowrate due to a decrease in methanol conversion. Overall hydrogen yield (shown in Figure 4.4) signifying the hydrogen produced from the combustion and reforming volumes, increased with an increase in reforming flowrate. Though increase in hotspot temperature favors methanol decomposition, it shifts the

equilibrium of water gas shift reaction towards left. Hence, the increased reactor temperature favored higher CO yields and lowered H_2 yields by shifting to the reverse water-gas shift reaction.

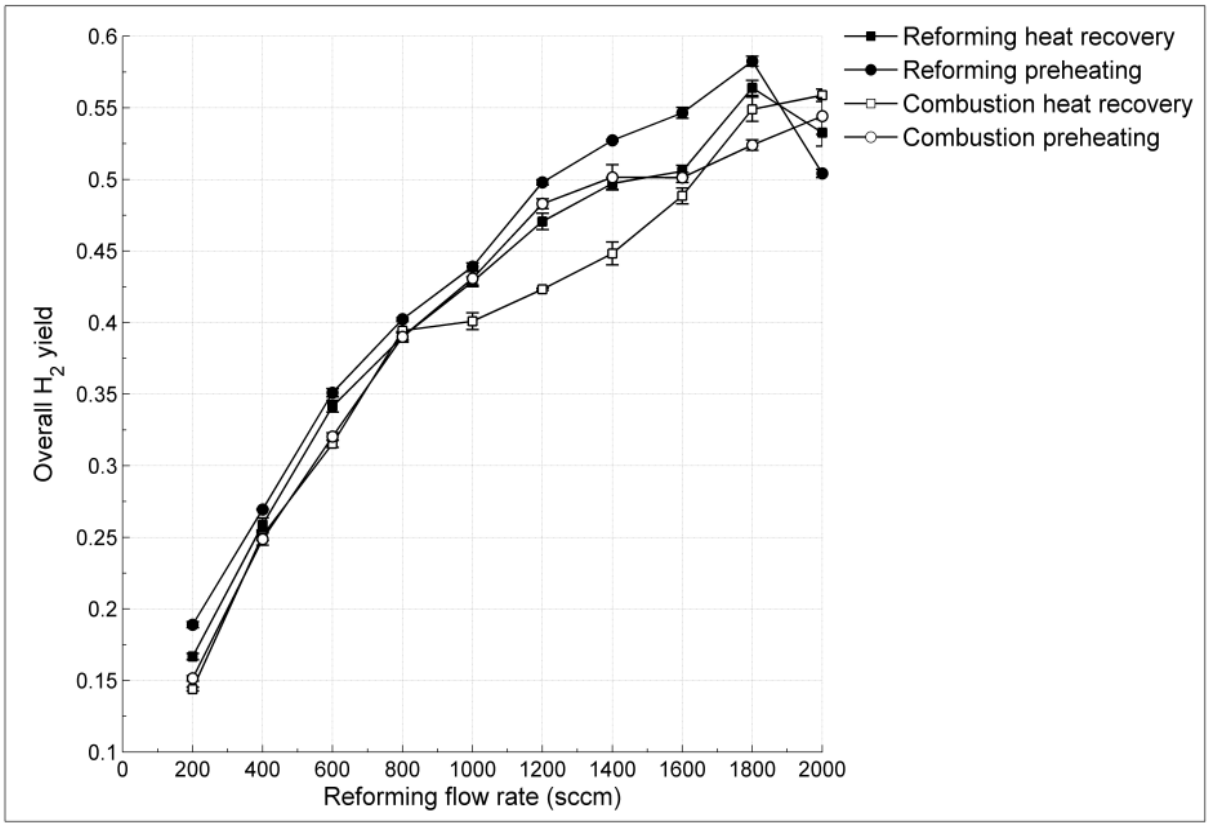

Figure 4.4. Overall hydrogen yield in the microchannel network for the four configurations studied using the outer 16 heat retention channels

Copper based catalysts have a maximum operating temperature of <270^{o}C to achieve higher yields and selectivities for methanol steam reforming reaction. The reforming catalyst ($CuO/ZnO/Al_2O_3$) loses its activity at higher temperatures (i.e. above

300^{o}C) due to thermal sintering. Therefore, methanol steam reforming reaction gives higher hydrogen yields only if it is operated at a temperature range of 220^{o}C - 270^{o}C using copper based catalysts (discussed in Chapter 1). A maximum overall hydrogen yield of about 58% with the hot-spot magnitude of 290^{o}C was obtained from configuration (I) of preheating the reforming stream before passing them to respective eight reforming channels. Thus, utilizing the outer 16 channels for preheating/sealing with input/output stream provided increased overall hydrogen yield when compared to earlier experiments of Architecture C with the maximum overall hydrogen yield of 53% at a hotspot magnitude of 218^{o}C.

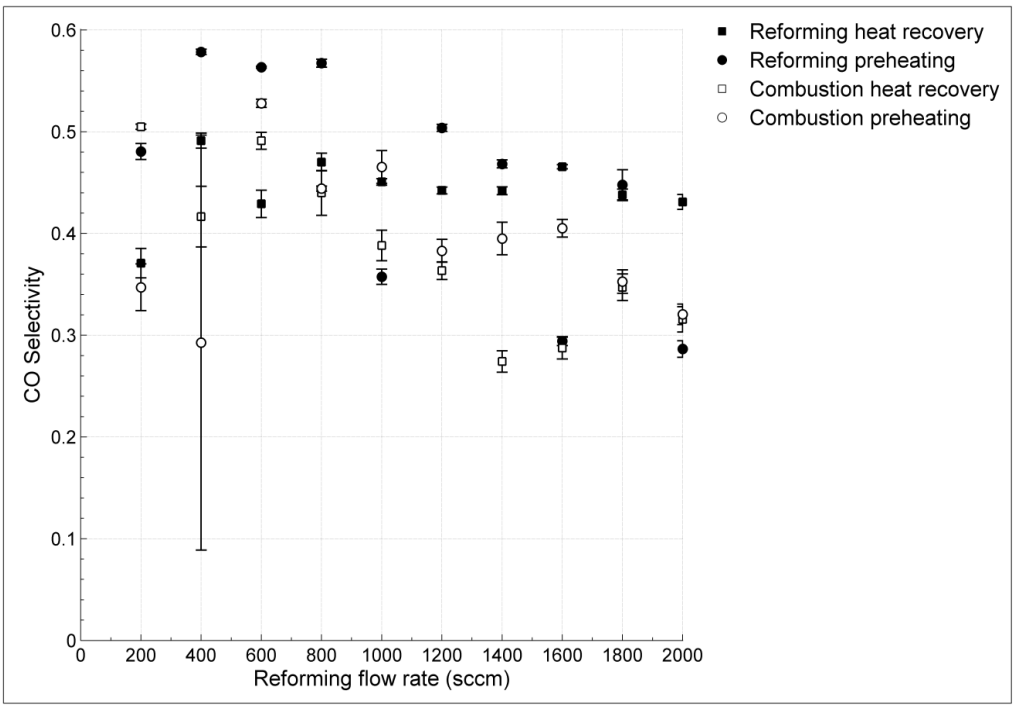

Figure 4.5. CO selectivity in the microchannel network for the four configurations studied using the outer 16 heat retention channels

Carbon monoxide yields were observed in both combustion and reforming volumes. CO selectivities (shown in Figure 4.5) were increased due to increased CO yields in the reforming volume. An increase in reactor temperature shifted the WGS reaction equilibrium towards the reactant side, which favored the formation of CO and lowered H_2 yields.

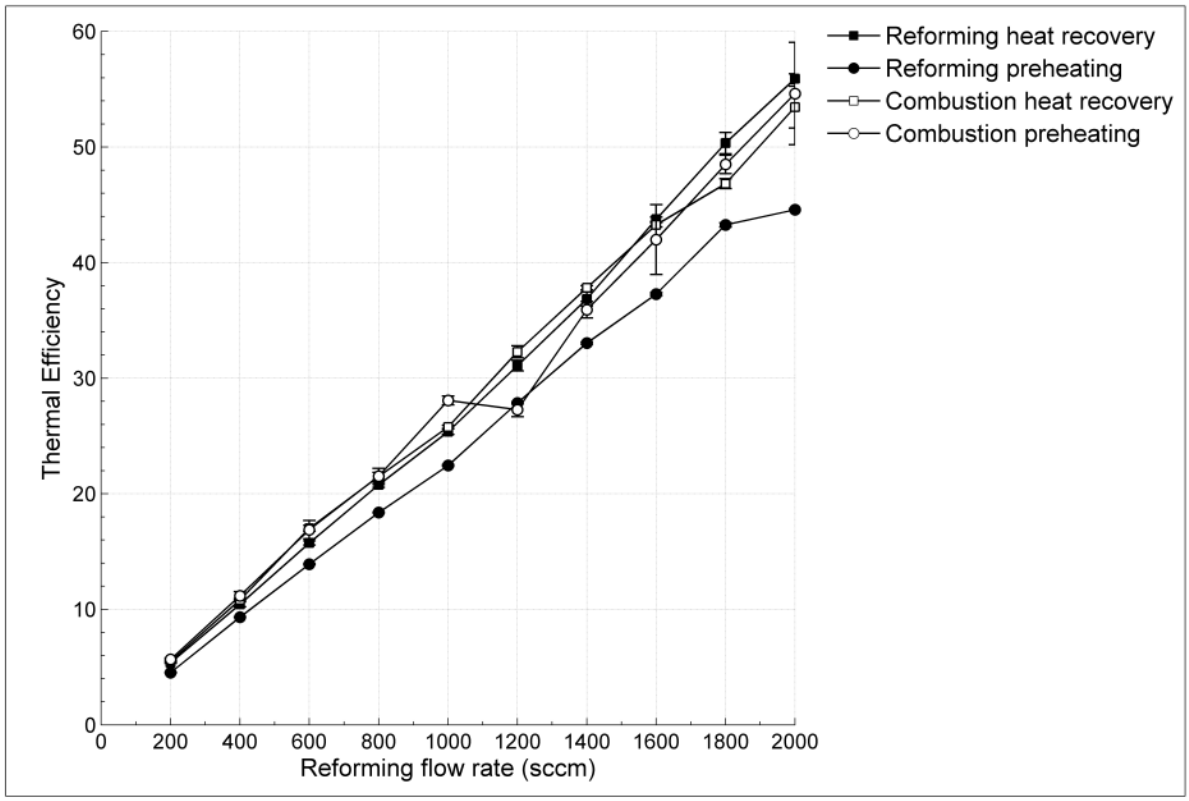

Figure 4.6. Thermal Efficiency of the microchannel network for the four configurations studied using the outer 16 heat retention channels

Thermal efficiency of the system (shown in Figure 4.6) was increased with an increase in reforming flowrates. Earlier experiments with Architecture C provided 51% thermal efficiency at a combustion flowrate of 300 sccm and a reforming flowrate of 1800 sccm, which had increased to 54% with an overall hydrogen yield of ~58% by configuration (I) of preheating the reforming stream in the outer 16 channels.

4.4 Conclusion

The four reactor configurations investigated using the outer 16 channels of Architecture C, by preheating the combustion/reforming input stream and sealing with combustion/reforming output stream, showed $50^{o}C$ – $60^{o}C$ higher hot-spot magnitude than the earlier experiments with Architecture C discussed in Chapter 3. The increase in reactor temperature reduced H_2 yields in the reforming volume due to the combination of reduced catalytic activity at temperatures $>270^{o}C$ and a shift in WGS equilibrium towards left. This showed the effect of hot-spot magnitude in achieving enhanced system performance by maintaining the catalytic activity and favoring WGS reaction. The maximum overall hydrogen yield of 58% was achieved with the combustion flowrate of 300 sccm and reforming flow rate of 1800 sccm by preheating the reforming stream in the outer 16 heat retention channels (i.e. Configuration I). The reactor performance was expected to further increase by maintaining an optimum operating temperature in the reforming volume with a further increase in reforming flowrate or with the reduction of combustion flowrate below 300 sccm. Therefore, these four configurations showed

promising operation for maintaining higher reactor temperature by effective axial and radial insulation than the earlier experimental study.

5. NUMERICAL MODELING OF COUNTER-CURRENT HEAT-EXCHANGER MICROREACTOR USING COMSOL MULTIPHYSICS™ AND INVESTIGATIONS ON THE IMPACT OF SUBSTRATE THERMAL CONDUCTIVITY UPON THE REACTOR PERFORMANCE

A 3-D design simulation of the thermally-integrated heat-exchanger microreactor, coupling exothermic methanol combustion and endothermic methanol steam reforming for portable hydrogen production, was performed using COMSOL Multiphysics 3.5a. Excluding fluid-solid transport properties and with simple kinetics for both combustion and reforming reaction, an initial FEM model of counter-current heat exchanger microreactor was designed to investigate the reactor hotspot shape, location and trends in reactor performance as a function of material selection. Specifically, the effect of solid-phase thermal conductivity was investigated upon the performance of the system by using four different thermal conductivity substrates such as glass, ceramic, stainless steel and silicon.

Numerical modeling of spontaneous combustion gave numerous challenges leading to instabilities at high reaction rates. Establishing control parameters to reduce the complexity of combustion chemistry was arduous, so the combustion reaction rate was limited by identifying the threshold point of stability. With these factors, it was difficult to obtain an exact solution but the current results were encouraging and much useful for future studies on establishing an enhanced design and operation of the

microchannel network, by tuning the solver parameters to control the fluctuations in combustion kinetics at high reaction rates.

5.1 Model definition

The three dimensional 5x5 microchannel reactor (shown in Figure 5.2) was designed using COMSOL 3.5a software with 25 square channels each of width 2.8 mm and length 15 cm. The chemical engineering module was used to define the subdomains for combustion, reforming and reactor substrate. The mass, momentum and energy transport of the three subdomains was defined using Maxwell Stefan diffusion and convection, Darcy's Law and Convection and Conduction application modes respectively. The porous medium was assumed to be isotropic and homogenous. Lastly, steady-state was assumed throughout the model.

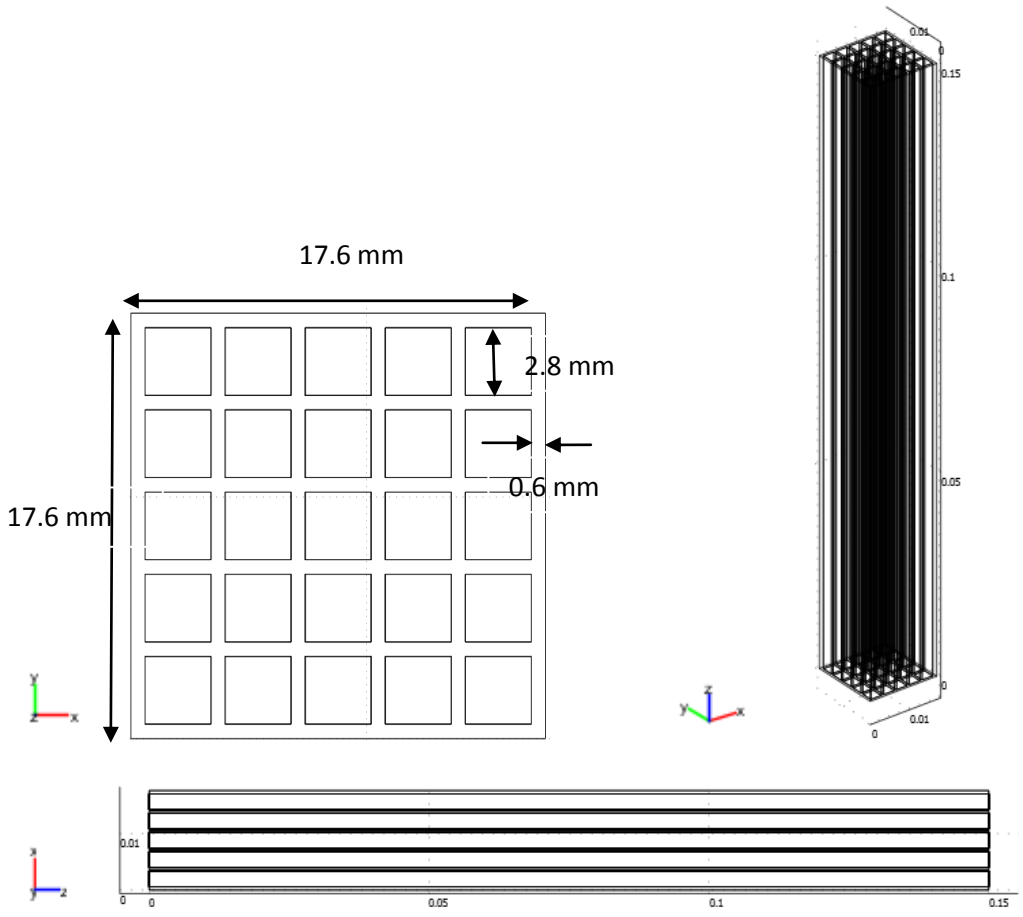

Figure 5.1. A COMSOL 3-D model of 25-channeled counter-current heat-exchanger microreactor

5.1.1 Mass transport – Maxwell-stefan diffusion and convection

The mass transport of the reforming and combustion subdomain was defined using steady-state Maxwell-stefan diffusion and convection equation.

$$\nabla.\left(\left(\rho\omega_i u\right)-\left(\rho\omega_i\sum_{j=1}^{n}D_{ij}\left(\nabla x_j+(x_j-\omega_j)\frac{\nabla P}{P}\right)-D_i^T\frac{\nabla T}{T}\right)\right)=R_i \qquad (5.1)$$

Effective diffusivity (D_{eff}) of the multicomponent mixture within the catalyst pellet includes ordinary diffusion (D_m) and Knudsen diffusion (D_k) [74]

$$\frac{1}{D_{i,eff}} = \frac{\tau}{\varepsilon}\left(\frac{1}{D_{i,m}} + \frac{1}{D_{i,K}}\right) \tag{5.2}$$

Knudsen diffusion was calculated by

$$D_{i,K} = \frac{2}{3} r_{pore}\sqrt{\frac{8RT}{\pi M_i}} \tag{5.3}$$

Molecular diffusion coefficient was obtained using the equation

$$D_{i,m} = \frac{1 - x_i}{\sum_{j=1}^{n}(x_j / D_{ij})} \quad \text{where, } D_{ij} = 1.00\times10^{-7} \frac{T^{1.75}\sqrt{\left(\frac{1}{M_i} + \frac{1}{M_j}\right)}}{P\left[(\sum \upsilon_i)^{\frac{1}{3}} + (\sum \upsilon_j)^{\frac{1}{3}}\right]^2} \tag{5.4}$$

Atomic diffusion volumes (υ) of C (16.5), H (1.98), O (5.48), H_2 (7.07), N_2 (17.9) and O_2 (16.6) were used to estimate the molecular structural diffusion volume *(Σ υ)* for each component using their chemical formula [75]. Mass generation term for each component was defined using their kinetics and stoichiometric relation.

5.1.1.1 Kinetics of methanol steam reforming

Methanol steam reforming (Eqn 5.5) network involves two reactions: methanol decomposition (Eqn 5.5a) followed by water-gas shift reaction (Eqn 5.5b)

$$CH_3OH \Rightarrow CO + 2H_{2,} \qquad \Delta H_{rxn} = 92 \text{ kJ/mol} \tag{5.5a}$$

$$CO + H_2O \Leftrightarrow CO_2 + H_{2,} \qquad \Delta H_{rxn} = -41.1 \text{ kJ/mol} \tag{5.5b}$$

$$CH_3OH + H_2O \Rightarrow CO_2 + 3H_2, \quad \Delta H_{rxn} = 49.4 \text{ kJ/mol} \tag{5.5}$$

Suh, Lee *et al*. [76] showed that the overall MSR network over BASF F3-01 ($CuO/ZnO/Al_2O_3$) catalyst could be accurately modeled using a corrected version of the kinetics developed by Amphlett. Amphlett kinetics [76] provided the reaction rates for methanol steam reforming reaction over a low temperature shift catalyst C18HC with the operating parameters of temperature ranging from 200 - 300^oC, pressures 1 - 3 atm and steam to methanol ratio of 0.67 - 1.5. The semi-empirical model proposed by Amphlett for catalytic methanol steam reforming used two reactions, the overall steam reforming and methanol pyrolysis. In the range of operating conditions with steam to methanol ratio of 0.67 - 1.5, the water-gas shift reaction was neglected without any significant loss in accuracy as per Amphlett chemical kinetics [76].

As a modification to Amphlett original kinetics due to the difference in the activity and selectivity of BASF F3-01 catalyst and C18HC catalyst , Suh, Lee *et al*. [76] introduced correction factors for reforming and decomposition reactions as 5.5 and 3.5 respectively, which are determined empirically from the experimental data [76]. With the similar composition of $CuO/ZnO/Al_2O_3$ (40% CuO/ 40% ZnO/ 20% Al_2O_3) for BASF F3-01 and our catalyst BASF R3-15, the same correction factors were used for methanol steam reforming reaction kinetics.

Considering the reaction taking place in a packed-bed plug flow reactor, the reaction rates were expressed as

$$R_D = (1-\varepsilon)\rho_s k_D \tag{5.6}$$

$$R_R = (1-\varepsilon)\rho_s k_R C_{MeOH} \tag{5.7}$$

Where catalyst density was estimated using (Eqn 5.8)

$$\rho_s = \frac{m_{cat}}{V_{cat}} \tag{5.8}$$

The rate constants of reforming (k_R) and decomposition reaction (k_D) were defined using Arrhenius equation (Eqn 5.9)

$$k_i = A_i e^{(-E_i/RT)} \tag{5.9}$$

$$k_R = C_R(A_R + B_R \ln(SMR)) \exp(-\frac{E_R}{RT}) \tag{5.10}$$

$$k_D = C_D A_D \exp\left(-\frac{E_D}{RT}\right) \tag{5.11}$$

$$A_R = 1.15\text{x}10^6 (m^3 s^{-1} kg^{-1})$$

$$B_R = 9.41\text{x}10^5 (m^3 s^{-1} kg^{-1})$$

$$E_R = 84{,}100 \ (Jmol^{-1})$$

$$A_D = 7.09\text{x}10^7 (mol \ s^{-1} kg^{-1})$$

$$E_D = 111{,}200 \ (Jmol^{-1})$$

The rates of generation of reaction species were expressed as

$$r_{MeOH} = -R_R - R_D \tag{5.12}$$

$$r_{H_2O} = -R_R \tag{5.13}$$

$$r_{CO_2} = R_R \tag{5.14}$$

$$r_{CO} = R_D \tag{5.15}$$

$$r_{H_2} = 3R_R + 2R_D \tag{5.16}$$

5.1.1.2 Kinetics of methanol combustion

Methanol combustion over Pt/Al_2O_3 catalyst is carried out in the central channel to provide heat for driving the endothermic reaction.

$$CH_3OH + 1.5O_2 \Rightarrow CO_2 + 2H_2O \qquad \Delta H_{rxn} = -673.2 \text{ kJ/mol} \tag{5.17}$$

Exact methanol combustion kinetics was difficult to obtain from the literature as it includes numerous elementary equations. For the sake of computational simplicity, the kinetics of catalytic oxidation of methanol was defined by a general power-law rate expression:

$$R_C = k_C P_{MeOH}^{\ m} P_{O2}^{\ n} \tag{5.18}$$

Where, values of m and n were taken to be 1 and 0 for all T > 405 K, based upon Gentry *et al*. kinetics of methanol oxidation over platinum wire catalysts [77].

The rate constant k_C was calculated using Arrhenius law with the frequency factor of A = 8.35×10^9 and activation energy of E = 56.9 kJ/mol, from Schwartz *et al*., 1970 [78]

$$k_i = A_i e^{(-E_i / RT)} \tag{5.19}$$

Each species reaction rates were defined as

$$r_{MeOH} = -R_C \tag{5.20}$$

$$r_{O2} = -1.5 * R_C \tag{5.21}$$

$$r_{CO2} = R_C \tag{5.22}$$

$$r_{H2O} = 2R_C \tag{5.23}$$

The total oxidation of methanol was highly exothermic, introduces instabilities to the system of finite element equations at high reaction rates. To address this convergence challenge, a maximum stable rate for combustion was employed, corresponding to the initial rate of reaction at 400 K. This ensured stable convergence of the mass, momentum and heat equations.

5.1.2 Momentum transport - Darcy's law

The flow of reaction species through the porous media were defined using Darcy's law

$$\nabla.\left(\rho\left(-\frac{k}{\eta}\nabla p_{ref}\right)\right) = 0 \tag{5.24}$$

The inlet and outlet boundary conditions were inlet velocities of each reaction streams and atmospheric pressure respectively.

5.1.3 Energy transport - Convection and conduction

Heat transport of the system was defined by convection and conduction application mode for three subdomains: reforming, combustion and ceramic substrate.

$$\nabla.(-k\nabla T) = Q - (\rho C_p.u.\nabla T) \tag{5.25}$$

The energy source terms for exothermic and endothermic reactions were:

$$Q_{\mathrm{Re}f} = -(\Delta H_R R_R) - (\Delta H_D R_D) \tag{5.26}$$

$$Q_{Comb} = -(\Delta H_C R_C) \tag{5.27}$$

The boundary conditions include heat exchange between reforming/combustion gas stream and the solid substrate, which was defined by

$$q = h_{fs}(T_f - T_s) \tag{5.28}$$

Heat flux from the solid substrate to the ambient was defined as:

$$q = h_s(T_s - T_a) \tag{5.29}$$

Interphase heat transfer coefficient was obtained from Dixon's theoretical predictions of effective heat transfer parameters in packed beds [74]; the fluid-wall heat transfer coefficient for the Reynold's number between 40 – 2000 was defined by

$$Nu_{fw} = \frac{h_{fs} d_p}{k_g} = (0.2)\mathrm{Pr}^{\frac{1}{3}}\,\mathrm{Re}^{0.8} \tag{5.30}$$

where, Re is the Reynold's number and was defined by

$$\mathrm{Re} = \left(\frac{\rho u}{\mu}\right)_i d_p \tag{5.31}$$

Prandtl number (Pr) was defined by

$$\mathrm{Pr} = \frac{C_p \mu}{k} \tag{5.32}$$

The heat transfer coefficient of the surface of non-uniform temperature subjected to natural convection cooling was obtained from Kos *et al*., 1994 [79]

$$h_s = \alpha_0 \left(\frac{T_s - T_a}{L}\right)^{\frac{1}{4}} \tag{5.33}$$

where, α_0 value was defined in the range of 1.5 - 2 W $m^{-7/4}$ $K^{-5/4}$.

Properties such as density, viscosity and thermal conductivity were calculated by assuming an ideal gas mixture

$$\rho = \frac{p}{RT} M = \frac{p}{RT} \sum_{i}^{n} x_i M_i \tag{5.34}$$

Specific heat of the gas mixture was calculated from the mass-weighted average of specific heat of species

$$C_{p,g} = \sum_{i}^{n} m_i C_{p,i} \tag{5.35}$$

Thermal Conductivity and molecular viscosity of the gas mixture were calculated using Wilke's mixture rule [80]:

$$\mu_g = \sum_{i=1}^{n} \frac{x_i \mu_i}{\sum_{j=1}^{n} x_j X_{ij}}$$

$$X_{ij} = \frac{\left[1 + \left(\frac{\mu_i}{\mu_j} \right)^{\frac{1}{2}} \left(\frac{M_j}{M_i} \right)^{\frac{1}{4}} \right]^2}{\sqrt{8} \left[1 + \left(\frac{M_i}{M_j} \right) \right]^{\frac{1}{2}}} \tag{5.36}$$

5.2 Meshing and solver parameters

Free and swept meshing was used to generate mesh for the heat-integrated microchannel network. To decrease the degrees of freedom, swept meshing (shown in Figure 5.3) of normal mesh-size was chosen to create mesh for the microreactor with 3

element layers for reforming/solid substrate sub-domain and 10 element layers for combustion sub-domain. The number of degrees of freedom used to solve the model was 20783 with the solving time of ~2500-3000 seconds. Stationary and segregated Direct (UMFPACK) solver was used with the relative tolerance of 1.0E-3 and maximum number of iterations = 250 for all subdomains.

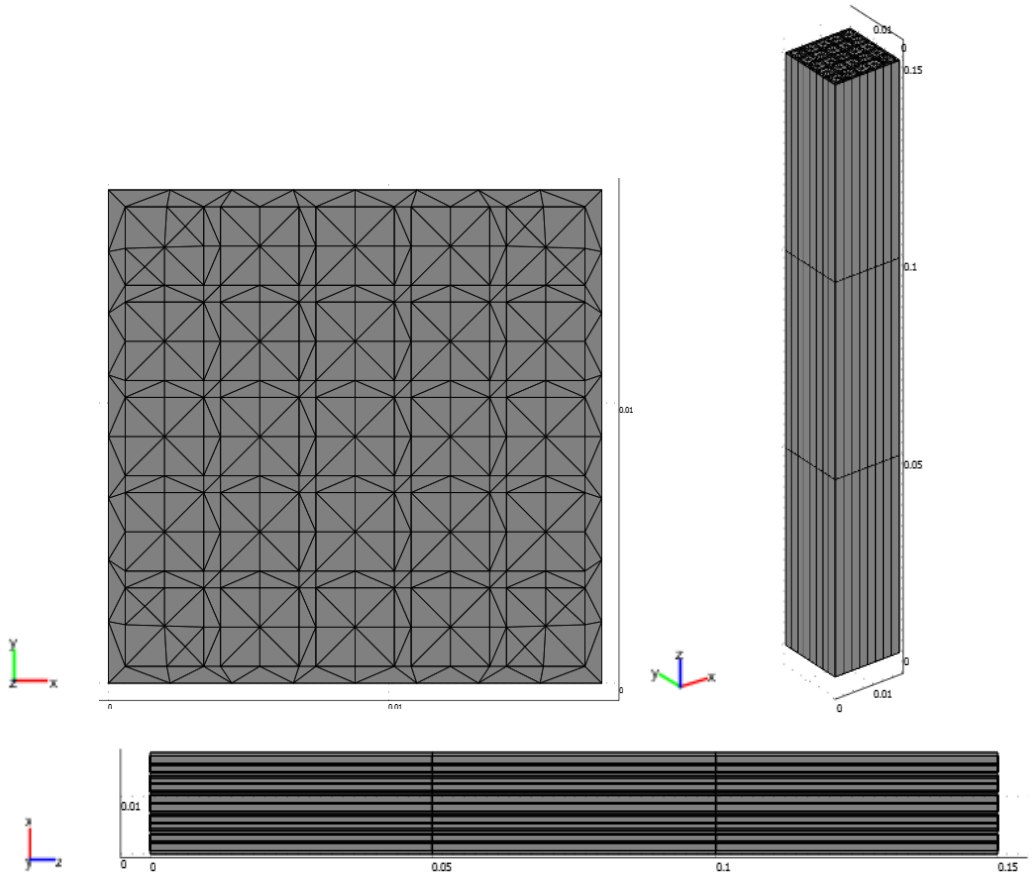

Figure 5.2. A COMSOL 3-D model of a counter-current heat-exchanger microreactor with swept meshing of normal mesh size (3 element layers for substrate and reforming subdomain and 10 element layers for combustion subdomain)

5.3 Results & discussion

Using COMSOL 3.5a, a 25-channeled microreactor of Architecture C was designed with a central combustion channel surrounding eight steam reforming channels and the outer 16 heat retention channels. The central combustion channel provided sufficient heat to drive the endothermic reaction in surrounding 8 steam reforming channels. The thermal coupling was achieved by effective radial heat transfer from the exothermic combustion volume to the endothermic steam reforming volume. Both the combustion and reforming catalytic zone was defined at the axial mid-point of each reaction volume at a length of 3.3 cm and 6 cm respectively. The modeling studies on the performance of heat-integrated microchannel network were done with the combustion and reforming reaction proceeding in counter-current heat-exchanger configuration at a combustion flowrate of 300 cm^3/min and reforming flowrate of 1800 cm^3/min.

The goal of this study was to simulate the heat-integrated ceramic microreactor using the operating parameters discussed in Chapter 3 and also to investigate the influence of substrate thermal conductivity upon the performance of thermally-coupled heat-exchanger microreactor. Thus, to identify the optimum thermal conductivity material for the construction of microchannel reactor, four different thermal conductivity materials were studied; Glass (K = 1.2 W/mK), Ceramic (K = 3 W/mK), Stainless steel (K = 16.2 W/mK) and Silicon (K = 150W/mK). An increase in wall thermal conductivity provided efficient heat transfer within the system but at the same time, led to rapid heat losses to surroundings through axial (conductive) and radial (convective) heat loss

pathways, which resulted in poor heat retention in the system. Figures 5.4, 5.8, 5.12, 5.15 show the axial temperature profiles of the counter-current heat exchanger microreactor for four different materials with the substrate thermal conductivity as the varying factor.

The high thermal conductivity materials such as silicon and stainless steel showed the leveling of reactor temperature along the axial direction due to excessive axial heat conduction losses. This “near-isothermal design” offset the thermal gradient within the system, which in turn affects the self-insulating nature and heat efficiency of the microreactors. A decrease in thermal conductivity of the wall showed enhanced heat transfer efficiency accomplished by maintaining large thermal gradients in the reactor, which acts as a driving force for effective radial heat transfer by limiting axial conduction heat losses via packaging [54]. Therefore, the axial heat conduction has significant effects on heat transfer efficiency of the micro-heat exchangers. Figures 5.5 and 5.9 shows that low thermal conductivity materials like glass, ceramics have the capability of placing the symmetrical hotspot near to the axial midpoint of the reactor. Figure 5.18 shows the surface (wall) temperature profile along the length of the reactor for four different thermal conductivity materials.

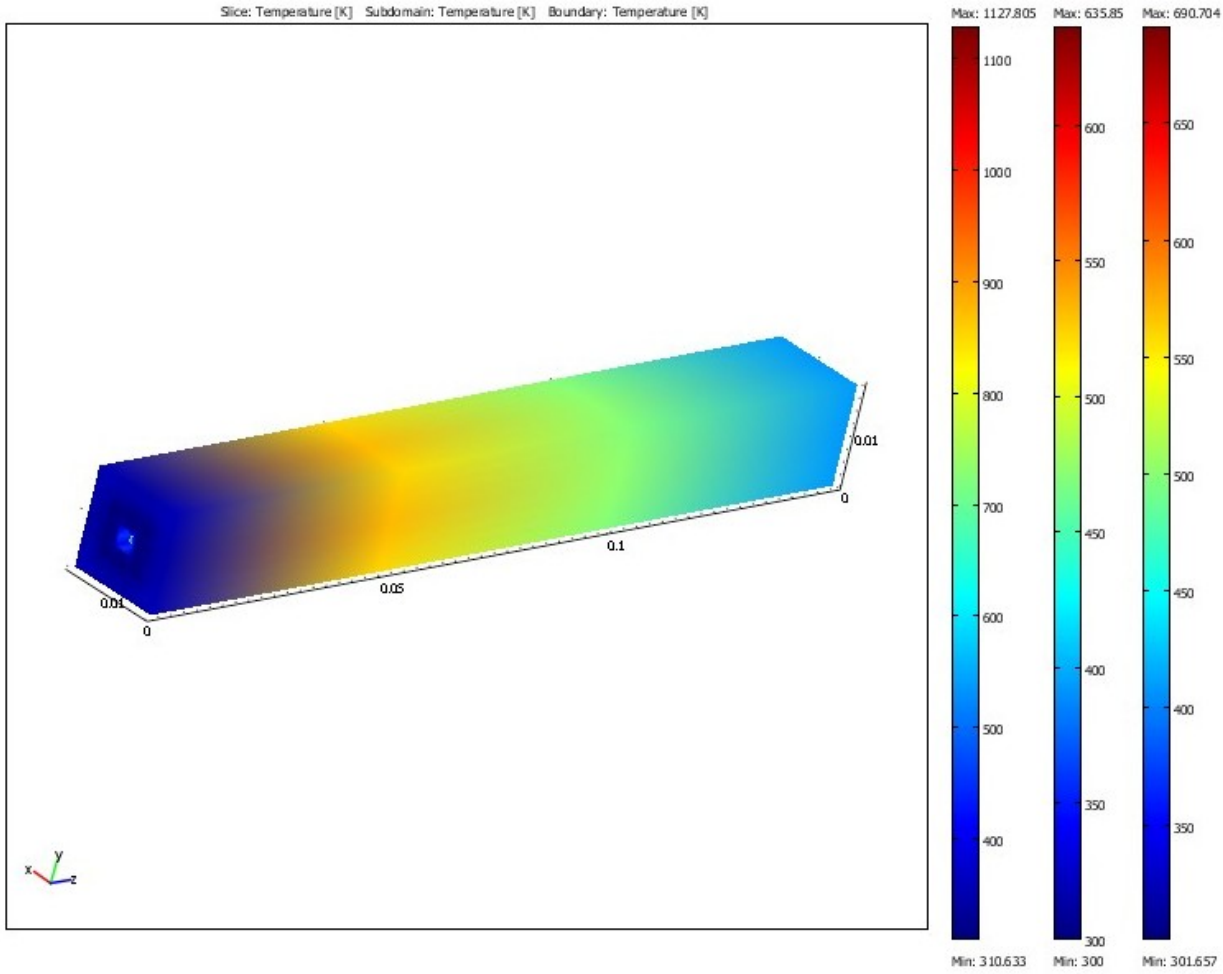

Figure 5.3. Axial temperature profile of counter-current heat-exchanger microscale reactor constructed with glass substrate of thermal conductivity K = 1.2 W/mK

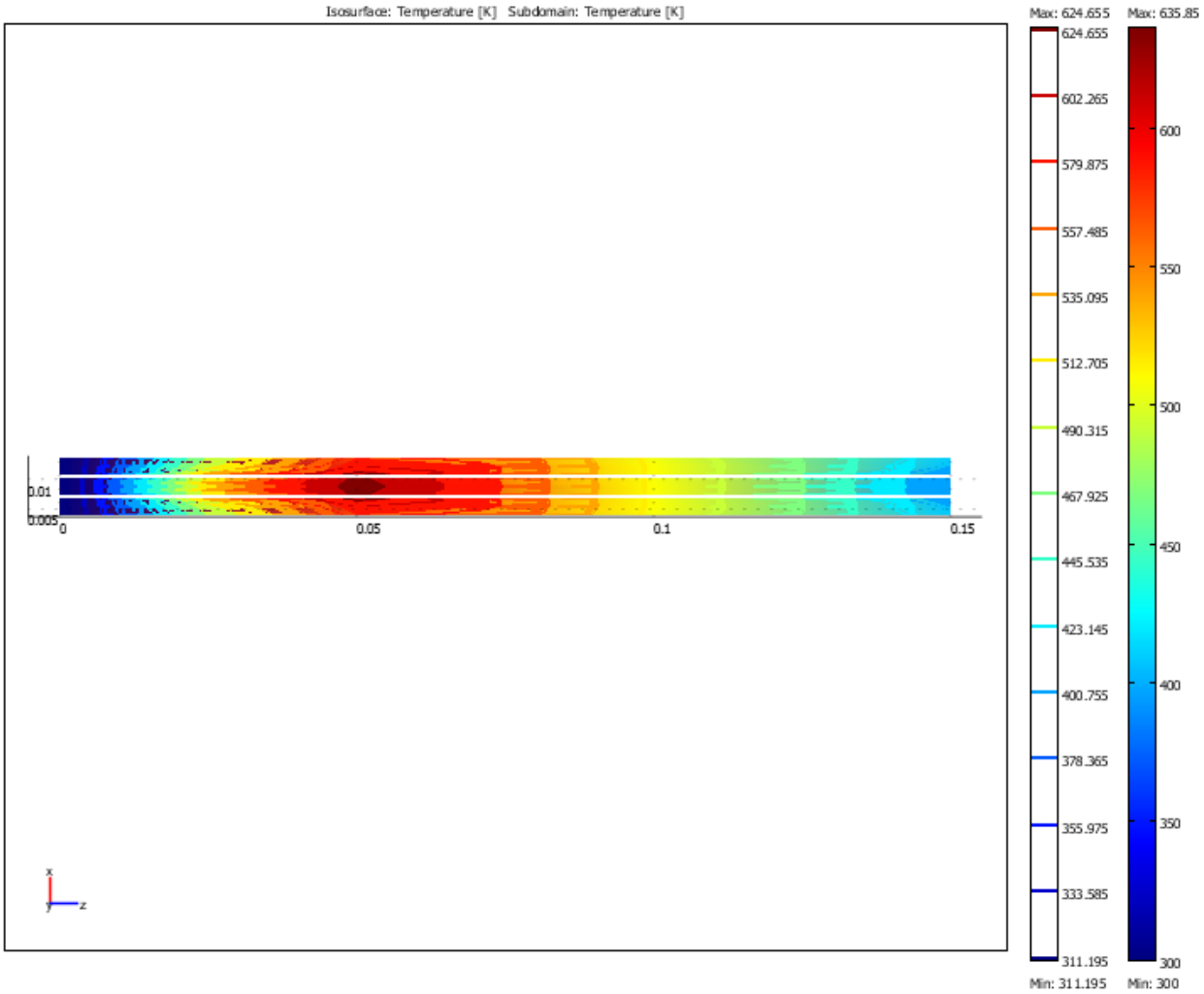

Figure 5.4. Hotspot located near to the axial mid-point of the microreactor constructed with glass substrate

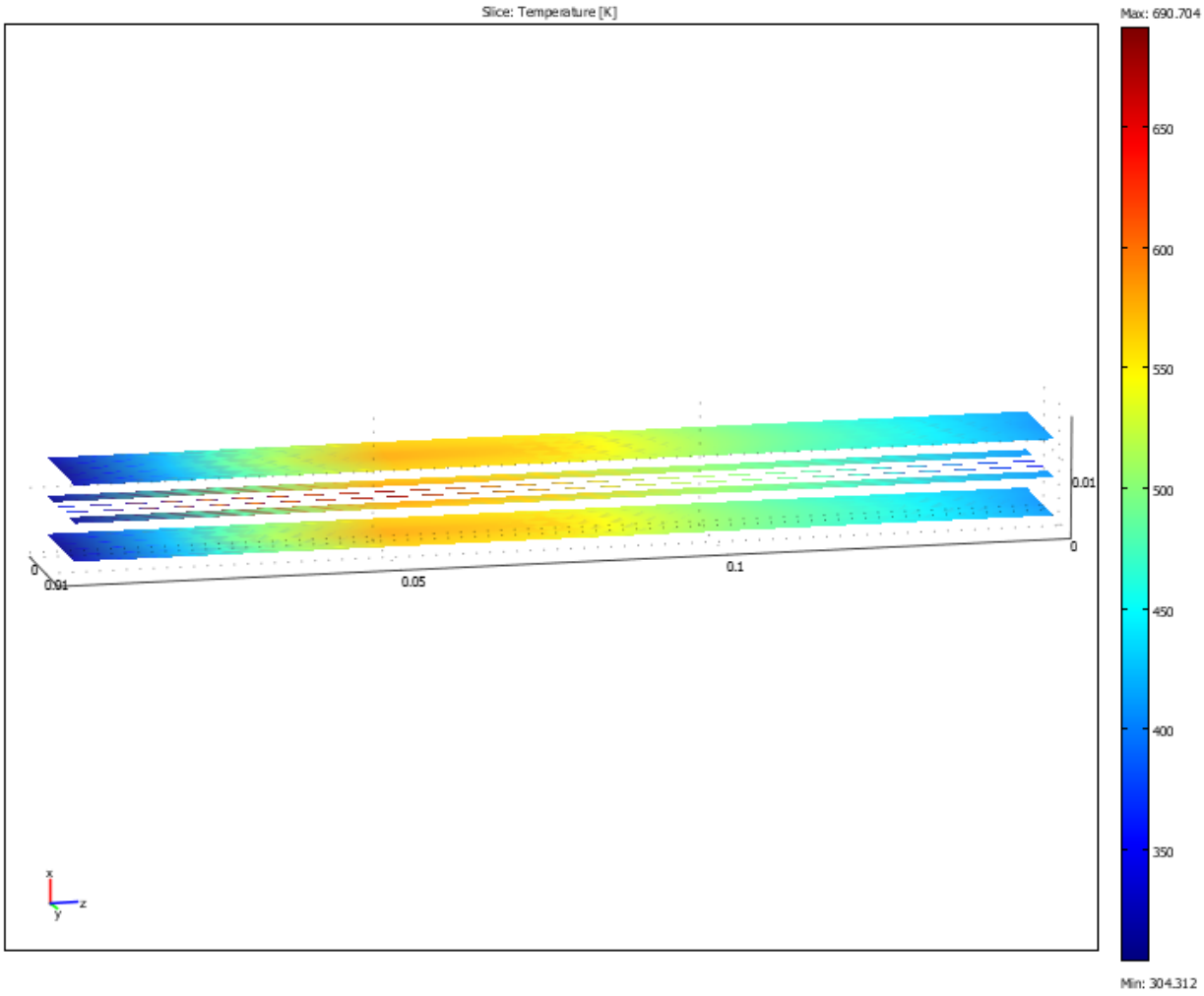

Figure 5.5. Slice plot along the x-direction showing axial and radial temperature profile of the microreactor constructed with glass substrate

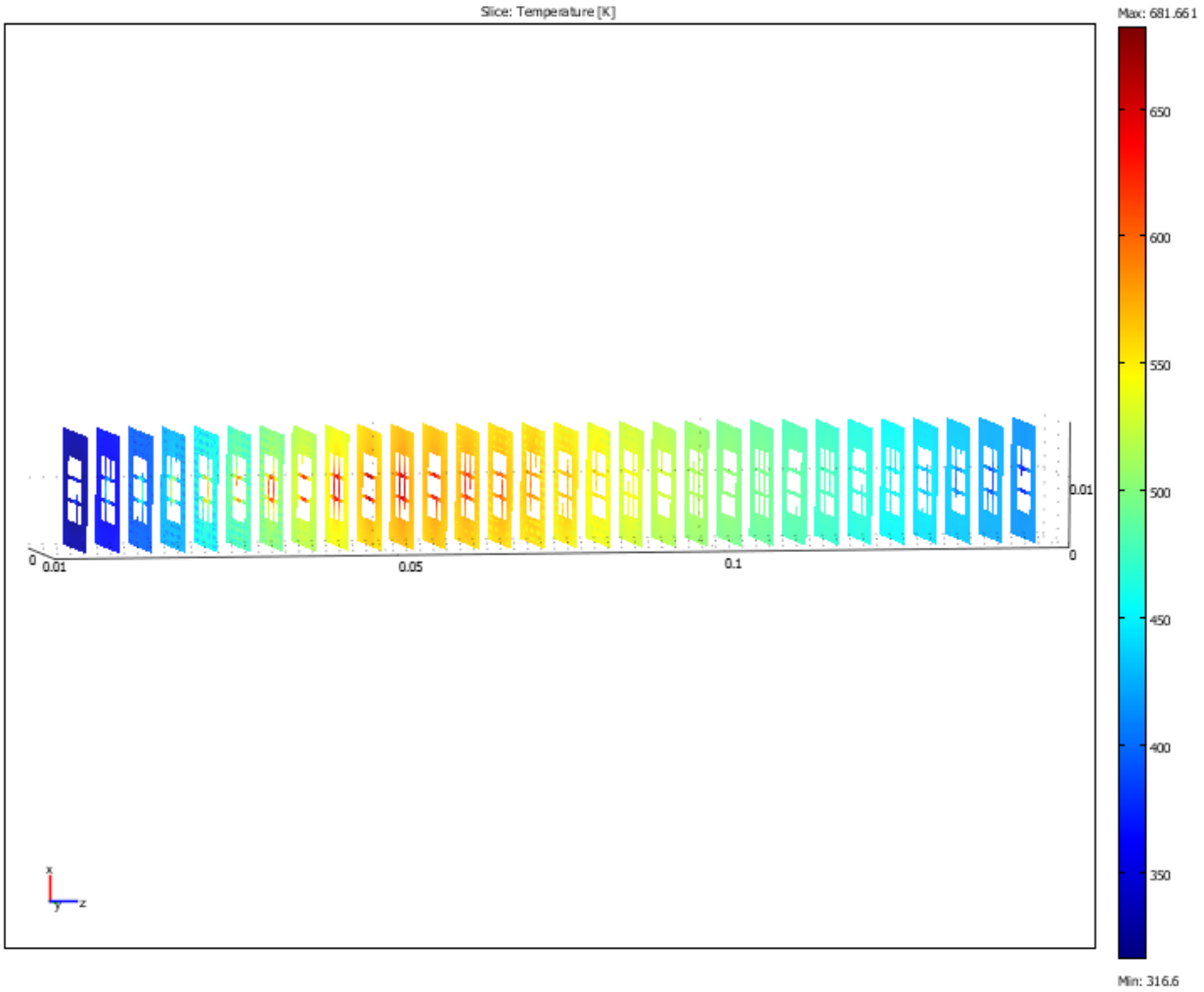

Figure 5.6. Slice plot along the z-direction showing axial and radial temperature profile of the microreactor constructed with glass substrate

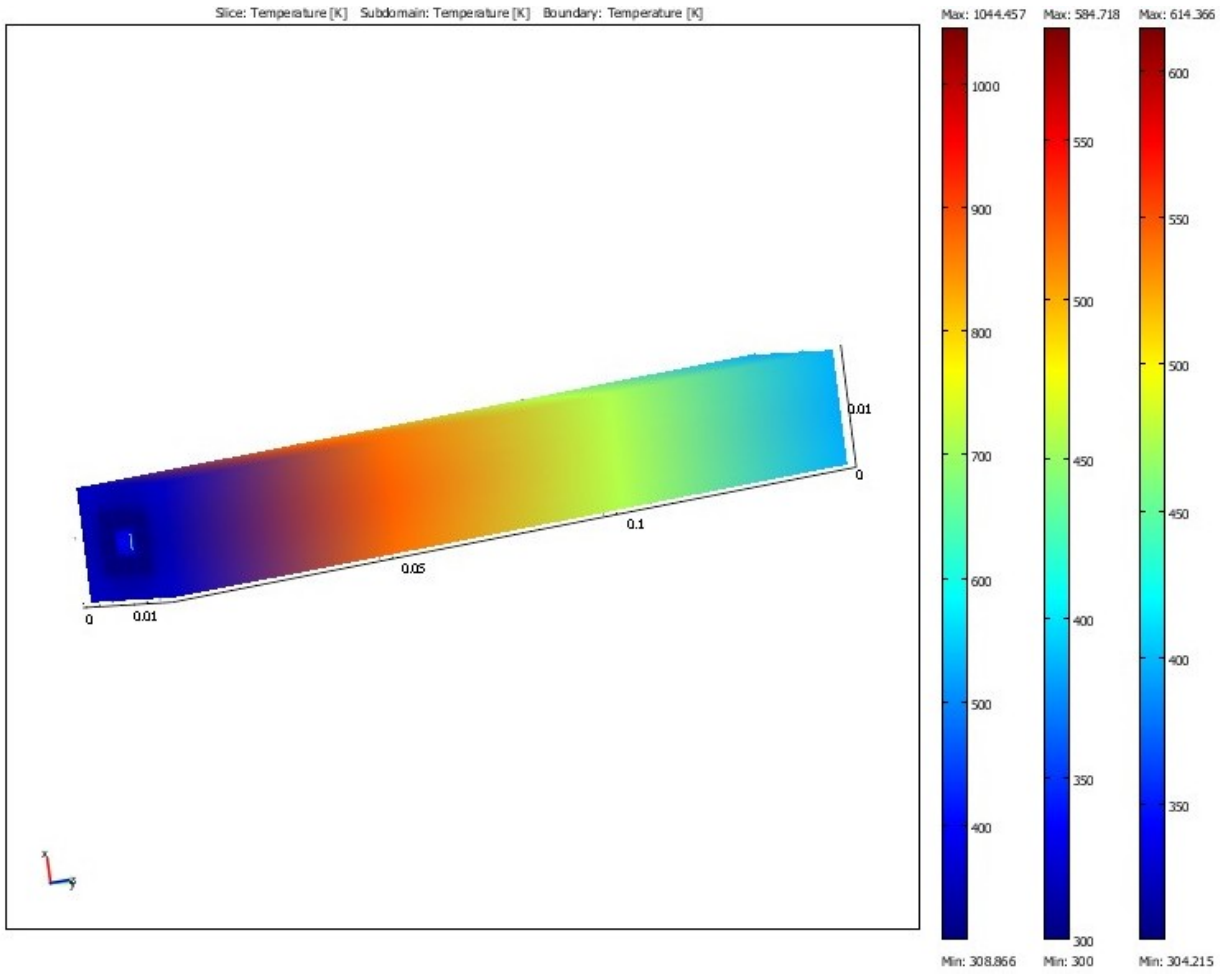

Figure 5.7. Axial temperature profile of counter-current heat-exchanger microscale reactor constructed with ceramic substrate of thermal conductivity K = 3 W/mK

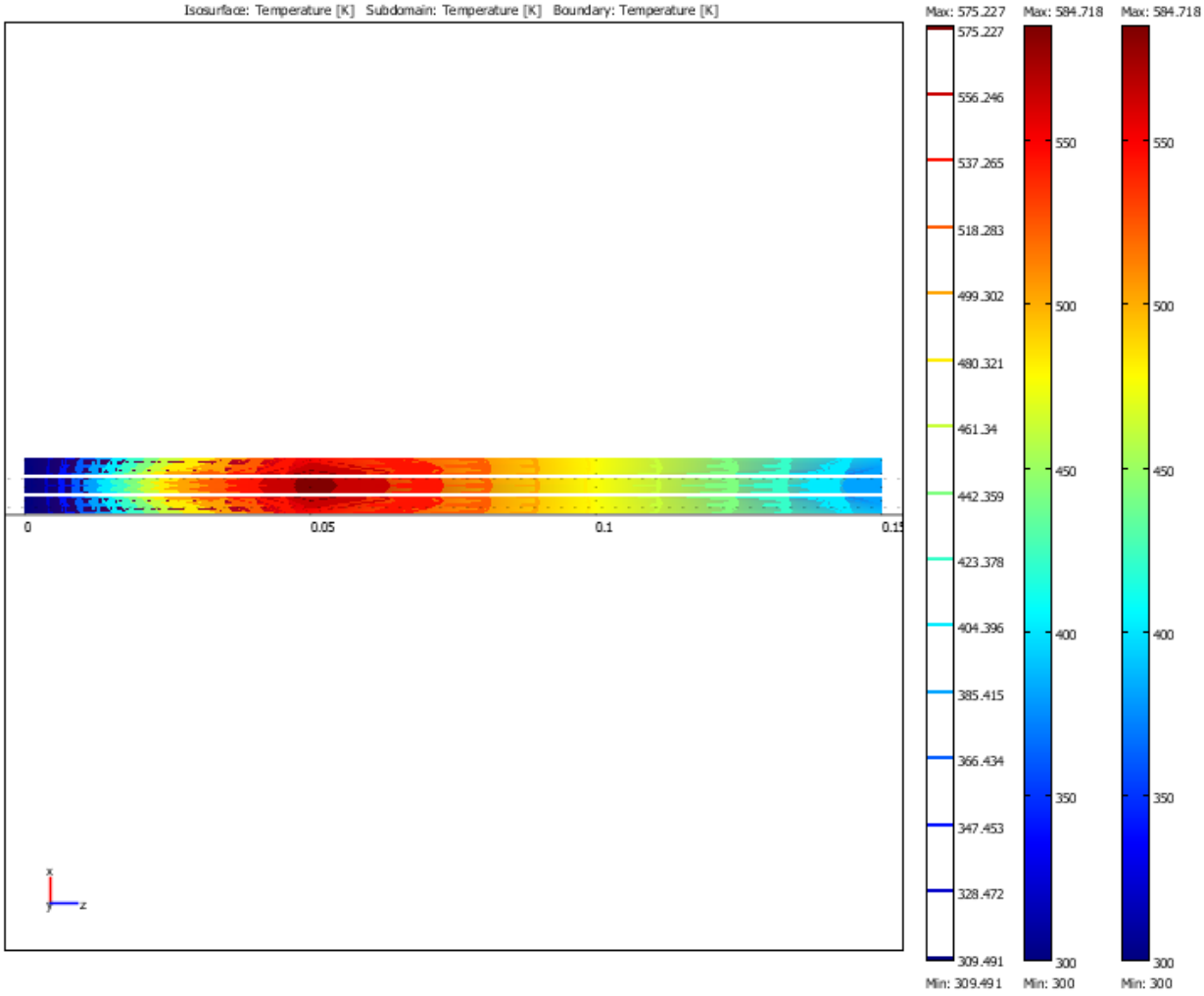

Figure 5.8. Hotspot located near to the axial mid-point of the microreactor constructed with ceramic substrate

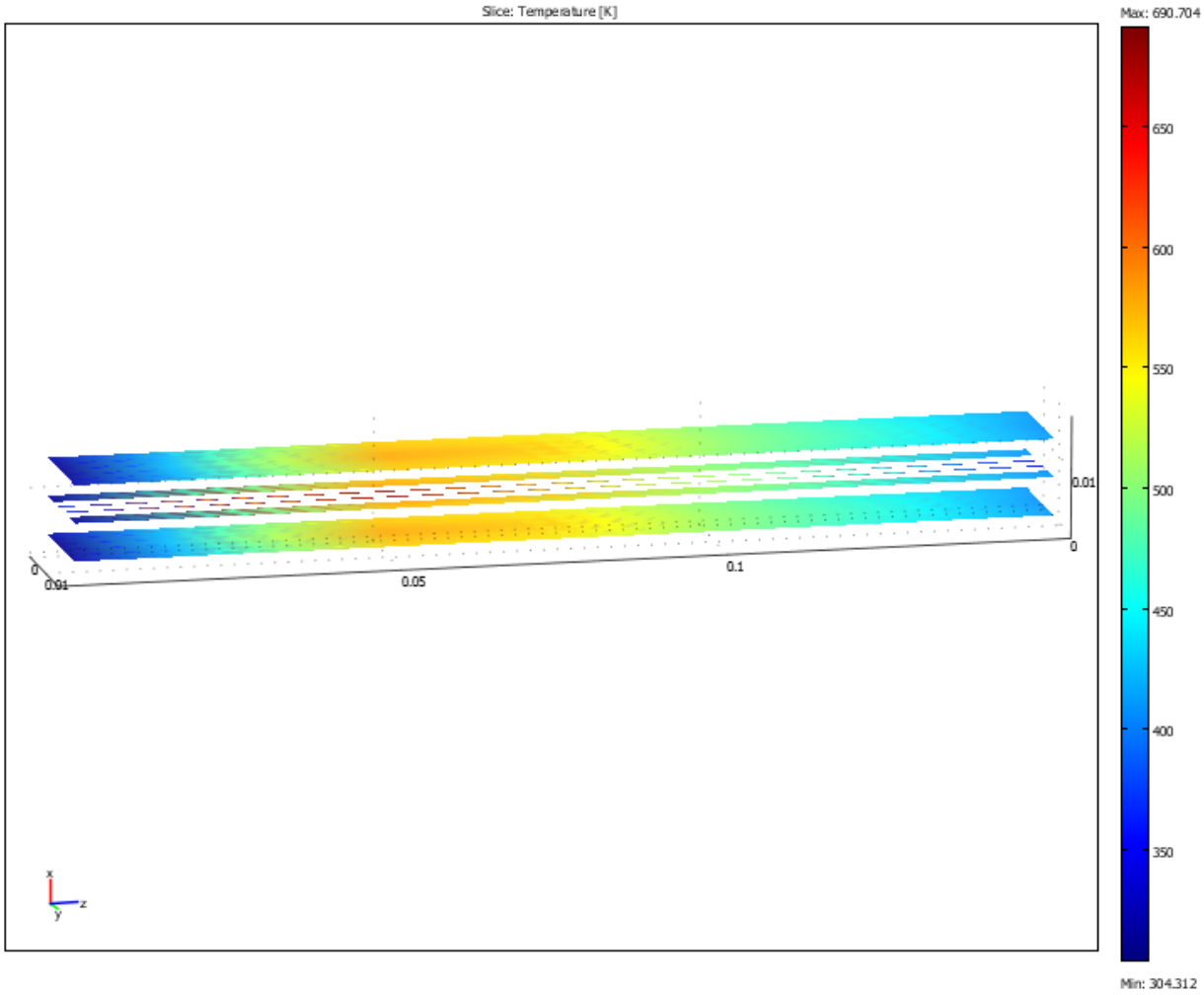

Figure 5.9. Slice plot along the x-direction showing axial and radial temperature profile of the microreactor constructed with ceramic substrate

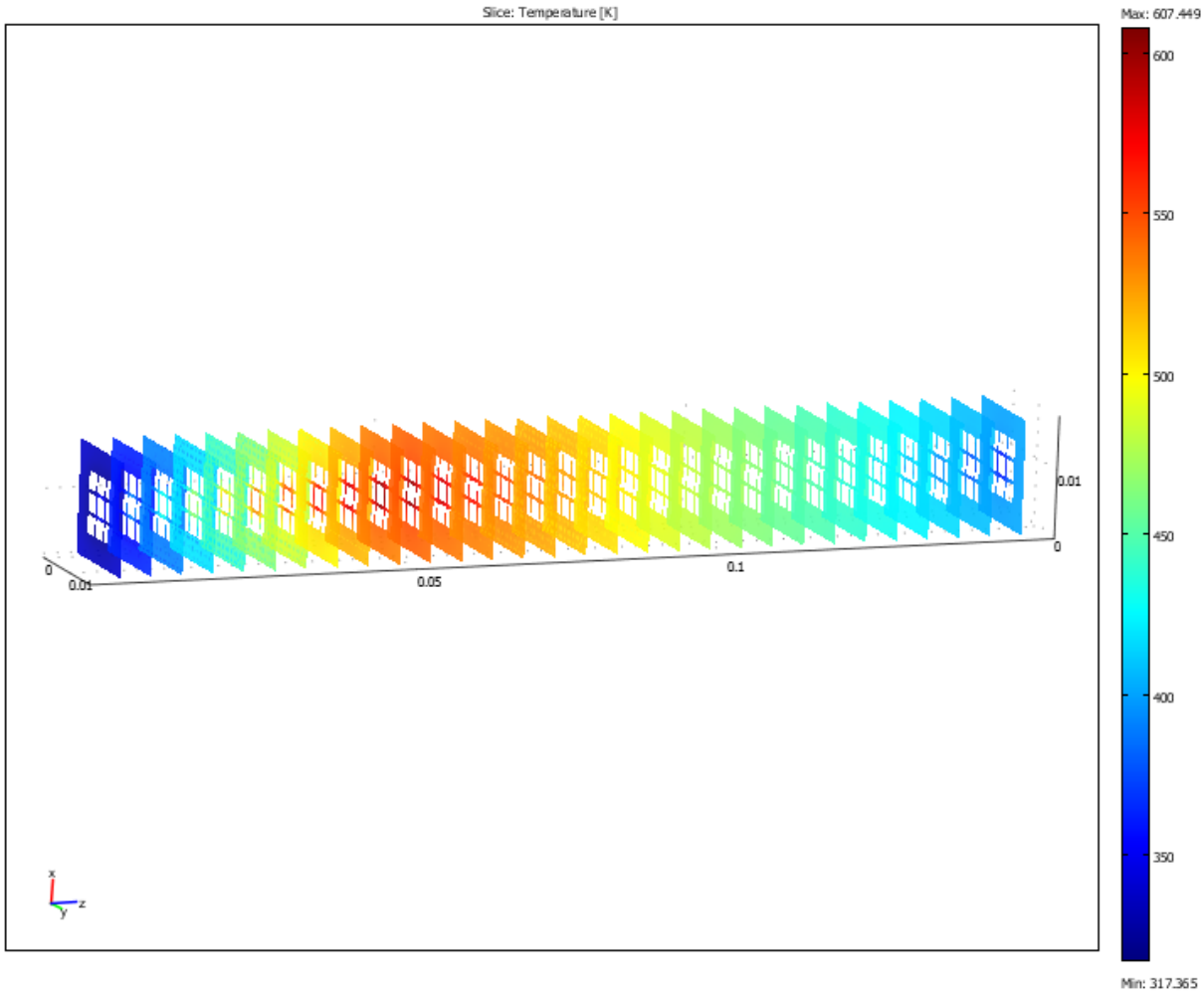

Figure 5.10. Slice plot along the z-direction showing axial and radial temperature profile of the microreactor constructed with ceramic substrate

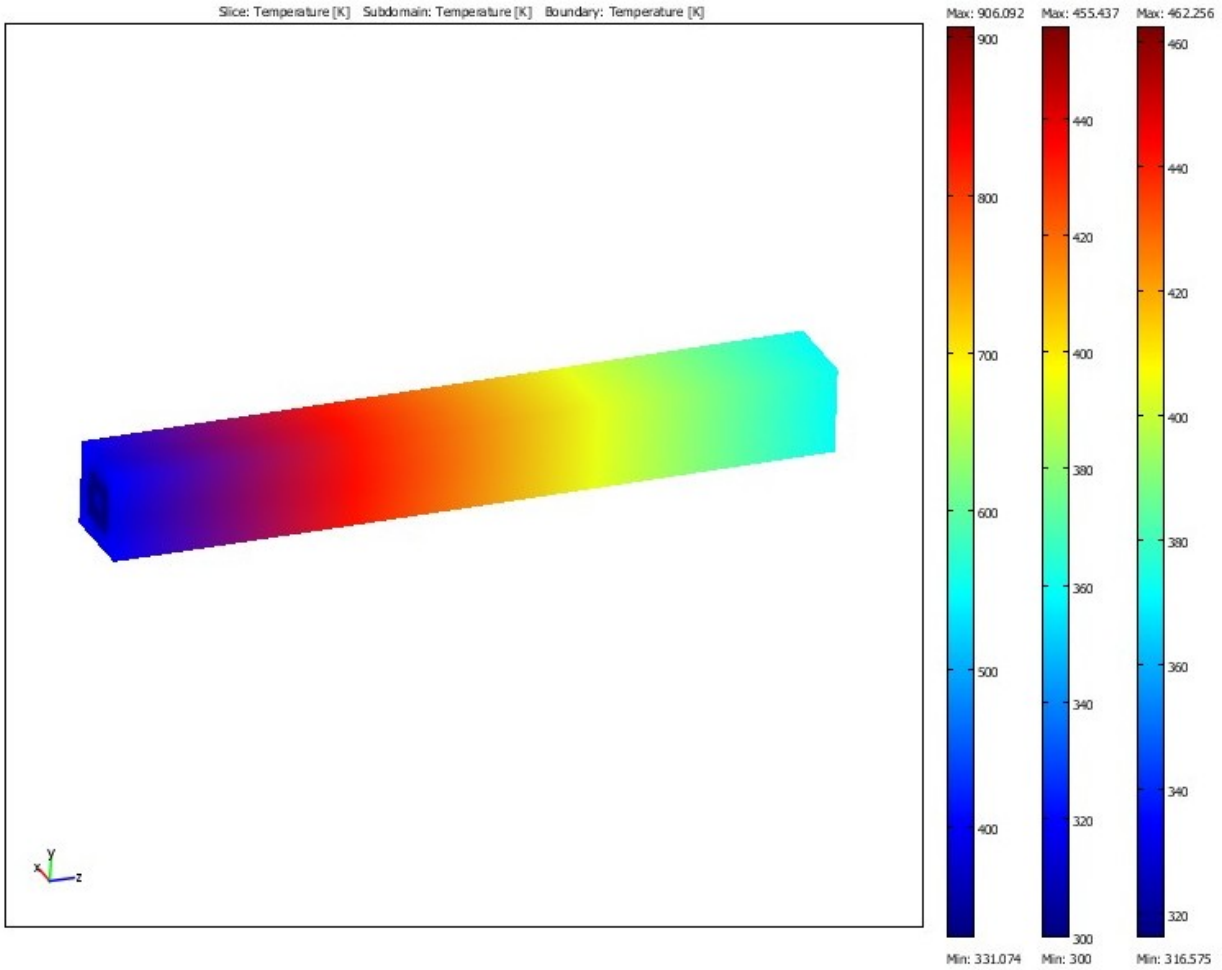

Figure 5.11. Axial temperature profile of counter-current heat-exchanger microscale reactor constructed with stainless steel substrate of thermal conductivity K = 16.2 W/mK

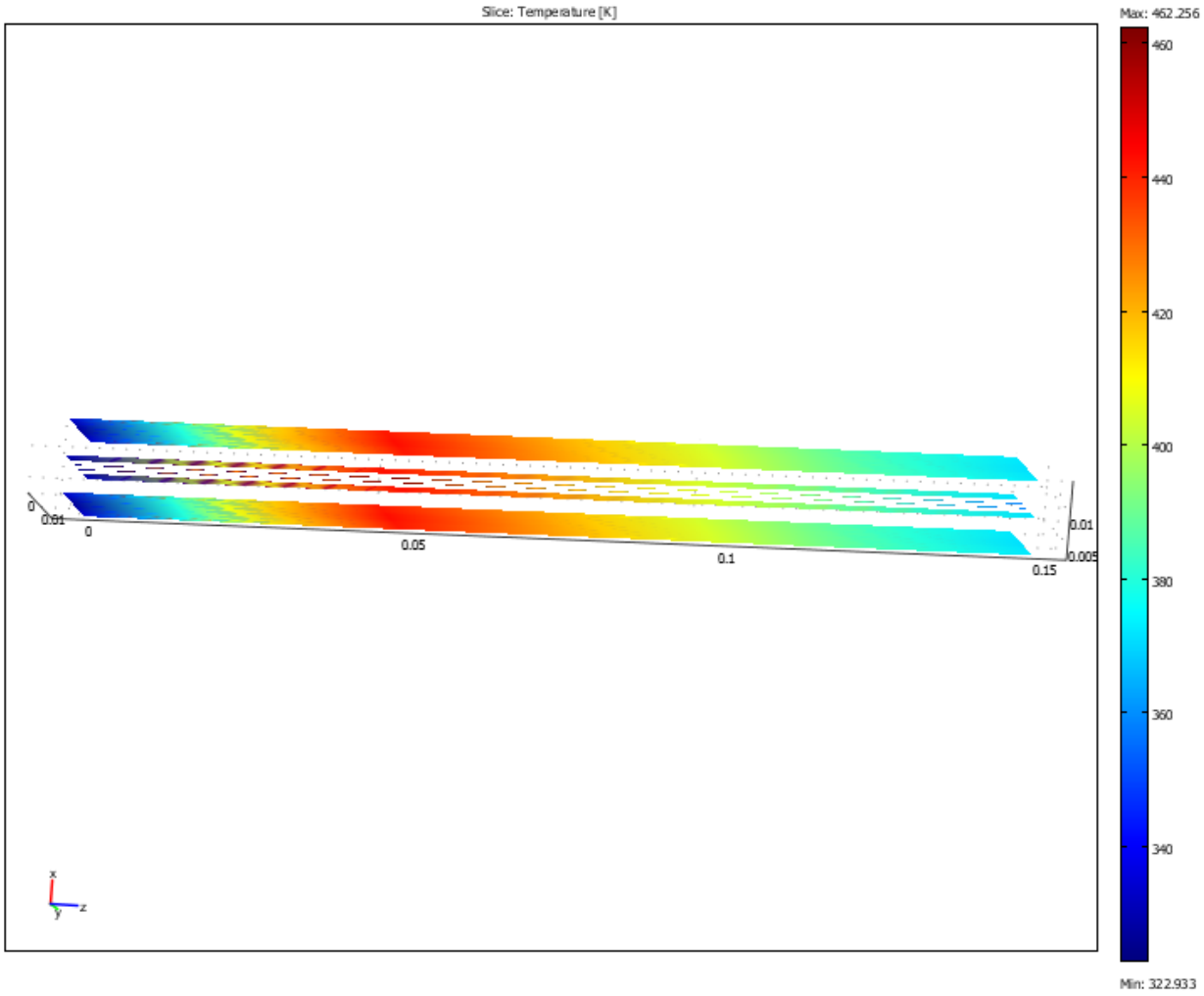

Figure 5.12. Slice plot along the x-direction showing axial and radial temperature profile of the microreactor constructed with stainless steel substrate

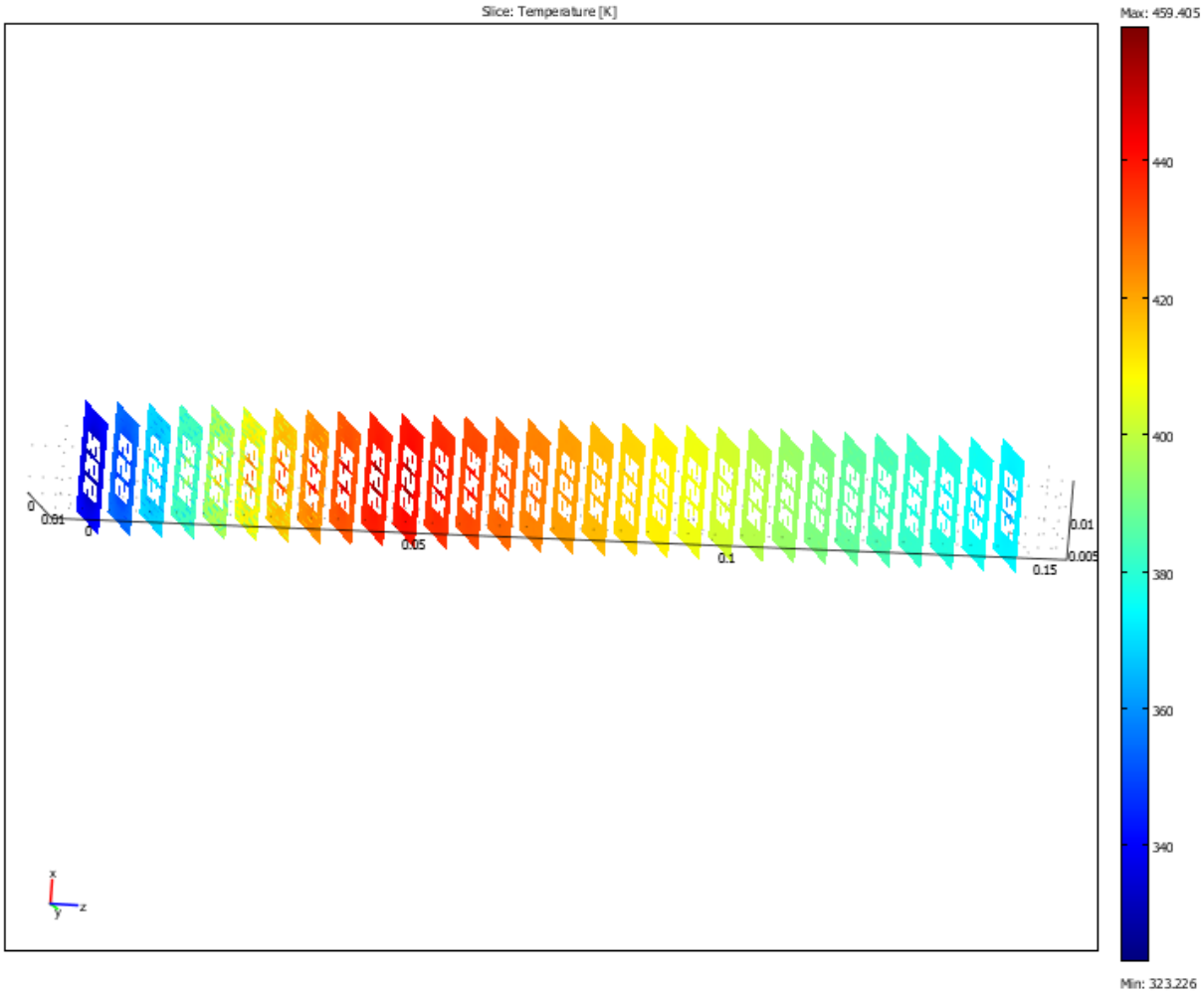

Figure 5.13. Slice plot along the z-direction showing axial and radial temperature profile of the microreactor constructed with stainless steel substrate

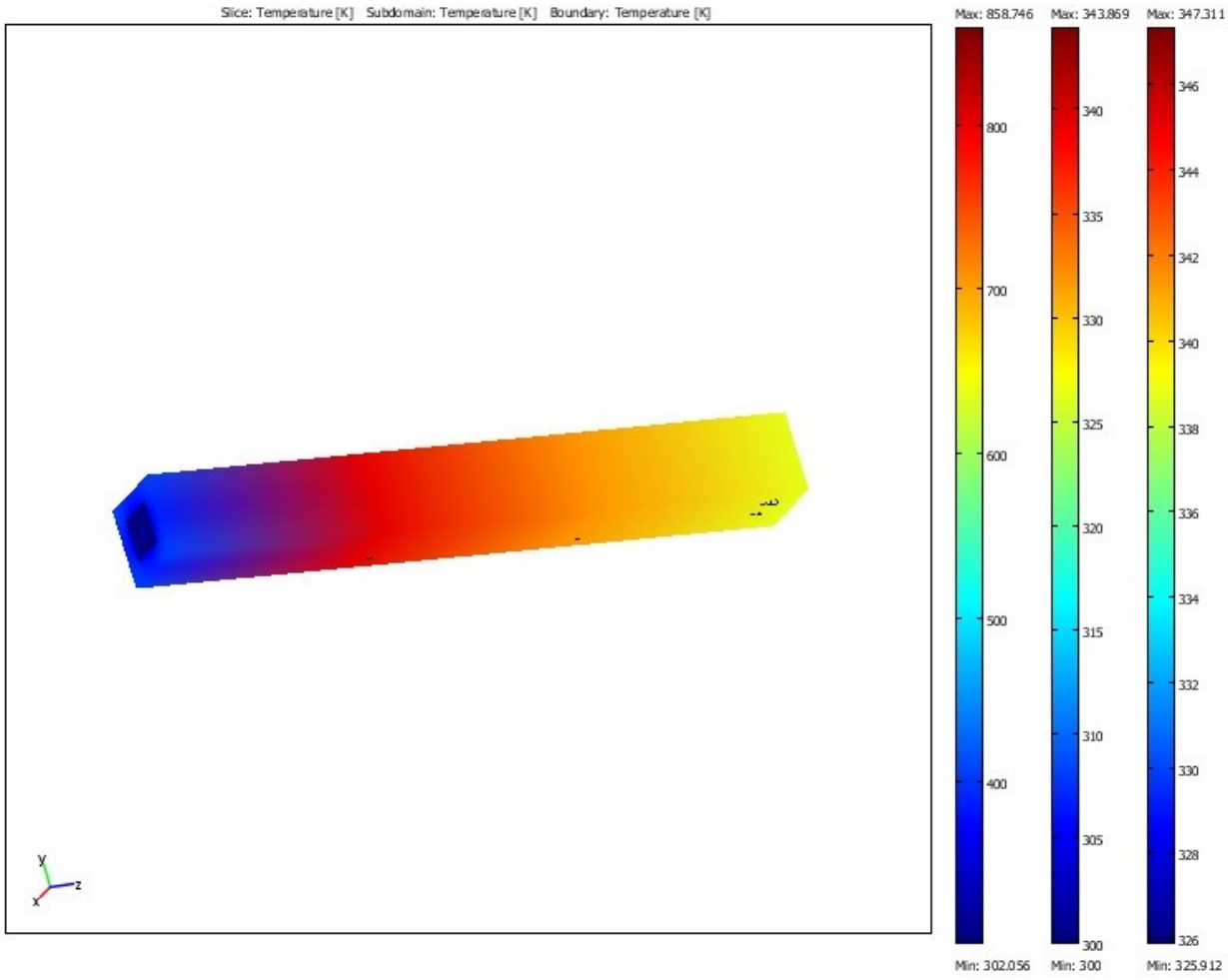

Figure 5.14. Axial temperature profile of counter-current heat-exchanger microscale reactor constructed with silicon substrate of thermal conductivity K = 150 W/mK

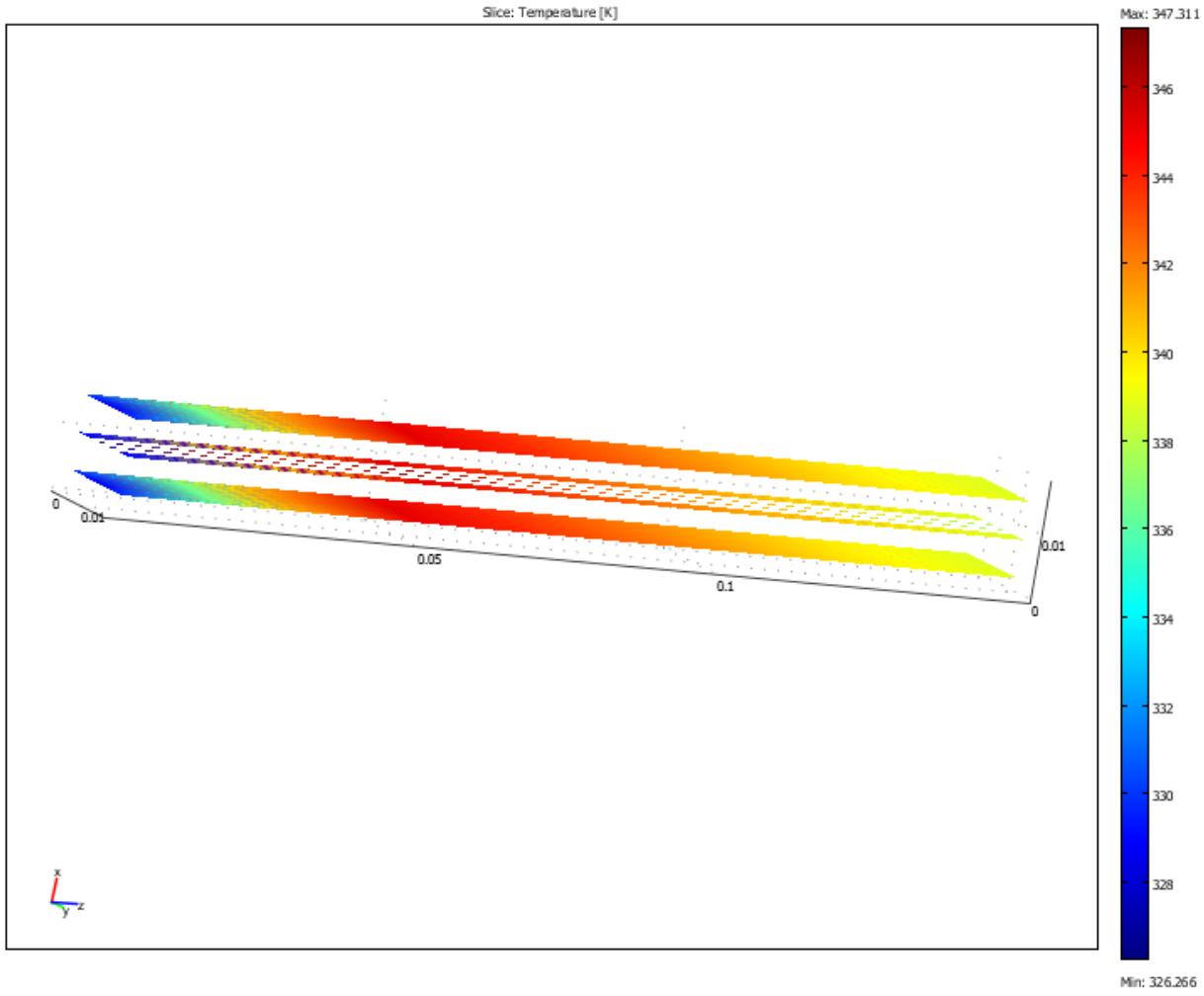

Figure 5.15. Slice plot along the x-direction showing axial and radial temperature profile of the microreactor constructed with silicon substrate

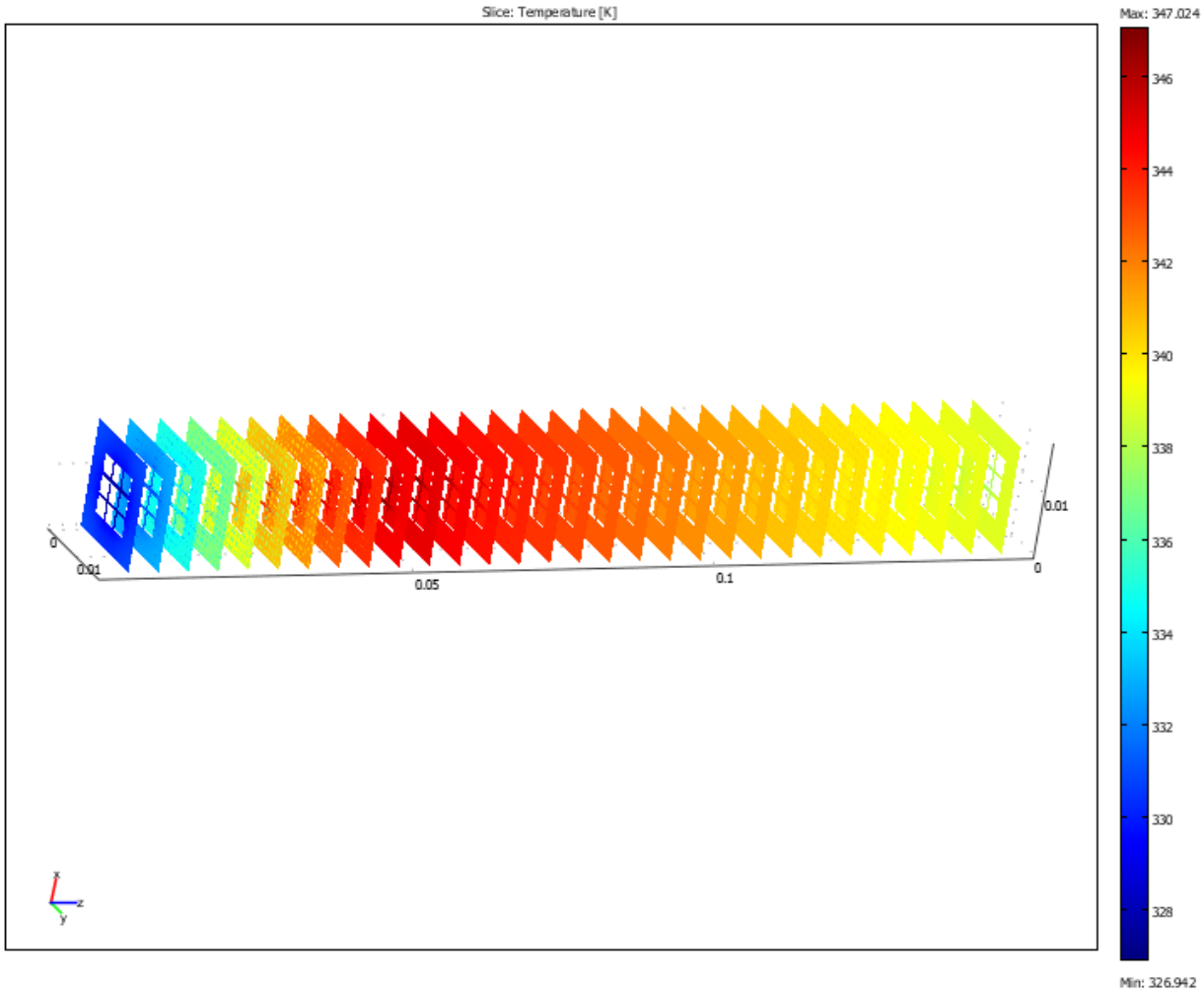

Figure 5.16. Slice plot along the z-direction showing axial and radial temperature profile of the microreactor constructed with silicon substrate

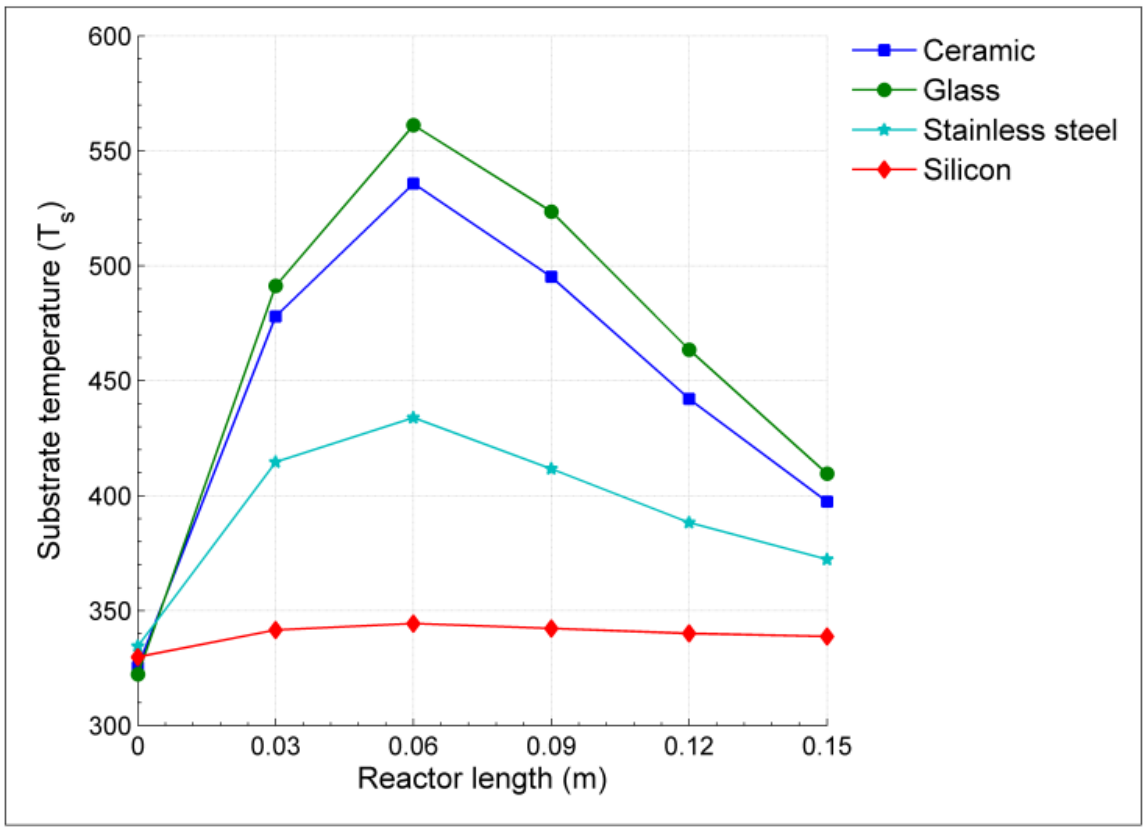

Figure 5.17. Axial temperature profile of the counter-current heat-exchanger microreactor for four different materials

The methanol conversion, overall hydrogen yield and thermal efficiency were calculated for the heat-exchanger microreactor designed with four different thermal conductivity substrates. Each reaction process has unique heat duty and optimal operating temperatures for their improved performance. Methanol steam reforming reaction should be operated at a temperature range of 220 - 300^{o}C for obtaining higher yields and increased CO_2 selectivities.

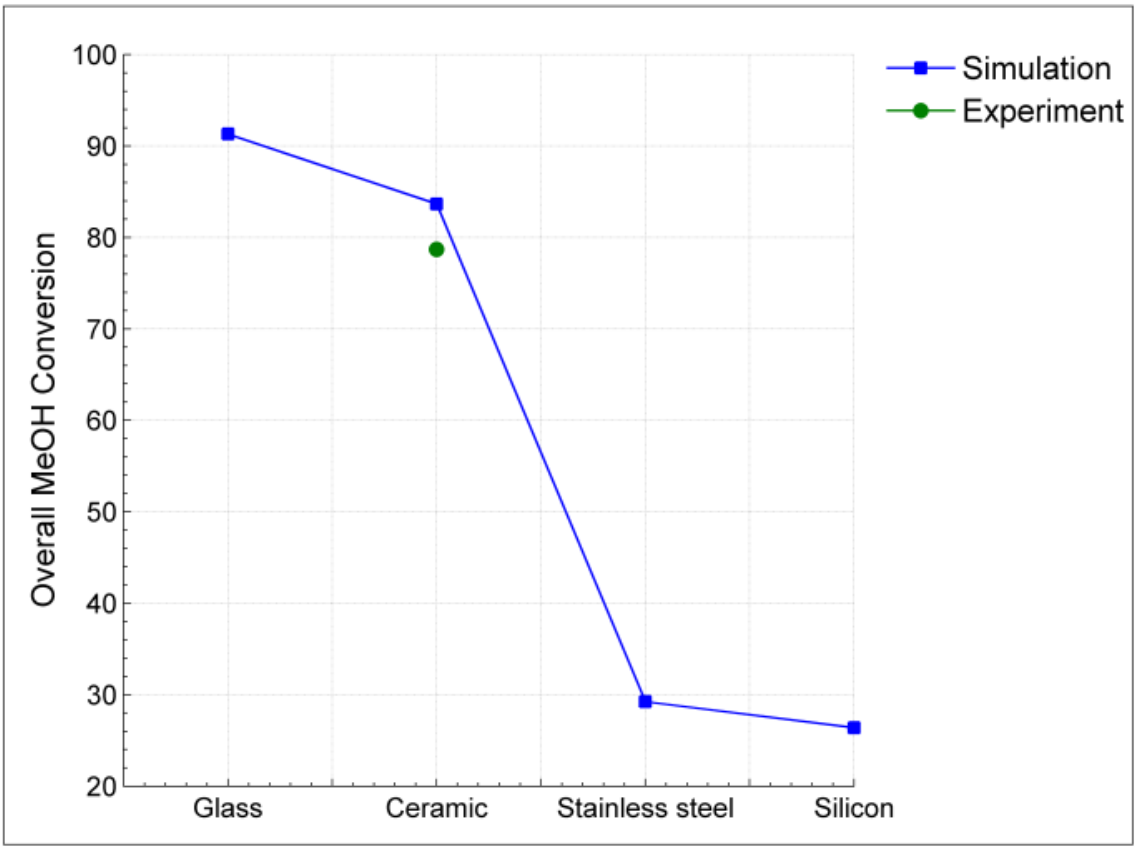

Figure 5.18. Overall methanol conversion of a heat-integrated microreactor studied with four different thermal conductivity materials

High thermal conductivity materials failed to maintain required hot-spot temperature in the reactor due to rapid axial conduction heat losses, which lowered the thermal gradient of the system. The insufficient heat supply to the endothermic reaction resulted in reduced conversion and hydrogen yield in the reforming volume. The thermal efficiency (shown in Figure 5.21) of the system was improved with the reduction in thermal conductivity of the substrate. A decrease in wall thermal conductivity resulted in increased heat retention in the system offering sufficient heat to drive the endothermic

steam reforming reaction. Methanol conversion (shown in Figure 5.19) and overall hydrogen yield (shown in Figure 5.20) increased with a decrease in substrate thermal conductivity and the overall Y_{H2} of ~ 55% & ~52% was obtained with glass and ceramic substrates respectively. The simulation with ceramic substrate showed promising results when compared with the experimental results (discussed in Chapter 3), which offered overall Y_{H2} of 53% with the same operating parameters.

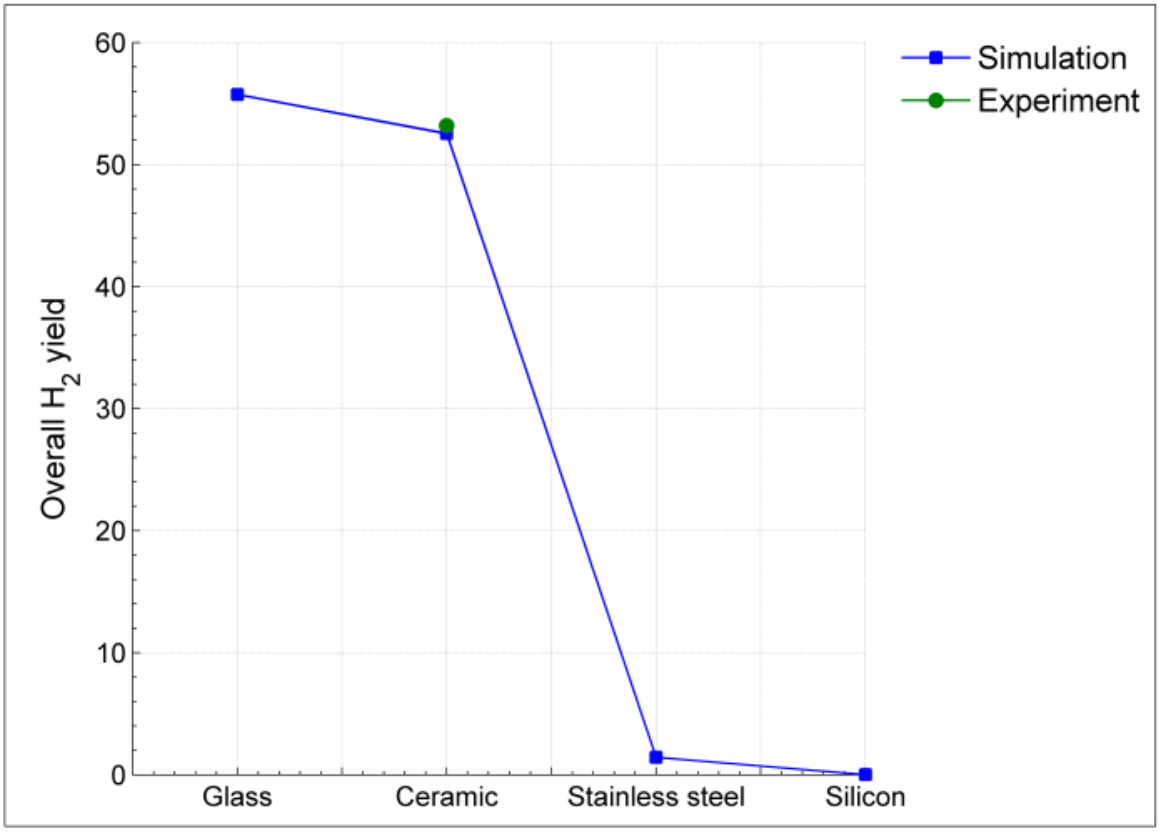

Figure 5.19. Overall hydrogen yield of a heat-integrated microreactor studied with four different thermal conductivity materials

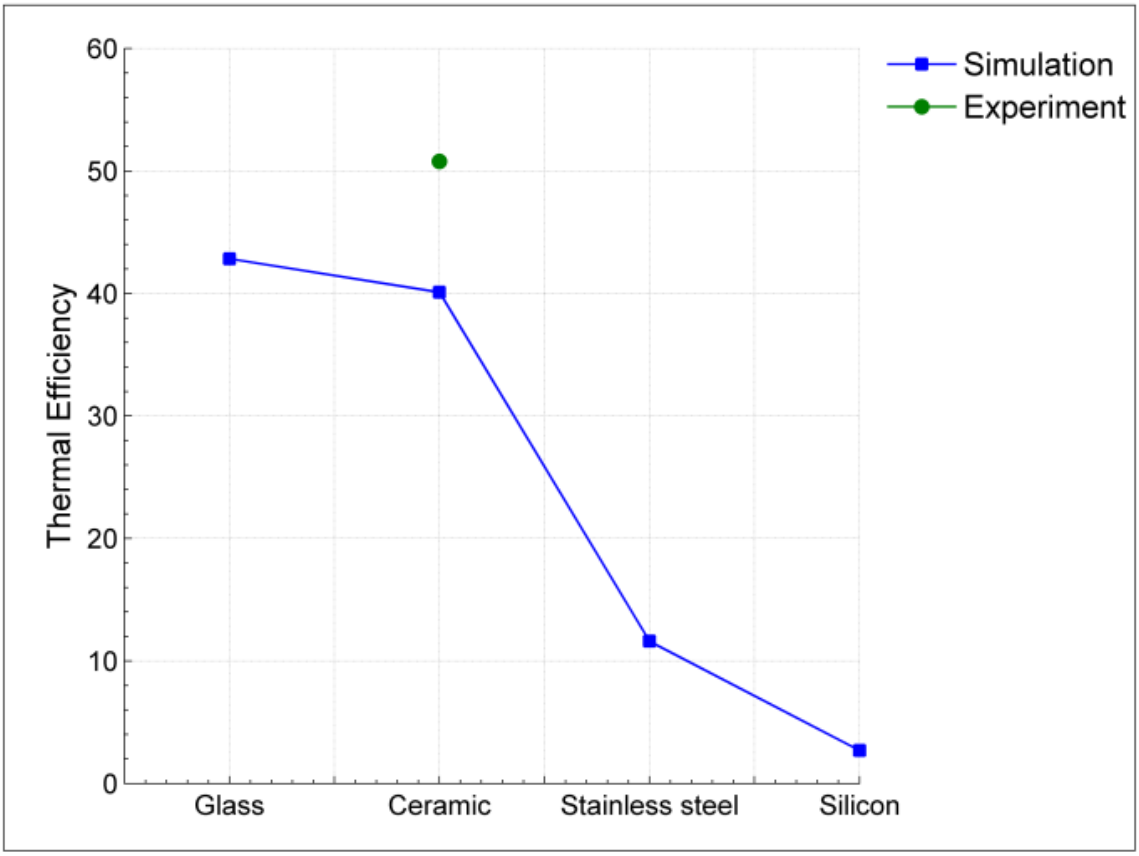

Figure 5.20. Thermal efficiency of a heat-integrated microreactor studied with four different thermal conductivity materials

5.4 Conclusion

A 3-D model of counter-current heat-exchanger microreactor developed using COMSOL 3.5a, was used as a numerical tool to explore the optimum operating parameters and substrate thermal conductivity in order to enhance the productivity of the microsystems used for fuel reformers. The simulation results of 5x5 microchannel

reactor with low thermal conductivity substrates provided promising results with the location of symmetrical hot-spot near to the axial midpoint of the microreactor. The above results also showed that the substrate selection plays a vital role for the efficient thermal coupling of exothermic and endothermic reaction. A decrease in wall thermal conductivity reduced the axial heat conduction and provided a large thermal gradient in the system by minimizing axial and radial heat losses. High thermal conductivity materials like silicon, stainless steel requires complex structures/designs like vacuum gaps or insulating materials to maintain sufficient thermal differences between reactor components for improved reactor performance. Addition of insulators increases the weight and volume of the system thereby decreases the energy density. Conversion, yield and thermal efficiency of the system were observed to be strongly affected by substrate thermal conductivity and axial heat conduction. An overall hydrogen yield of ~55% and ~52% was obtained with glass and ceramics respectively, whereas negligible yields were observed with high thermal conductivity materials like silicon and stainless steel. Therefore, low thermal conductivity substrates such as glass, ceramics offer enhanced reactor performance by increasing the thermal efficiency of the system.

6. CONCLUSIONS, RECOMMENDATIONS AND ENERGY DENSITY CALCULATIONS

6.1 Conclusions

A new class of cartridge-based heat-exchanger microchannel reactor was constructed by our research group through combination of (1) precision machining of metals and (2) ceramic extrusion, which provided a cost-effective, scalable and energy-efficient process of hydrogen production for portable power. The initial study performed by Dr.Angela Moreno with a 3x3 checkerboard patterned microreactor demonstrated that this novel design was capable of providing axially self-insulating thermal patterns capable of maintaining a stable, symmetrical hot-spot at the axial mid-point of the reactor with a packaging temperature of <50^{o}C in the absence of any external insulation and provided an overall hydrogen yield of ~11%.

A preliminary study (Chapter 2) with Dr.Angela Moreno investigating three unique radial distribution architectures indicated that a radially-layered distribution pattern with Architecture C of 3 flow volumes for flow folding, provides the maximum external surface temperature dropped by 50 - 150^{o}C, even though the conversions were similar, the center of the hotspot remained the same, but reduced radial heat losses. Optimization of process flowrates and equivalence ratio by analyzing various reforming and combustion flowrates was accomplished experimentally through the 5x5 Architecture C selected through this preliminary study.

A packed-bed catalyst configuration of 3.3 cm depth of Pt/Al_2O_3 pellets (0.16-0.18 g) in the combustion channel, positioned at the axial mid-point of the reactor, with 6 cm of $CuO/ZnO/Al_2O_3$ pellets (0.3 g) in the reforming channels, helped in preventing the hotspot mobility from the axial center of the reactor, allowing a much broader range of process flows to be investigated using Architecture C configuration (Chapter 3). The overall hydrogen yield was increased with an increasing reforming flowrate and the maximum overall H_2 yield of 53% was attained at higher reforming flowrates with an increase in combustion flowrate. Net H_2 yield of >50% and thermal efficiency of >80% was achieved from methanol with minimal insulation to the heat-integrated ceramic microchannel network.

Four reactor configurations were investigated using the outer 16 channels of Architecture C (Chapter 4), by preheating the combustion/reforming input stream and sealing with combustion/reforming output stream, which showed 50^oC – 60^oC higher hot-spot magnitude through enhanced axial and radial insulation than the earlier experiments with Architecture C and manifested the effect of hot-spot magnitude on the catalytic activity and WGS equilibrium for improved reactor performance. The maximum overall hydrogen yield of 58% was achieved with the combustion flowrate of 300 sccm and reforming flow rate of 1800 sccm by preheating the reforming stream in the outer 16 heat retention channels.

The 3-D COMSOL model (Chapter 5) served as a mathematical tool to explore the hot-spot location, shape and optimum process conditions of a counter-current heat-exchanger microreactor and also to establish the effect of substrate thermal conductivity

upon the reactor performance. Low thermal conductivity substrates such as glass, ceramics offered enhanced efficiencies than the higher thermal conductivity materials like silicon and stainless steel, by maintaining large thermal gradients through reduction in axial and radial heat losses.

Overall, this research demonstrated the optimal Architecture, process flowrates and substrate thermal conductivity for the efficient operation of thermally-integrated heat exchanger microchannel network by coupling exothermic methanol combustion and endothermic methanol steam reforming.

6.2 Recommendations

The following recommendations would refine the applicability of this novel microchannel network as efficient micro-fuel reformers for portable hydrogen production for PEMFCs:

1. Development of light-weight silicon distributors by employing efficient microfabrication techniques, in order to achieve higher gravimetric and volumetric energy densities.
2. Extensive experimental study on the four reactor configurations using the outer 16 channels of Architecture C, with substantial reduction in combustion fuel addition to maintain the optimum reactor temperature.
3. Enhance the 3-D COMSOL model as a numerical tool to optimize the reactor design and operating parameters to further improve the overall hydrogen yield and thermal efficiency.

4. Incorporation of hydrogen gas purification process along with simultaneous combustion and reforming reaction by introducing carbon monoxide removal step (preferential oxidation or additional water-gas shift reaction) or by hydrogen separation from carbon gases through the palladium membrane.
5. Catalytic studies focusing on the regeneration of combustion (Pt/Al_2O_3) and reforming ($CuO/ZnO/Al_2O_3$) catalyst after longer experimental runs.

6.3 Energy density calculations

The portable power sources in wireless and communication systems for consumer needs and military applications demands higher energy density. Conventional battery systems in current portable electronic devices failed to meet higher energy storage densities with its excessive weight and bulky design. Polymer electrolyte membrane fuel cells (PEMFCs) operating on hydrogen offer higher energy densities, longer operational time and less environmental impact than batteries. Table 6.1 provides the gravimetric and volumetric energy densities of various batteries compared with energy-dense hydrocarbon fuels. Fuel cells can be operated either with stored hydrogen or hydrogen produced from high energy dense hydrocarbons. Miniature fuel cells integrated with micro-fuel processors provides continuous operation by just refilling methanol and steam avoiding recharging cycles required by conventional Li-Ion batteries and thus, fuel processor/fuel cell system was considered as the efficient method for portable power generation. The energy density and efficiency of fuel cells integrated with fuel processor are higher than Li-Ion batteries, as detailed in Chapter 1. PEMFC

requires pure hydrogen for its operation and this can be achieved by employing membrane separation techniques along with fuel processing unit. Compact and efficient micro-scale fuel processor offers miniaturization and higher energy densities by carrying out methanol steam reforming for portable hydrogen production.

A novel cartridge-based ceramic microchannel network designed by our research group provided a complex two-dimensional heat integration patterns to couple exothermic methanol combustion and endothermic methanol steam reforming for autothermal hydrogen production. Energy storage density was calculated with the best results obtained from the brass distributors packaged ceramic microchannel network using Architecture C, with the maximum overall hydrogen yield of 1.30×10^{-4} mol/s at a combustion flowrate of 300 sccm and a reforming flowrate of 1800 sccm.

The fuel processor consisting of a combustor and reformer was integrated with a fuel cell system to calculate the energy density and efficiency of the overall power system. The reforming feed was comprised of 4.89×10^{-5} mol/s of methanol and 3.63×10^{-5} mol/s of water vapor whereas the combustion feed was composed of 3.28×10^{-5} mol/s of methanol. Thus, the power fed to the fuel processor from methanol was 51.7 W (with the heat of methanol of 6.30×10^{5} J/mol). Experimental results (reported in Chapter 3) showed 1.30×10^{-4} mol/s of hydrogen was produced from the fuel processor. Assuming 100% hydrogen utilization by the fuel cell, the power fed to the fuel cell by the hydrogen produced from fuel processor was 37.2 W. The maximum theoretical fuel processor efficiency was calculated through perfectly balancing the thermal energy of the system and was obtained as 72%; the decrease in thermal efficiency of our system to 51% was

due to heat loss through the product gas as sensible heat, and through conductive (to packaging) and convective (to atmosphere) heat transfer. Therefore, with the thermodynamic fuel processor efficiency of 72%, the overall system efficiency was estimated by assuming the fuel cell efficiency as 60%. The fuel cell power of 22.3 W was achieved with a fuel cell efficiency of 60% and the overall system efficiency of 43.2%.

The total weight of the system includes the mass of a fuel processor (distributors and ceramic microreactor packed with catalyst), fuel cell and the total fuel required for operation. Miniature hydrogen fuel cell of mass 0.031 g and volume of 0.012 cm^3 fabricated from micromachined silicon wafers by Kelley [81] group, was used to assume the fuel cell weight required for this analysis. Assuming 0.031 g of fuel cell system and 10 hrs mission time, the energy density of fuel processor/fuel cell assembly was calculated as shown in Table 6.1. The energy density calculations for silicon distributors- packaged microchannel network were performed using the same hydrogen yield reported in Chapter 3; where, distributor weight and volume were measured from silicon distributor assembly designed by Dr.Angela Moreno.

Table 6.1. Estimated energy density calculations of the system integrating fuel cell with the brass and silicon distributors packaged ceramic micro-fuel processor

	Brass Distributors (current work)	**Silicon Distributors (Proposed future work)**
Methanol fed to reformer	4.89 x10^{-5} mol/s	4.89x10^{-5}mol/s
Water fed to reformer	3.63x10^{-5} mol/s	3.63x10^{-5} mol/s
Methanol fed to combustor	3.28x10^{-5} mol/s	3.28x10^{-5} mol/s
Total methanol (reformer+combustor)	8.2x10^{-5} mol/s	8.20x10^{-5} mol/s
Total (fuel+water) to the system	1.18x10^{-4} mol/s	1.18x10^{-4} mol/s
Power from methanol fed to the system	51.7 W	51.7 W
Hydrogen produced	1.30x10^{-4} mol/s	1.30x10^{-4} mol/s
Hydrogen Utilization	100%	100%
Power from hydrogen produced	37.2 W	37.2 W
Fuel processor efficiency	72%	72%
Fuel cell efficiency	60%	60%
Fuel cell output power	22.3 W	22.3 W
Overall system efficiency	43.2%	43.2%
Mission time	10 hrs	10 hrs
Methanol weight/mission time	94.46 g	94.46 g
Water weight/mission time	23.54 g	23.54 g

Table 6.1 Continued

System weight:		
Two distributors	1823.66 g	131.47 g
Ceramic microreactor packed with catalyst	40.13 g	40.13 g
Fire brick insulation block	213.83 g	213.83 g
Fuel cell weight	0.031 g	0.031 g
Total weight	2195.65 g	503.50 g
Estimated gravimetric energy density	**169.34 Wh/kg**	**738.50 Wh/kg**
Volume of two distributors	447.30 cm^3	111.40 cm^3
Volume of ceramic microreactor	33.75 cm^3	33.75 cm^3
Volume of fire brick insulation block	110.88 cm^3	110.88 cm^3
Total system volume	592 cm^3	256 cm^3
Fuel volume (methanol+water)	143 cm^3	143 cm^3
Fuel cell volume	0.012 cm^3	0.012 cm^3
Total volume	734.75 cm^3	399 cm^3
Estimated volumetric energy density	**506.02 Wh/l**	**932.24 Wh/l**

A gravimetric and volumetric energy density of 169.34 Wh/kg and 506.02 Wh/l with a fuel cell power of 22.3 W was achieved from brass architectures for 10 hrs operation, which is higher than the energy density of Li-Ion batteries (120 Wh/kg and 350 Wh/l). The energy density of the fuel cell/ fuel processor assembly could be

increased significantly by reducing the mass of the fuel processor. This could be achieved through microfabrication of light-weight silicon substrates for the construction of microchannel network. The above analysis showed that silicon distributor assembly tremendously enhances both the gravimetric and volumetric energy density (738.5 Wh/kg and 932.24 Wh/l) of the system. Thus, the 37W heat-integrated ceramic microchannel methanol fuel processor has the capability of generating portable power by integrating with hydrogen fuel cells.

REFERENCES

[1] J. D. Holladay, Y. Wang, and E. Jones, "Review of developments in portable hydrogen production using microreactor technology," *Chemical Reviews,* vol. 104, pp. 4767-4790, 2004.

[2] C. K. Dyer, "Fuel cells for portable applications," *Fuel Cells Bulletin,* pp. 8-9, 2002.

[3] M. Granovskii, I. Dincer, and M. A. Rosen, "Life cycle assessment of hydrogen fuel cell and gasoline vehicles," *International Journal of Hydrogen Energy,* vol. 31, pp. 337-352, 2006.

[4] L. Carrette, K. A. Friedrich, and U. Stimming, "Fuel cells: principles, types, fuels, and applications," *ChemPhysChem,* vol. 1, pp. 162-193, 2000.

[5] L. Carrette, K. A. Friedrich, and U. Stimming, "Fuel cells – fundamentals and applications," *Fuel Cells,* vol. 1, pp. 5-39, 2001.

[6] J. Ramousse, J. Deseure, O. Lottin, S. Didierjean, and D. Maillet, "Modelling of heat, mass and charge transfer in a PEMFC single cell," *Journal of Power Sources,* vol. 145, pp. 416-427, 2005.

[7] J. H. Hirschenhofer, D. B. Stauffer, R. R. Engleman, and C. Morgantown Energy Technology, *Fuel cells : a handbook*. Morgantown, W.V.: U.S. Dept. of Energy, Office of Fossil Energy, Morgantown Energy Technology Center, 1994.

[8] V. S. Bagot͡skiĭ, *Fuel cells : problems and solutions : The ECS series of texts and monographs*, 2009.

[9] M. Winter and R. J. Brodd, "What are batteries, fuel cells, and supercapacitors?," *Chemical reviews,* vol. 104, pp. 4245-4270, 2004/10/01 2004.

[10] K. Shah, X. Ouyang, and R. S. Besser, "Microreaction for microfuel processing: challenges and prospects," *Chemical Engineering & Technology,* vol. 28, pp. 303-313, 2005.

[11] J. D. Holladay, E. O. Jones, M. Phelps, and J. Hu, "Microfuel processor for use in a miniature power supply," *Journal of Power Sources,* vol. 108, pp. 21-27, 2002.

[12] D. N. Prater and J. J. Rusek, "Energy density of a methanol/hydrogen-peroxide fuel cell," *Applied Energy,* vol. 74, pp. 135-140, 2003.

[13] S. S. Zhang, K. Xu, and T. R. Jow, "Study of the charging process of a LiCoO2-based Li-ion battery," *Journal of Power Sources,* vol. 160, pp. 1349-1354, 2006.

[14] R. von Helmolt and U. Eberle, "Fuel cell vehicles: Status 2007," *Journal of Power Sources,* vol. 165, pp. 833-843, 2007.

[15] G. Cacciola, V. Antonucci, and S. Freni, "Technology up date and new strategies on fuel cells," *Journal of Power Sources,* vol. 100, pp. 67-79, 2001.

[16] M. P. Hogarth and T. R. Ralph, "Catalysis for low temperature fuel cells," *Platinum Metals Review,* vol. 46, pp. 146-164, 2002.

[17] D. R. Palo, J. D. Holladay, R. T. Rozmiarek, C. E. Guzman-Leong, Y. Wang, J. Hu, Y.-H. Chin, R. A. Dagle, and E. G. Baker, "Development of a soldier-portable fuel cell power system: Part I: A bread-board methanol fuel processor," *Journal of Power Sources,* vol. 108, pp. 28-34, 2002.

[18] U. S. D.o.Energy, "Hydrogen, fuel cells and infrastructure technologies program: Multi-year research, development and demonstration plan," pp 1-12, April 2009, http://www1.eere.energy.gov/hydrogenandfuelcells/mypp/.

[19] R.-N. Thomas, "Manufacture of hydrogen," *Catalysis Today,* vol. 106, pp. 293-296, 2005.

[20] J. D. Holladay, J. Hu, D. L. King, and Y. Wang, "An overview of hydrogen production technologies," *Catalysis Today,* vol. 139, pp. 244-260, 2009.

[21] T. Riis and E. F. Hagen, "Hydrogen production - gaps and priorities," *IEA Hydrogen implementing Agreement*, IEA, Paris, 2005, http://www.bctia.org/files/PDF/hydrogen_fuel_cells/Hydrogen_Production_Gaps_Priorities_-_IEA_-_2005.pdf.

[22] A. Stankiewicz and J. A. Moulijn, "Process intensification," *Industrial & Engineering Chemistry Research,* vol. 41, pp. 1920-1924, 2002/04/01 2002.

[23] F. M. Dautzenberg and M. Mukherjee, "Process intensification using multifunctional reactors," *Chemical Engineering Science,* vol. 56, pp. 251-267, 2001.

[24] S. Andrzej, "Reactive separations for process intensification: an industrial perspective," *Chemical Engineering and Processing: Process Intensification,* vol. 42, pp. 137-144, 2003.

[25] K. L. Wasewar, V. G. Pangarkar, A. B. M. Heesink, and G. F. Versteeg, "Intensification of enzymatic conversion of glucose to lactic acid by reactive extraction," *Chemical Engineering Science,* vol. 58, pp. 3385-3393, 2003.

[26] H. J. Bart, C. Drumm, and M. M. Attarakih, "Process intensification with reactive extraction columns," *Chemical Engineering and Processing: Process Intensification,* vol. 47, pp. 745-754, 2008.

[27] K. K. Sirkar, P. V. Shanbhag, and A. S. Kovvali, "Membrane in a reactor: A functional perspective," *Industrial & Engineering Chemistry Research,* vol. 38, pp. 3715-3737, 1999/10/01 1999.

[28] R. C. Ramaswamy, P. A. Ramachandran, and M. P. Dudukovic, "Recuperative coupling of exothermic and endothermic reactions," *Chemical Engineering Science,* vol. 61, pp. 459-472, 2006.

[29] R. K. Grasselli, D. L. Stern, and J. G. Tsikoyiannis, "Catalytic dehydrogenation (DH) of light paraffins combined with selective hydrogen combustion (SHC): I. DH --> SHC --> DH catalysts in series (co-fed process mode)," *Applied Catalysis A: General,* vol. 189, pp. 1-8, 1999.

[30] R. K. Grasselli, D. L. Stern, and J. G. Tsikoyiannis, "Catalytic dehydrogenation (DH) of light paraffins combined with selective hydrogen combustion (SHC): II. DH+SHC catalysts physically mixed (redox process mode)," *Applied Catalysis A: General,* vol. 189, pp. 9-14, 1999.

[31] D. A. Henning and L. D. Schmidt, "Oxidative dehydrogenation of ethane at short contact times: species and temperature profiles within and after the catalyst," *Chemical Engineering Science,* vol. 57, pp. 2615-2625, 2002.

[32] V. R. Choudhary, V. H. Rane, and A. M. Rajput, "High-temperature catalytic oxidative conversion of propane to propylene and ethylene involving coupling of exothermic and endothermic reactions," *Industrial & Engineering Chemistry Research,* vol. 39, pp. 904-908, 2000.

[33] G. Kolios, J. Frauhammer, and G. Eigenberger, "Autothermal fixed-bed reactor concepts," *Chemical Engineering Science,* vol. 55, pp. 5945-5967, 2000.

[34] M. van Sint Annaland and R. C. Nijssen, "A novel reverse flow reactor coupling endothermic and exothermic reactions: an experimental study," *Chemical Engineering Science,* vol. 57, pp. 4967-4985, 2002.

[35] T. Liu, H. Temur, and G. Veser, "Autothermal reforming of methane in a reverse-flow reactor," *Chemical Engineering & Technology,* vol. 32, pp. 1358-1366, 2009.

[36] S. R. Deshmukh and D. G. Vlachos, "CFD simulations of coupled, countercurrent combustor/reformer microdevices for hydrogen production," *Industrial & Engineering Chemistry Research,* vol. 44, pp. 4982-4992, 2005.

[37] G. Kolios, J. Frauhammer, and G. Eigenberger, "Efficient reactor concepts for coupling of endothermic and exothermic reactions," *Chemical Engineering Science,* vol. 57, pp. 1505-1510, 2002.

[38] L. R. Arana, S. B. Schaevitz, A. J. Franz, M. A. Schmidt, and K. F. Jensen, "A microfabricated suspended-tube chemical reactor for thermally efficient fuel processing," *Microelectromechanical Systems, Journal of,* vol. 12, pp. 600-612, 2003.

[39] J. Frauhammer, G. Eigenberger, L. v. Hippel, and D. Arntz, "A new reactor concept for endothermic high-temperature reactions," *Chemical Engineering Science,* vol. 54, pp. 3661-3670, 1999.

[40] G. Kolios, J. Frauhammer, and G. Eigenberger, "A simplified procedure for the optimal design of autothermal reactors for endothermic high-temperature reactions," *Chemical Engineering Science,* vol. 56, pp. 351-357, 2001.

[41] Z. Anxionnaz, M. Cabassud, C. Gourdon, and P. Tochon, "Heat exchanger/reactors (HEX reactors): Concepts, technologies: State-of-the-art," *Chemical Engineering and Processing: Process Intensification,* vol. 47, pp. 2029-2050, 2008.

[42] N. de Mas, A. Günther, M. A. Schmidt, and K. F. Jensen, "Increasing productivity of microreactors for fast gas−liquid reactions: the case of direct fluorination of toluene," *Industrial & Engineering Chemistry Research,* vol. 48, pp. 1428-1434, 2009/02/04 2008.

[43] I.-M. Hsing, K.F. Jensen, R. Srinivasan, M.A. Schmidt, "Reaction engineering for microreactor systems," *Microreactor Technology : Proceedings of the First International Conference on Microreactor Technology*, W. Ehrfeld, Ed. Berlin, Germany: Springer Verlag, Berlin, pp. 2-9, 1997.

[44] A. Gavriilidis, P. Angeli, E. Cao, K. K. Yeong, and Y. S. S. Wan, "Technology and applications of microengineered reactors," *Chemical Engineering Research and Design,* vol. 80, pp. 3-30, 2002.

[45] K. F. Jensen, "Microchemical systems: Status, challenges, and opportunities," *AIChE Journal,* vol. 45, pp. 2051-2054, 1999.

[46] K. F. Jensen, "Microreaction engineering -- is small better?," *Chemical Engineering Science,* vol. 56, pp. 293-303, 2001.

[47] B. A. Wilhite, "Thermal management and system integration," in *Microfabricated Power Generation Devices*, ed: Wiley-VCH Verlag GmbH & Co. KGaA, 2009, pp. 113-140.

[48] K. Shah and R. S. Besser, "Key issues in the microchemical systems-based methanol fuel processor: Energy density, thermal integration, and heat loss mechanisms," *Journal of Power Sources,* vol. 166, pp. 177-193, 2007.

[49] E. R. Delsman, M. H. J. M. de Croon, G. J. Kramer, P. D. Cobden, C. Hofmann, V. Cominos, and J. C. Schouten, "Experiments and modelling of an integrated preferential oxidation-heat exchanger microdevice," *Chemical Engineering Journal,* vol. 101, pp. 123-131, 2004.

[50] M. V. Twigg and M. S. Spencer, "Deactivation of copper metal catalysts for methanol decomposition, methanol steam reforming and methanol synthesis," *Topics in Catalysis,* vol. 22, pp. 191-203, 2003.

[51] R. B. Peterson, "Numerical modeling of conduction effects in microscale counterflow heat exchangers," *Microscale Thermophysical Engineering,* vol. 3, pp. 17-30, 1999/02/01 1999.

[52] T. Stief, O.-U. Langer, and K. Schubert, "Numerical investigations of optimal heat conductivity in micro heat exchangers," *Chemical Engineering & Technology,* vol. 22, pp. 297-303, 1999.

[53] C. Schmitt, D. W.Agar, and F. Platte, "Ceramic plate heat exchanger for heterogeneous gas-phase reactions," *Chemical Engineering & Technology,* vol. 28, pp. 337-343, 2005.

[54] A. Moreno, K. Murphy, and B. A. Wilhite, "Parametric study of solid-phase axial heat conduction in thermally integrated microchannel networks," *Industrial & Engineering Chemistry Research,* vol. 47, pp. 9040-9054, 2008.

[55] V. Tomasic and F. Jovic, "State-of-the-art in the monolithic catalysts/reactors," *Applied Catalysis A: General,* vol. 311, pp. 112-121, 2006.

[56] R. M. Heck, S. Gulati, and R. J. Farrauto, "The application of monoliths for gas phase catalytic reactions," *Chemical Engineering Journal,* vol. 82, pp. 149-156, 2001.

[57] X. Karatzas, M. Nilsson, J. Dawody, B. Lindström, and L. J. Pettersson, "Characterization and optimization of an autothermal diesel and jet fuel reformer for 5 kWe mobile fuel cell applications," *Chemical Engineering Journal,* vol. 156, pp. 366-379, 2010.

[58] A. Casanovas, C. de Leitenburg, A. Trovarelli, and J. Llorca, "Catalytic monoliths for ethanol steam reforming," *Catalysis Today,* vol. 138, pp. 187-192, 2008.

[59] A. Qi, S. Wang, G. Fu, C. Ni, and D. Wu, "La-Ce-Ni-O monolithic perovskite catalysts potential for gasoline autothermal reforming system," *Applied Catalysis A: General,* vol. 281, pp. 233-246, 2005.

[60] C. P. Rodrigues, V. T. da Silva, and M. Schmal, "Partial oxidation of ethanol over cobalt oxide based cordierite monolith catalyst," *Applied Catalysis B: Environmental,* vol. 96, pp. 1-9, 2010.

[61] R. M. Navarro, M. A. Pena, and J. L. Fierro, "Hydrogen production reactions from carbon feedstocks: fossil fuels and biomass," *Chemical Reviews,* vol. 107, pp. 3952-91, Oct 2007.

[62] D. R. Palo, R. A. Dagle, and J. D. Holladay, "Methanol steam reforming for hydrogen production," *Chemical Reviews,* vol. 107, pp. 3992-4021, Oct 2007.

[63] S. Ahmed and M. Krumpelt, "Hydrogen from hydrocarbon fuels for fuel cells," *International Journal of Hydrogen Energy,* vol. 26, pp. 291-301, 2001.

[64] W.-H. Cheng, I. Chen, J.-s. Liou, and S.-S. Lin, "Supported Cu catalysts with yttria-doped ceria for steam reforming of methanol," *Topics in Catalysis,* vol. 22, pp. 225-233, 2003.

[65] L. Ma, B. Gong, T. Tran, and M. S. Wainwright, "Cr2O3 promoted skeletal Cu catalysts for the reactions of methanol steam reforming and water gas shift," *Catalysis Today,* vol. 63, pp. 499-505, 2000.

[66] C.-Y. Huang, Y.-M. Sun, C.-Y. Chou, and C.-C. Su, "Performance of catalysts CuO-ZnO-Al2O3, CuO-ZnO-Al2O3-Pt-Rh, and Pt-Rh in a small reformer for hydrogen generation," *Journal of Power Sources,* vol. 166, pp. 450-457, 2007.

[67] Y.-H. Chin, R. Dagle, J. Hu, A. C. Dohnalkova, and Y. Wang, "Steam reforming of methanol over highly active Pd/ZnO catalyst," *Catalysis Today,* vol. 77, pp. 79-88, 2002.

[68] Y.-H. Chin, Y. Wang, R. A. Dagle, and X. Shari Li, "Methanol steam reforming over Pd/ZnO: Catalyst preparation and pretreatment studies," *Fuel Processing Technology,* vol. 83, pp. 193-201, 2003.

[69] C. Cao, G. Xia, J. Holladay, E. Jones, and Y. Wang, "Kinetic studies of methanol steam reforming over Pd/ZnO catalyst using a microchannel reactor," *Applied Catalysis A: General,* vol. 262, pp. 19-29, 2004.

[70] S. Velu, K. Suzuki, and T. Osaki, "Oxidative steam reforming of methanol over CuZnAl(Zr)-oxide catalysts; a new and efficient method for the production of CO-free hydrogen for fuel cells," *Chemical Communications,* pp. 2341-2342, 1999.

[71] A. M. Moreno and B. A. Wilhite, "Autothermal hydrogen generation from methanol in a ceramic microchannel network," *Journal of Power Sources,* vol. 195, pp. 1964-1970, 2010.

[72] A. M. Moreno, S. Damodharan, and B. Wilhite, "Influence of two-dimensional distribution schemes upon reactor performance in a ceramic microchannel network for autothermal methanol reforming," *Industrial & Engineering Chemistry Research,* vol. 49, pp. 10956-10964, 2010/11/03 2010.

[73] A. M. Moreno, "Thermally integrated ceramic microreactors for hydrogen production," *DigitalCommons@UConn,* 2010.

[74] A. G. Dixon and D. L. Cresswell, "Theoretical prediction of effective heat transfer parameters in packed beds," *AIChE Journal,* vol. 25, pp. 663-676, 1979.

[75] C. Geankoplis, *Transport Processes and Separation Process Principles (Includes Unit Operations) Fourth Edition*, 2003.

[76] J. C. Amphlett, K. A. M. Creber, J. M. Davis, R. F. Mann, B. A. Peppley, and D. M. Stokes, "Hydrogen production by steam reforming of methanol for polymer electrolyte fuel cells," *International Journal of Hydrogen Energy,* vol. 19, pp. 131-137, 1994.

[77] S. J. Gentry, A. Jones, and P. T. Walsh, "Kinetics of methanol oxidation over platinum wire catalysts," *Journal of the Chemical Society, Faraday Transactions 1: Physical Chemistry in Condensed Phases,* vol. 76, pp. 2084-2095, 1980.

[78] A. Schwartz, L. L. Holbrook, and H. Wise, "Catalytic oxidation studies with platinum and palladium," *Journal of Catalysis,* vol. 21, pp. 199-207, 1971.

[79] A. Kos, "Experimental-verification on the temperature distribution on ceramic substrates," *Journal of physics. B, Atomic, molecular and optical physics,* vol. 27, p. 2163, 1994.

[80] C. R. Wilke, "A viscosity equation for gas mixtures," *The Journal of Chemical Physics,* vol. 18, p. 517, 1950.

[81] S. C. Kelley, G. A. Deluga, and W. H. Smyrl, "Miniature fuel cells fabricated on silicon substrates," *AIChE Journal,* vol. 48, pp. 1071-1082, 2002.

VITA

Name:	Shalini Damodharan
Address:	Texas A&M University, Artie McFerrin Department of Chemical Engineering, 3122 TAMU, College Station TX 77843
Email Address:	shalini.damodharan@gmail.com
Education:	B.Tech., Anna University, India, 2007 M.S., Chemical Engineering, Texas A&M University, 2012